THÈSE

Pour l'obtention du grade de

DOCTEUR DE L'UNIVERSITÉ DE POITIERS

Faculté des Sciences Fondamentales et Appliquées

Diplôme National - Arrêté du 25 mai 2016

École doctorale sciences et ingénierie des matériaux, mécanique, énergétique

Domaine de recherche: milieux denses et matériaux

Présentée par

Emmanuel Adetola FODEKE

Mechanical behaviour of 2D materials on strained substrates: experimental investigation on MoS_2

Directeurs de thèse: **Christophe COUPEAU** et **Loranne VERNISSE**

Soutenance le 9 juin 2023

Devant la Commission d'Examen

JURY

P. LECLERE	Professeur, Université de Mons, Belgique	Rapporteur
G. PARRY	Maître de Conférences, SIMAP, Univ. de Grenoble Alpes	Rapporteur
A. CLAUDEL	Ingénieur de Recherche, Institut Néel, Grenoble	Examinateur
B. KOKOH	Professeur des Universités, IC2MP, Univ. de Poitiers	Examinateur
L. VERNISSE	Maître de Conférences, Institut P', Univ. de Poitiers	Examinatrice
C. COUPEAU	Professeur des Universités, Institut P', Univ. de Poitiers	Examinateur

Acknowledgements

Firstly, I would like to appreciate my thesis supervisors, Dr Loranne Vernisse, Prof. Christophe Coupeau and Dr Michel Drouet, for all the support given to me during my years of doctoral studies. I would like to immensely thank them for their useful advice and constructive remarks they gave me and for their kind words of encouragement during several challenging moments. Words would fail me to describe the positivity and boost I got from all of them every time I felt overwhelmed by the challenges of the research. Their assistance in ensuring that my stay in France is hitch-free despite the rigour of research and administrative bureaucracy is deeply appreciated. The simplicity and ease with which they transfer their knowledge and ideas while ensuring high standards and thoroughness will forever be appreciated.

I would like also to thank the reviewers, Prof. Philippe Leclere and Dr Guillaume Parry as well as other members of the jury, Dr Arnaud Claudel and Prof. Boniface Kokoh for accepting to examine my work and for their interest in the results of this manuscript.

I am grateful for all the support I got from members of the Nanoplast team, both past and present. Special appreciation goes to Dr Michel Drouet who taught me very devotedly, the operations and manipulations of the Nanoplast device without ever complaining. I would like to also appreciate Dr Dimitri Chauraud who, in the early days of my studies, supported me in some experimental activities despite the stress of his thesis. I also wish to appreciate Dr Simon Smalley who was more than a team member, but also a friend and companion. I will always cherish the moments we shared. Special thanks to Fabrice Berneau who ensured the smooth running of the Nanoplast software.

My gratitude also goes to other members of the P' institute; Dr Julien Durinck for his robust contribution and brilliant insight particularly in the explanation of the sliding phenomenon. I also

wish to thank Prof. Christophe Tromas for dedicating some good time out of his busy schedule to explain the operations of the Mamouth device from where I got a huge part of my experimental data. My deep gratitude goes to Bruno Lamongie for the design of a manual straining device which was integral to the success of my experiments. I appreciate the assistance of Dr Nadia Guignard of the IC2MP laboratory in carrying out Raman analyses on our samples. I also thank the workshop team, Claude Veillon, Patrick Tanguy and Nicolas Desseigne, for fabricating devices and device parts which I needed in the course of my studies. I would like to thank Marie-Noëlle Branlé who was always available to solve any challenge I had with my computer. Special thanks to Alicia Lecesve for being always there to help with all kinds of administrative challenges.

I would like to thank my colleagues, some of whom have completed their studies: Axel Zuber, Thibault Chommaux, Florian Brette, Charlélie Chil, Razvan Burcea, Yen Fred Woguem and Fakhry Muhammad. Also, special appreciation goes to Loïc Van Hoorde and Cécile Marsal, who were my office colleagues.Thank you all for the moments we shared.

Special appreciation goes to my friends around the country who at one point or another visited me to ensure I had some company, and my mental health was in good shape. Thanks to Dr Abiodun Ogunleke, Charity Ojo (I look forward to the commencement of your doctoral studies too), Emmanuel Idowu, Victoria, Kenny, Eniola and Huwa. I appreciate your support.

My appreciation also goes to members of my family, my lovely parents, Mr and Mrs Joseph Fodeke, my siblings; Oluwaseun, Adeola and Adeboola. I cherish your love, support and encouragement. I would also like to appreciate support and companionship (over the phone, of course) of my partner and friend, Susanna Orshio. I look forward to a beautiful future with you. Finally, my profound gratitude goes to the giver and sustainer of life, the Almighty God for His love towards me.

Contents

Acknowledgements iv

Table of Contents vii

Introduction 1

1 Sample Preparation and Characterisation 9

1.1 Techniques and Experimental Devices . . . 9

1.1.1 Experimental Techniques . . . 10

1.1.1.1 Atomic Force Microscopy (AFM) . . . 10

1.1.1.2 Scanning Tunneling Microscopy (STM) . . . 13

1.1.2 Experimental Devices . . . 13

1.1.2.1 Bruker's Dimension Icon AFM . . . 13

1.1.2.2 Nanoplast Test Bench . . . 14

1.2 MoS_2 Film Transfer . . . 16

1.2.1 Substrate Preparation . . . 19

1.2.1.1 Single Crystals Surface Preparation . . . 19

1.2.1.2 PEEK Surface Preparation . . . 21

1.2.2 PMMA-Assisted MoS_2 Film Transfer . . . 23

1.2.2.1 Method . . . 23

1.2.2.2 Sample Characterisation . . . 23

1.2.3 Direct Transfer . . . 27

1.2.3.1 Method . . . 27

1.2.3.2 Topography Validation . . . 28
1.2.3.3 Band Gap Validation . . . 30
1.2.3.4 Raman Characterisation . . . 32
1.2.3.5 MoS_2 on PEEK Substrate . . . 33
1.3 Summary . . . 35
1.4 Résumé en Français . . . 37

2 Buckling of MoS_2 films: a descriptive study 43
2.1 Experimental Procedure and Characterisation . . . 44
2.1.1 Substrate Characterisation under Compressive Stress . . . 44
2.1.2 Experimental Device and Protocol . . . 45
2.2 AFM Results . . . 47
2.2.1 Emergence of Straight-Sided Buckles . . . 47
2.2.2 Strain-Induced Cracks on Film . . . 49
2.2.3 Interactions Between Buckles . . . 52
2.2.3.1 Attraction and Wrapping of Progressing SSBs . . . 54
2.2.3.2 Coalescence of Buckles . . . 57
2.2.4 *In-situ* Cyclic Compression . . . 61
2.3 Summary . . . 62
2.4 Résumé en Français . . . 64

3 Analyses of Strain-Induced Buckling on MoS_2 Film 71
3.1 Thin Plates under Compression . . . 72
3.1.1 Föppl-von Kármán Model of Thin Plates . . . 72
3.1.2 The Straight-Sided Buckle (Euler's column) . . . 75
3.1.3 Influence of Substrate Elasticity on Buckling Phenomenon . . . 78
3.1.4 Effect of Film Sliding on Maximum Deflection . . . 81
3.2 Extraction of MoS_2 Young's Modulus from Buckle Morphology . . . 83
3.3 Strain in 2D MoS_2 Films . . . 86
3.3.1 Total Strain in MoS_2 Film . . . 87

3.3.2 Internal Strain in MoS_2 Film . . . 87
3.4 Analyses of MoS_2 Buckle Evolution . . . 89
3.4.1 Predicted Critical Buckling Strain Versus Observed Critical Buckling Strain 89
3.4.2 Determination of Interfacial Adhesion Energy . . . 90
3.4.3 MoS_2 Buckle Evolution . . . 92
3.5 Summary . . . 100
3.6 Résumé en Français . . . 102

Conclusion and Perspectives **109**

Bibliography **112**

Introduction

Understanding the properties of ultra-thin materials will unlock a wide range of opportunities in the technological revolution particularly in applications that involve the use of flexible electronics and nanodevices. The discoveries of carbon nanotubes and, subsequently, graphene (joint Nobel Prize in Physics in 2010 [1]) have attracted a lot of interest in the field of nanotechnology [2–4]. From then, several studies have highlighted its impressive properties, particularly its high conductivity (10^4 Ω $^{-1}$ cm^{-1}) [5] and Young's modulus (1.1 TPa) [6]. These superior properties make it a suitable candidate for many applications ranging from energy storage to wearable electronics [5, 6]. However, due to the absence of a band gap, graphene is considered unsuitable in many applications such as logical circuits [7]. Therefore, there have been quests to study other two dimensional materials with similar properties as graphene, which also possess semiconductor properties.

Two-dimensional transition metal dichalcogenides (2D-TMDCs) are a class of materials with appealing properties which make them attractive for fundamental research into new physical phenomena and applications ranging from sensing to nanoelectronics and nanophotonics at the nanoscale level. Interests in 2D TMDCs have increased significantly in recent years, triggered by the demonstration of the first transistors [8] and the discovery of strong photoluminescence in MoS_2 monolayers [9]. They are semiconductors, chemically versatile with sizeable band gaps, and are found abundantly in nature [10]

TMDCs have a general formula MX_2, where M is an atom of a transition metal and X is an atom of the chalcogen family (S, Se or Te) [11] as shown in Fig. 1. In their bulk form, they have a repeated stacking of X-M-X unit with a hexagonal layer of M atom sandwiched between two layers of X atoms. Their electronic properties vary significantly depending on the numbers

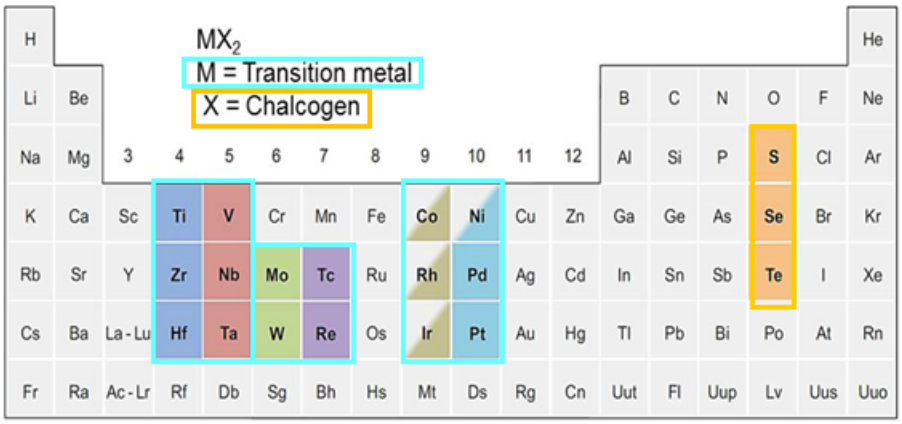

Figure 1: Periodic table with possible combination of elements for TMDCs compound: transition metals (highlighted in blue) and chalcogen elements (highlighted in orange) Image adapted from [11].

of *d*-electrons of M atoms hence, some TMDCs are insulators (HfS_2), semiconductors (MoS_2), semi-metals ($MoTe_2$), metals (NbS_2), or even superconductors ($NbSe_2$) [12].

TMDCs have a well-detailed history. Their structure was first determined and reported by Linus Pauling in 1923 [13]. By the end of the 1960s, about 60 TMDCs were reported with over 40 of them having layered structures [14]. In 1963, Robert Frindt reported the first ultra-thin MoS_2 fabrication using adhesive tape and by 1986 fabrication of MoS_2 monolayer suspension was achieved [15, 16]. The discovery of other TMDCs like WS_2 nanoparticles were also reported in parallel [17]. The rapid growth of graphene-related research that began in 2004 has stimulated the development of techniques suitable for working with layered materials, paving the way for new research, especially in TMDCs in their ultra-thin forms. The impressive properties of these materials have made them a delight for researchers for potential scientific and industrial applications, particularly in the electronics field. An important building block of modern electronic circuits is the field effect transistor (FET) and materials for transistors are required to have high charge carrier mobility and on/off ratios.

Among other TMDCs, researchers have recently been exploring the use of single layers of MoS_2 in functional electronic devices where they have shown advantages over graphene and silicon [18]. Coupled with its outstanding mechanical and optical properties, MoS_2 thin films have become viable candidates in flexible nanoelectronics applications [19]. This material offers a compelling possibility for technological innovation, especially in devices where components are expected to be ultra-thin functional materials with high efficiency.

Molybdenum disulfide (MoS_2) is a well-researched member of the TMDC family. The multi-layered form has been used as a solid lubricant for centuries [20]. As shown in Fig. 2, it is a layered material consisting of a molybdenum atom sandwiched between two sulphur atoms held together by a strong in-plane covalent bond [21]. Its atomic layers with hexagonal lattices are held together by adhesive van der Waals forces which allow layers to easily slide over one another thereby causing shear along the basal plane of MoS_2 crystals [22]. This explains its super lubricity property, hence the reason it has been used as a solid lubricant for many years. Generally, each layer (consisting of three atomic planes) has a thickness of about 0.65 nm [23].

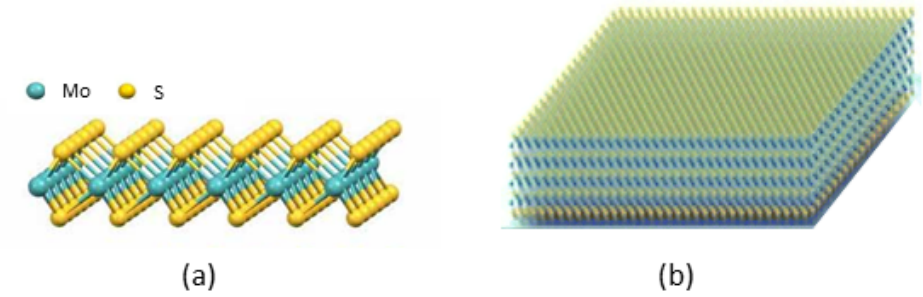

Figure 2: Crystal structure of MoS_2 (a) Monolayer MoS_2 showing a layer of molybdenum atoms sandwiched between two layers of sulphur atoms. (b) Multilayer of MoS_2.

MoS_2, like other TMDCs, possesses different polytypes. Three main polytypes of MoS_2 crystals experimentally determined are 1T, 2H and 3R. The digits represent numbers of monolayers in a unit cell and the letters represent structural symmetry with T as trigonal, H as hexagonal and R as rhombohedral. The 1T phase has an octahedral Mo-S coordination, while the 2H and 3R phases have trigonal prismatic coordination [24]. While the 2H phase found in naturally existing MoS_2 crystals is thermodynamically stable, the 1T and 3R phases are only meta-stable and mostly found in synthetic MoS_2 [25]. Due to their stability, 2H crystals are used for this work.

Many of MoS_2 impressive properties depend on the material thickness, as it has the ability to transition from an indirect band gap in its bulk or multi-layer form to a direct band gap as it reaches nano scale. This makes it possible to take control over the electrical properties of the material and gives it an edge over graphene in terms of applications. The band gap transition is dependent on quantum confinement, interactions between layers and Coulomb effects. In its bulk form, MoS_2 has an indirect gap of 1.2 eV between the maximum valence band (VBM) and the minimum conduction band (CBM) displaying metallic properties. As the number of layers

decreases, the values of VBM and CBM change, thus causing a variation in the gap value between them. A single layer of MoS_2 has a direct gap value of 1.8 eV between the VBM and CBM and displays semiconductor properties [9]. It is also possible to toggle between the n-type and p-type semiconductors by intercalation of doping elements.

MoS_2 has been predicted to possess impressive mechanical properties essential for application in nanodevices through limited experimental analyses, but various numerical analyses and molecular dynamics simulations have given insight into some outstanding properties of MoS_2 film. Experimentally, characterisation of the Young's modulus of MoS_2 has so far been limited to the use of nanoindentation technique [26], a technique adopted to characterise the mechanical properties of thin films after it was used for the measurement of elastic properties of monolayer graphene [27]. Reports from this technique indicate that the Young's modulus of single layer MoS_2 is about 270 ± 100 GPa [26, 28].

Monolayer MoS_2 has a high out of plane flexibility and a high tensile strength and can withstand a tensile strain of up to 11% before rupture [26]. Applied strain is capable of modifying the properties of MoS_2. For instance, the band gap of MoS_2 is tunable when highly strained and consequently results in the modulation of its electrical conductivity. Theoretical studies predict that straining the material up to 10% biaxial strain can lead to a complete band gap closure [29, 30]. With a tensile strain of 3% applied by bending the substrate using a customized sample holder, the direct band gap of monolayer MoS_2 was reduced to its bulk value, 1.2 eV [31]. Straining this material is further expected to alter its electrical properties [32], dielectric properties [33], thermal conductivity [34], and spin-orbiting coupling [35].

The several applications of MoS_2 earlier highlighted will require a controlled mechanical stability of the material under severe conditions. The understanding of how MoS_2 thin film responds to stress/strain is therefore critical. A lot of research has been carried out on the response of films to applied stress, particularly metallic films with thickness ranging from hundreds of nanometers to few micrometers. Results from these studies have helped to determine some mechanical properties of these materials.

When a film is under compression (internally or externally induced), it undergoes several relaxation mechanisms. The film, for instance, can adopt a wavy configuration [36]. Plastic

events such as the formation of epitaxial dislocation can also occur [37]. Rupture mechanisms can also occur at the film-substrate interface causing the film to delaminate from its support [38]. Finally, due to its low thickness, the film under compression may buckle which then leads to an increase in the delaminated zone.

There are different morphologies of buckling structures. Among them, three are highlighted in Fig. 3. The most basic form is the circular blister (or bubble) [39, 40] shown in Fig. 3a. Another is the telephone cord buckle [41] (Fig. 3b). From the name, the buckles progress by forming zigzag patterns on the sample surface. Research has also shown that telephone cord buckles can be formed due to instability of the straight-sided buckle [42], as shown in Fig. 3c.

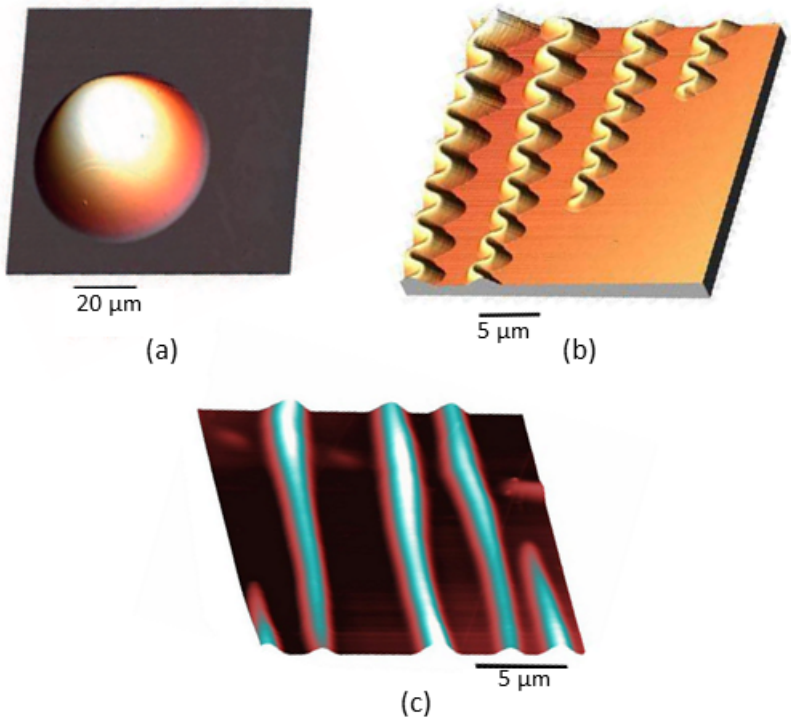

Figure 3: AFM images of (a) a circular blister of 630 nm Au film on Si substrate [40], (b) telephone cord buckling structures observed on a Y_2O_3 film of variable thickness (30-50 nm), deposited on GaAs [41] (c) straight-sided buckles structures observed on the surface of a 100 nm thick nickel film deposited on polycarbonate [42].

The most frequently generated buckling structures are the straight-sided buckles which may be induced by externally applied stress, lying perpendicular to the compression axis. The morphology of this buckle is relatively simple thus, making them easier to study [43, 44]. The straight-sided buckles are of rectilinear shape with a sinusoidal profile. Irrespective of their structure type,

observations show that the height of buckles (called deflection hereafter) is an order of magnitude smaller than their width, giving them a flattened appearance. Several parameters play a major role in the buckling process. The intensity of the stress/strain in the film (either internal or externally applied, or both) could favour this phenomenon. Also, the thickness of the film contributes to the magnitude of both the width and the deflection of the buckle. The adhesion of the well-bonded film to substrate appears as a limiting factor which has to be subdued before buckling occurs [45].

All of these buckling phenomena of thin plates have been studied and well described based on the thin plate model developed at the beginning of the 20th century by A. Föppl [46] and T. von Kármán [47] (referred to as FvK). The theory makes it possible to understand the mechanical properties of the plate under stress based on the buckling phenomenon and has been used to determine the elastic properties of metallic thin films which generally differ from those of the same materials at the bulk state [48, 49].

In this context, our research aims to study the mechanical response of 2D nanosheets of MoS_2 under externally applied stresses. Indeed, designing experimental protocols and data acquisition at nanoscale are challenging hence, there are only few available information in the literature in this regard. It appears, therefore, logical to draw a parallel between the behaviour of 2D sheets and the established behaviour of metallic thin films under compression by taking advantage of the buckling phenomenon using the FvK theory of thin plates. Understanding the behaviour of the buckles will also help in predicting the response of 2D materials to varying compressive strains which, of course, is critical to the deployment of these materials for various applications.

To accomplish afore mentioned aim, as-synthesised MoS_2 film will be transferred from its growth substrate to other substrates of interest which are capable of withstanding large compressive strain without failure. Thereafter, samples will be strained by compressing the substrates. This is with an expectation that the compressive stress is transferred to the deposited film which will induce delamination and buckling of the film. The structures and interactions of the buckles will be studied and analysed.

The manuscript is organised as follows: Chapter one focuses on the sample preparation techniques used for this research. Equipment and their working operations are first described. Sample preparation entails the transfer of MoS_2 films from growth substrates to other desired substrates.

Several methods have been suggested and used for the transfer of 2D materials and we demonstrate the most reported technique. Samples prepared by this method are characterised and drawbacks are highlighted. We, therefore, propose and demonstrate a new transfer technique for MoS_2 films (single layer and 3 layers) from growth substrate to metallic and non metallic substrates with interesting outcome.

In the second chapter, we describe the experimental procedure of sample compression after which results from atomic force microscope are presented. The features of the morphology of the buckle are discussed with specific attention to the lateral growth, reduction of the buckle width based on the applied strain in the system and strain-induced cracks on the film. Interactions of straight-sided buckles propagating in opposite directions are also discussed.

Finally, in the third chapter, we describe the FvK theory of thin plates and the Euler's column. The experimental results are analysed based on these theories. A critical strain beyond which buckle is observed is noted. The impact of substrate elasticity and how it affects the transfer of stress to the film is also examined. We will attempt to extract the Young's modulus of the film using the induced buckle morphology. We will also attempt to quantify the possible sliding phenomenon of such 2D-materials on substrates and examine how buckling is impacted.

Chapter 1

Sample Preparation and Characterisation

Contents

1.1 Techniques and Experimental Devices 9
1.1.1 Experimental Techniques 10
1.1.2 Experimental Devices 13
1.2 MoS_2 Film Transfer 16
1.2.1 Substrate Preparation 19
1.2.2 PMMA-Assisted MoS_2 Film Transfer 23
1.2.3 Direct Transfer 27
1.3 Summary 35
1.4 Résumé en Français 37

1.1 Techniques and Experimental Devices

The research work carried out during this thesis benefited from characterisations by surface analyses and scanning probe microscopy. Most of the experimental investigations were carried out on a Bruker Dimension Icon AFM device with an incorporated compression device. Other investiga-

tions were carried out using a unique test bench called Nanoplast, which combines an ultra-high vacuum STM/AFM and a mechanical stress device in compression. This instrument allows the *in-situ* observation of the surface of crystals at the atomic scale, at variable temperatures and under increasing applied deformation.

This chapter sets out to present the experimental techniques implemented during this thesis. First, we present brief descriptions of the experimental techniques used, then we describe the main characteristics of the experimental equipment. Surface preparation protocols necessary for good quality AFM and STM imaging, as well as the state of the substrate after preparation, are also mentioned. This chapter also examines some already established protocols for 2D film transfer from growth substrates to other substrates. We then present an optimised protocol for MoS_2 film transfer. Finally, the transferred films are characterised and analysed.

1.1.1 Experimental Techniques

1.1.1.1 Atomic Force Microscopy (AFM)

The AFM is a microscopic technique developed by Binnig, Quate and Gerber in 1986 [50]. It is used to image the topography of a sample surface by measuring the interaction force between an atom (or group of atoms) in the probe of the AFM scanning device and an atom (or group of atoms) on the scanned surface. The interaction force exists regardless of the environment or atoms concerned.

To make an image, a tip with a nanometric radius of curvature is mounted on a micrometric flexible lever arm known as a cantilever which forms a spring. The surface is swept by the tip which follows the topography of the sample, thereby inducing a deflection of the cantilever. In most cases, a laser beam is projected on the rear face of the cantilever and the reflection is collected on a four-dial photo-diode, which makes it possible to follow the variations of the cantilever deflection. The deflection of the cantilever induced by the interaction forces between the surface and the tip is then measured by the variation in the position of the reflected beam that it causes on the four-dial detector [51].

There are plenty of scanning AFM modes. In this thesis, we used the non-contact (NC) mode and Peak Force Tapping (PFT) mode. In the NC AFM, which is a commonly used mode, the

probe scans an area of the sample surface with the distance between the probe and the surface being in the order of Angstroms. Van der Waals interaction between the probe and the surface causes the cantilever to oscillate and changes in the amplitude of the cantilever oscillation at a constant frequency just off the resonance frequency are recorded. The PFT mode is more recent and is better described in the following.

Peak Force Tapping® AFM

The Peak Force Tapping® (PFT) AFM by Bruker, developed by Pittenger *et al.* [52], is a relatively new operating mode of the AFM which operates with a wide variety of standard AFM probes. This mode is equivalent to the PinPoint™ by Park and Fast Force Mapping (FFM) mode by Oxford Instruments. In the PFT mode, the probe oscillates periodically below the resonance frequency of the cantilever typically with a peak to peak amplitude of about 300 nm in air. The oscillation brings the probe into periodic contact with the scanned surface for a short time (usually less than 100 μs) thereby exerting a pN-level oscillating force on the surface which is measured by the deflection of the cantilever [53]. The peak force is kept down to about 10 pN by a feedback loop at actuation rates up to 8 kHz. With the PFT mode, cantilever tuning is unnecessary and the force control keeps the integrity of the tip and sample intact while collecting high-resolution images. The schematic of the working principle of the PFT AFM is described in Fig. 1.1 which shows the modulation of the probe plotted as a function of time as the probe interacts with the surface in a single scan cycle.

When the tip is far from the surface, there is little or no force on the tip. As the tip approaches the surface, the cantilever is pulled by attractive forces which eventually overcome the stiffness of the cantilever causing it to snap-in and the tip makes contact with the surface. The tip remains in contact with the surface until the force reaches its maximum value. This is known as the peak force. The peak force is kept constant by the system feedback. Once the peak force is reached, the tip begins to withdraw and the force reduces to a minimum value. The value of the minimum force just before the tip detaches from the surface corresponds to the adhesion peak and this point is known as the pull-off point. Once the tip comes off from the surface, it is only affected by long-range forces which are very small or zero and then the cycle continues. The total time

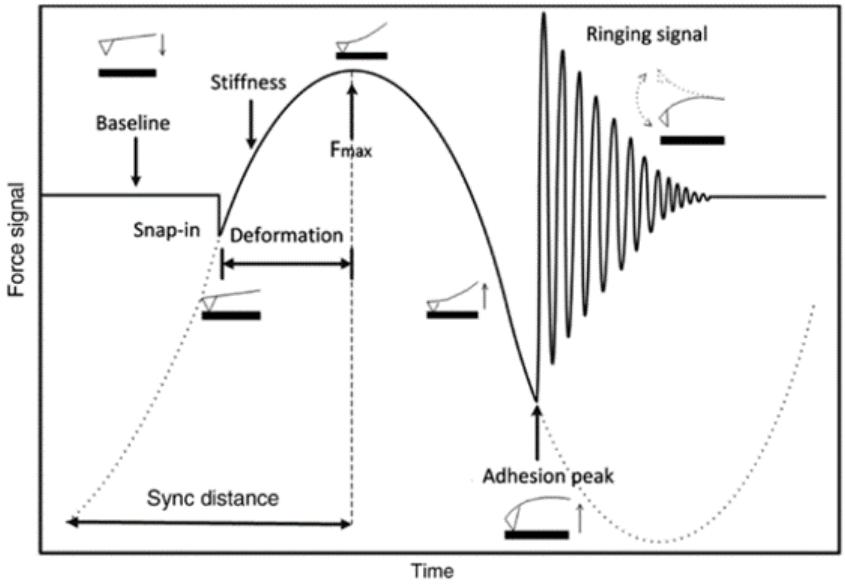

Figure 1.1: Schematic diagram of Peak Force Tapping mode of AFM for a single cycle. (Image from [54])

for a complete cycle could be as short as 0.5 ms [52].

The PFT uses a sinusoidal wave as the driving signal with a synchronization algorithm. With this algorithm, the maximum vertical interaction force (peak force) is extracted from half of the wave period set by the synchronization window. The maximum vertical interaction force is separated from the ringing signal and this allows the setpoint to be set to a small value. A second algorithm is employed to get rid of the background deflection signal which could occur due to environmental damping or rough sample topography [55]. The deflection signal is obtained when the probe lifts up to a certain height before each scan. The synchronization algorithm then effectively separates the tip-sample interaction region from the non-interaction region. An average of the non-interaction region is extracted from data obtained and constitutes a horizontal baseline. The baseline overcomes the effect of the ringing signal and allows the PFT mode to begin the next cycle without necessarily waiting for the ringing to be completely diminished. This enables the AFM to operate with a high scanning speed [54]. The PFT mode has an edge over the conventional tapping mode because it uses lowest force possible and has a better control of tip/surface interaction.

1.1.1.2 Scanning Tunneling Microscopy (STM)

The STM (or tunnel effect microscope) was developed in the early 1980s in IBM Zurich laboratories, Switzerland. It is the first local probe microscope to have enabled the possibility of having the atomic resolution of solid surfaces. First experiments on the STM were carried out by Binnig and Rohrer from which they were able to obtain images of silicon surfaces at the atomic scale [56,57]. The discovery of this technique and other its derivatives (including the AFM) earned them a Nobel Prize in Physics in 1986 [58].

The operation of the STM is based on the principle of the tunnelling effect. When the metallic tip (the probe) is brought very close (less than a nanometre) to a metallic or semi-conductive surface and a bias voltage is applied between the tip and the surface, a tunnelling current is detected. The current is proportional to the applied voltage and varies exponentially to the distance between the tip and the surface. It is usually in the order of nanoampere. The tip then sweeps across the surface by the means of piezoelectric tubes which ensure a lateral resolution of about 1 Å. The tip can maintain a constant distance from the sample surface throughout the sweep and the variations of tunnelling current (which is due to morphology and the electronic density of the surface) are recorded. This mode is known as the open loop mode. In another mode (close loop), the tunneling current is kept constant while the probe sweeps over the surface. The probe displacement in z will follow the lines of isodensity of current. The image created will be referred to as topographic image. Further details on the STM can be accessed in [59]. For the purpose of this research, STM characterisation was performed at a constant current.

1.1.2 Experimental Devices

1.1.2.1 Bruker's Dimension Icon AFM

The AFM device is housed in a vibration isolation compartment, as shown in Fig. 1.2. Apart from vibration isolation, the compartment also protects the sample from surface contamination and ensures an almost constant temperature and minimises thermal drift during scans.

The main components of this device include: a closed-loop scanner where the AFM probe is attached, a connector for application modules, a computer-controlled sample stage, an optical system which includes a USB camera and LED illumination.

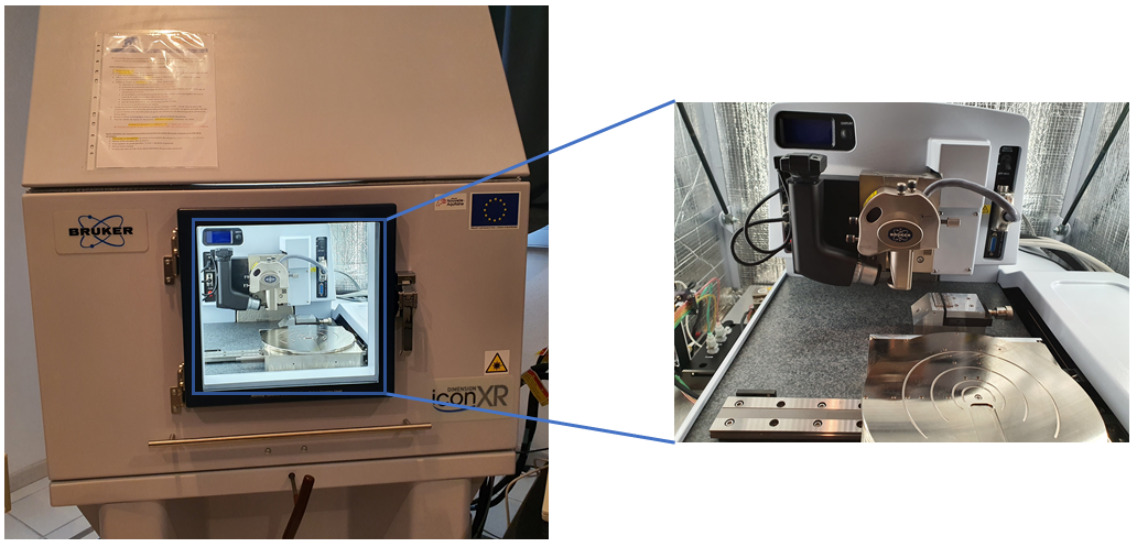

Figure 1.2: Bruker's Dimension Icon AFM with an incorporated manual straining device for sample compression.

The scanning mode is selected based on the type of probe used. In our case, PFT probes (material: silicon tip on nitride lever, tip radius = 2 nm, frequency = 70 kHz, spring constant = 0.4 N/m) were used. The operating software, Nanoscope, provides the possibility of using a unique tool called the ScanAsyst imaging mode. It is an image-optimization scanning mode for AFM. ScanAsyst continuously monitors image quality to ensure good and easy-to-understand images. It is capable of making necessary adjustments to scanning parameters. Set-point is optimised in such a way that the minimum force required to track the sample surface is used. Also, it uses a feedback loop which monitors and adjusts the gain to ensure that data quality is kept within a reasonable noise level. Scan rate can also be controlled, including the z limit [60]. All these are done while scanning with no input from the operator.

1.1.2.2 Nanoplast Test Bench

The Nanoplast test bench is a unique experimental device for surface probe microscopy analyses in an ultra-high vacuum (UHV) environment. It was developed by Pprime Institute and is fully described in the reference [61]. It was designed to follow *in-situ* the evolution of material surfaces by AFM/STM under increasing strain (with strain rate ranging from 10^{-6} s^{-1} to 10^{-2} s^{-1}), in UHV environment ($< 10^{-10}$ mbar) within a large temperature range (from 90 K to 600 K). The nanoplast test bench consists of three chambers as shown in Fig. 1.3.

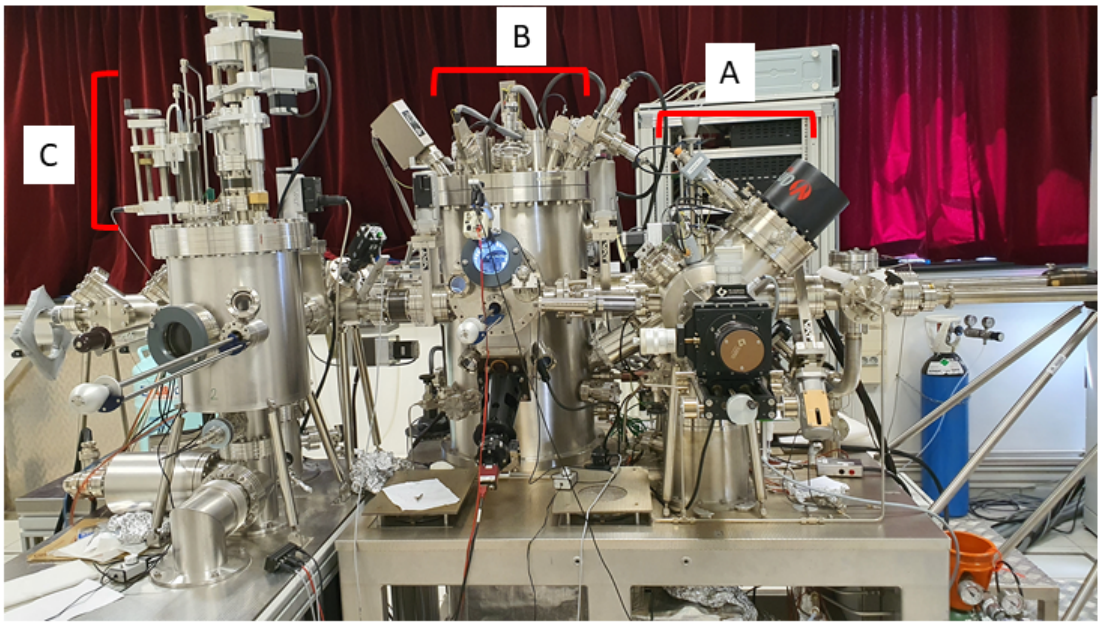

Figure 1.3: Nanoplast Test Bench. A: preparation chamber, B: in-situ mechanical test chamber with variable temperature (VT), C: variable temperature and ex-situ compression chamber

A load lock, which directly leads to the preparation chamber (A), allows samples to be introduced into the device. The preparation chamber includes a resistive oven which allows annealing up to 1200 K, and an ion gun for Ar ion sputtering (beam up to 5 keV). This makes carrying out several heating/sputtering cycles of sample surface possible to obtain good crystalline surface quality for AFM/STM investigations. The preparation chamber also contains two characterisation tools: a LEED (Low Energy Electron Diffraction) and an Auger spectrometer for chemical characterisation of samples.

The mechanical test chamber (B) houses a near-field microscopy system. The near-field microscope is an STM/AFM-VT [62] designed by Omicron NanoTechnology GmBH. The device makes it possible to follow the evolution *in situ* of the same zone of interest over a wide range of temperatures and to keep a high spatial resolution offered by the near field microscopy at high-stress levels (up to 500 MPa). The compression system comprises of two parts: an internal part and an external part. The external part is attached to the chamber and consists of two motors in a symmetrical configuration. The external compression configuration aims to reach any point of interest on a full strain/stress curve. However, the vibrations created by the external motors do not allow good quality imaging. Thus, as soon as the desired strain/stress level is reached, the

external motors are disengaged. The sample loading continues with the internal device through the elongation of two piezoelectric fixed to the stage of the microscope, thus allowing the imaging of AFM/STM in situ of the sample surface.

The third chamber (C) is dedicated to *ex-situ* deformation of samples at high temperature (up to 1300 K) and was not used in this work.

1.2 MoS_2 Film Transfer

Several methods are used for the synthesis and preparation of MoS_2 sheets and each method has its advantages and drawbacks as modification of structures and properties can be incurred. Methods used include mechanical exfoliation, vapour deposition, hydrothermal synthesis, sol-gel process, thermal decomposition, and others [63]. Industrial relevance and applications of any material, including MoS_2, require the availability of large-scale production and this is a major challenge in the fabrication of MoS_2 nano-sheets.

After a successful exfoliation of graphene from bulk graphite, other 2D materials have been fabricated using the simple "scotch tape" method [64, 65]. This method, known as mechanical exfoliation, has been used to fabricate high-quality monolayers suitable for research purposes [8]. However, the inability to control sheet size and the number of layers are major drawbacks. Larger MoS_2 sheets have been reported through chemical exfoliation technique. This technique is based on ion intercalation and solvent-based exfoliation. Anions or cations in solution are driven between layered bulk material by chemical or electrochemical reaction. This leads weakening of interlayer van der Waals bonds and the widening of the layers. Layers are eventually separated by subjecting the bulk MoS_2 to water treatment by ultrasonication. Solvents like ethanol, methanol and isopropyl alcohol can be used as water replacement with slight heat. Although larger sheets (up to 400 μm^2) can be obtained using this technique, it takes up to three days of reaction time. Also, intercalation process is difficult to control and there are lots of defects in the lattice structure of the produced MoS_2 flakes [63].

Another fabrication method that has gained popularity and acceptance in recent years is the chemical vapour deposition method (CVD). It is efficient in the preparation of 2D materials with large area uniformity, ensuring the fabrication of continuous layers with specific film thickness. It

can be used to synthesise wafer-scale films [66] which makes it promising for applications like large-scale integrated electronics. It is also applicable in the preparation of layered heterostructures and prevents contamination at interfaces between different layers since no transfer process is required during such growth. The basic schematic diagram of the CVD process is shown in Fig. 1.4.



Figure 1.4: Schematic diagram of chemical vapour deposition method.

The growth substrate is pretreated so as to improve the ability of the substrate to adsorb precursor materials, aid material nucleation, and stimulate material epitaxial growth [67, 68]. At the basic level, sulphur is heated to over 120 °C and its vapour is made to flow through a quartz tube, with nitrogen gas, where an Mo-based compound is heated at a high temperature (around 750 °C). Mo precursors used include ammonium thiomolybdate solution [$(NH_4)_2MoS_4$], molybdenum trioxide powder [MoO_3] and elemental molybdenum [69–71]. Mo is evaporated on the substrate after which sulfurisation takes place. MoS_2 crystal grain sizes are dependent on the type of substrate used. Sapphire substrates have been reported to grow larger crystals than SiO_2 [63]. Other substrates like strontium titanate (STO) [72] and mica [73] have been used to grow MoS_2 sheets.

The limitation of the substrate type for material growth makes it necessary to transfer the as-synthesised film to other substrates for various applications and characterisations. In order to characterise and study the behaviour of MoS_2 thin films under stress, there is a need to transfer the films from their growth substrates to other desired substrates with favourable elastic properties. This will allow compression possible without damaging the sample. The transfer is expected to be carried out in such a way that the morphological properties of the film are preserved.

Several methods have been proposed and used for the transfer of MoS_2 films and other 2D materials from their growth substrates to other desired substrates. The most commonly used method involves coating organic films on the MoS_2 films to serve as a support layer. Organic films that have

been reportedly used include polymethyl methacrylate (PMMA), polydimethylsiloxane (PDMS), polyvinyl alcohol (PVA), polyvinyl acetate (PVAc), rosin, and many others [74–78]. After deposition, the growth substrate is removed either by chemical etching or by induced delamination through ultrasonic bubbling. The film with supporting coating is then transferred to the surface of the desired substrate.

Many of these techniques have their particular drawbacks however, some challenges common to all include: introduction of impurities, poor surface quality, roughness, complicated and long-duration procedure. Another challenge is the separation of the growth substrate from the film/support-layer stack. For instance, substrate etching was proposed for PVAc-assisted transfer [77]. However, film foldings occur during the transfer process and the etching also leads to film quality degradation [79,80]. Therefore, substrate removal through an ultrasonic bath is preferred. This technique introduces no hazardous pollutant to the sample or environment and can guarantee the integrity of the crystal quality of the transferred film to a large extent. Additionally, it encourages the preservation and reusability of growth substrates thereby reducing waste and production costs [74]. However, a major challenge for this technique is the removal of the organic coating from the film surface in such a way that no residue is left on the free surface and the overall quality of the MoS_2 film is preserved.

Samples used in this study were prepared by CVD grown MoS_2 films on SiO_2 and sapphire substrates and transferred to metallic and non-metallic substrates. The use of metallic substrates allowed for electronic characterisation of the transferred MoS_2 films and non-metallic substrates allowed samples to be compressed over large strain. In this section, we describe the methods used in the preparation of substrates for the film transfer. We also demonstrate two transfer techniques by experimentation. The first is the PMMA-assisted transfer which has been widely used and reported in the literature. In order to reduce (or eliminate) residue on the film surface, we improved the sample cleaning protocol. We also propose and demonstrate a new protocol for a direct transfer of MoS_2 from their growth substrates to several substrate of interest. The new protocol is such that the prepared surface is clean and devoid of external contamination. It guarantees the morphological integrity of the material and can be used for several substrates as desired. This technique is an optimisation of the already existing technique but does not require

a support layer or chemical etching. Prepared samples were characterised using several surface characterisation/analysis techniques and the results are discussed.

1.2.1 Substrate Preparation

For the purpose of this work, surfaces of substrates intended for use for MoS_2 film transfer are required to be clean, homogeneous and flat. Hence, they have to go through specific surface preparation cycles. We selected both metallic and non-metallic substrates for the film transfer. Surfaces of metallic substrates are prepared by polishing, argon ion sputtering and annealing, while the surface of the non-metallic substrate was prepared by specific polishing procedures. Substrates used for the MoS_2 film transfer are Cu(100), Au(111) single crystals and polyether ether ketone (PEEK) substrates. All samples were cut to fit into the Nanoplast sample holder with a cross-section of $2 \times 2\ mm^2$ and length 6 mm.

1.2.1.1 Single Crystals Surface Preparation

Single crystal metallic substrates underwent a surface polishing procedure and several cycles of ion bombardment and annealing under a UHV environment in the preparation chamber of the Nanoplast test bench in order to obtain a good quality crystalline surface for STM imaging. Cu(100) and Au(111) single crystals were prepared using similar surface preparation procedures. Therefore, only Cu(100) surface preparation is described.

For the polishing process, the substrate was firstly subjected to lapping using waterproof abrasive papers as lapping pads. The mesh size of the abrasive paper was gradually increased from 800 to 2400. During lapping, the force was 5 N and the rotation speed of the lapping pad was 50 rpm with a lapping time of 2 minutes for each abrasive paper. After lapping, the abrasive paper was replaced with a leather pad for polishing. For the polishing rounds, the grain size of monocrystalline diamond suspension was reduced from 3 μm to 1 μm at a polishing speed of 150 rpm and 15 minutes per round. The procedure was completed by using OP-U active oxide suspension for final polishing. This was done to reduce scratches and defects on the polished surface. The sample was thereafter cleaned and dried in deionised water and compressed air respectively before insertion under UHV for surface cleaning.

Ion bombardment is a method of cleaning and preparing a surface by removing contaminants present on it. To do this, accelerated argon ions bombard the surface at normal incidence and expel the contaminants. Lowering the acceleration of argon ensures minimal penetration of ions into the material. Sputtering, therefore, occurs by collisions between the ions and the surface atoms. After the ion bombardment, it is important to carry out annealing to evaporate surface impurities, remove ion bombardment traces and to reconstruct the surface by the diffusion of atoms.

The protocol used for Cu(100) monocrystal sputtering was to accelerate argon ions to a voltage of 0.6 keV with an emission current of 6 μA at 1.8 x 10^{-5} mbar pressure for a period of 10 minutes and then annealed at 450 °C for 45 minutes to remove surface contamination and ensure a clean surface. A 150×90 mm^2 STM image of the prepared Cu(100) monocrystal substrate surface is shown in Fig. 1.5.

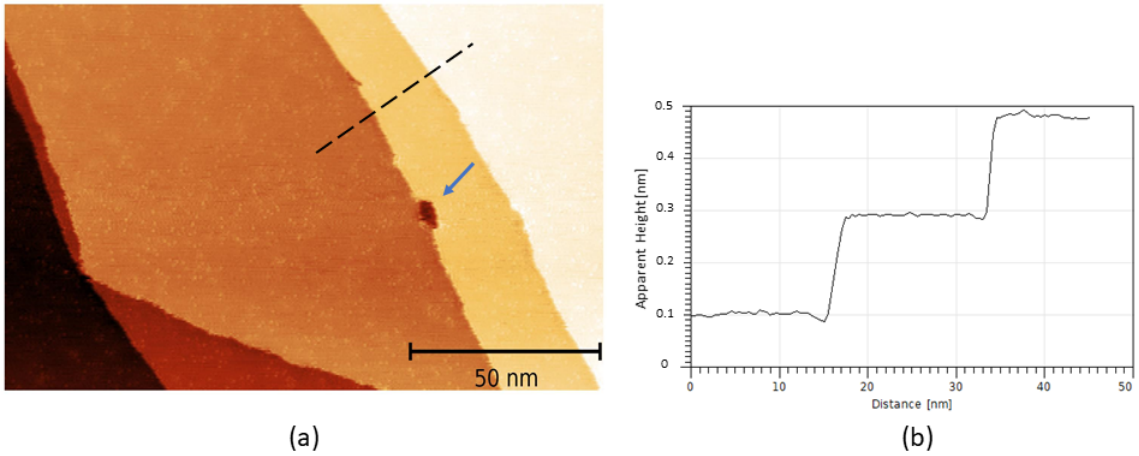

Figure 1.5: Cu(100) surface after preparation: (a) STM image showing terraces and Cu(100) steps ($V_b = 1\,V$, $I_t = 1\,nA$, RT). (b) Surface profile obtained perpendicular to local steps.

The STM investigation of the Cu(100) surface after several preparation cycles reveals the surface is largely clean and flat. Few defects, sparsely distributed across the surface, were observed (one of such is indicated by an arrow in Fig. 1.5a). However, large terraces without defects were observed across different regions of the sample surface. Data from a line profile across three terraces in close proximity (indicated by the black broken line in Fig. 1.5a) is plotted and shown in Fig. 1.5b. It shows a step height of 0.18 nm characteristic of Cu(100) [81]. This validates our surface preparation protocol to a large extent and thus, the substrate is suitable for MoS_2 film

transfer.

1.2.1.2 PEEK Surface Preparation

PEEK 450G^{TM} purchased from Victrex^{TM} was cut into substrates of 2×2 mm^2 cross-section and 6 mm length. Polishing protocols for PEEK are not well discussed in the literature as it is mostly utilised as a biomaterial for orthopedic, body implants and removable dentures [82]. For these purposes, polished surface of PEEK is only required to have a threshold of 0.2 μm of surface roughness [83]. This value is higher than what is required for our work hence, we decided to use a different surface preparation protocol to achieve a flatter surface for MoS_2 film transfer. To do this, some PEEK samples were sent to Surface Preparation Laboratory (SPL) in the Netherlands, a laboratory which specialises in preparation and characterisation of crystalline surfaces and interfaces. Other samples were polished in the sample preparation room of Pprime Institute.

For the polishing performed in our lab, we used Mecatech 234 from Presi SA automatic polishing device. The polishing began with the choice of TOP, Reflex PAD-MAG polishing fabric from Presi, made from plasticised acetate silk taffeta for levelling of the sample surface. With a polishing time of 5 minutes and a force of 10 N, the polishing speed was set at 250 rpm and diamond suspension of 10 μm grain size was intermittently supplied to the polishing pad. For the next polishing round, RAM, Reflex PAD-MAG polishing fabric and 3 μm diamond suspension were used. Similar polishing parameters were used as it was in the first round. The procedure was completed by using an NT, Reflex PAD-MAG polishing fabric and $\frac{1}{4}$ μm diamond suspension. The sample was thereafter cleaned in deionised water and dried in compressed air. By visual observation, a highly reflective surface was obtained. AFM images of samples polished by SPL and in our lab are shown in Fig. 1.6.

The topography representative of a 5×5 μm^2 area of the sample surface prepared by SPL (shown in Fig. 1.6a) shows deep residual scratches from the polishing across the scanned area. A line profile (blue line in Fig. 1.6a) across the surface as shown in Fig. 1.6c gives an insight into the depths of the polishing scratches with some as deep as 45 nm. The proximity of the scratches gives no room for large terraces. The assessed surface profile's mean deviation (R_a) which represents

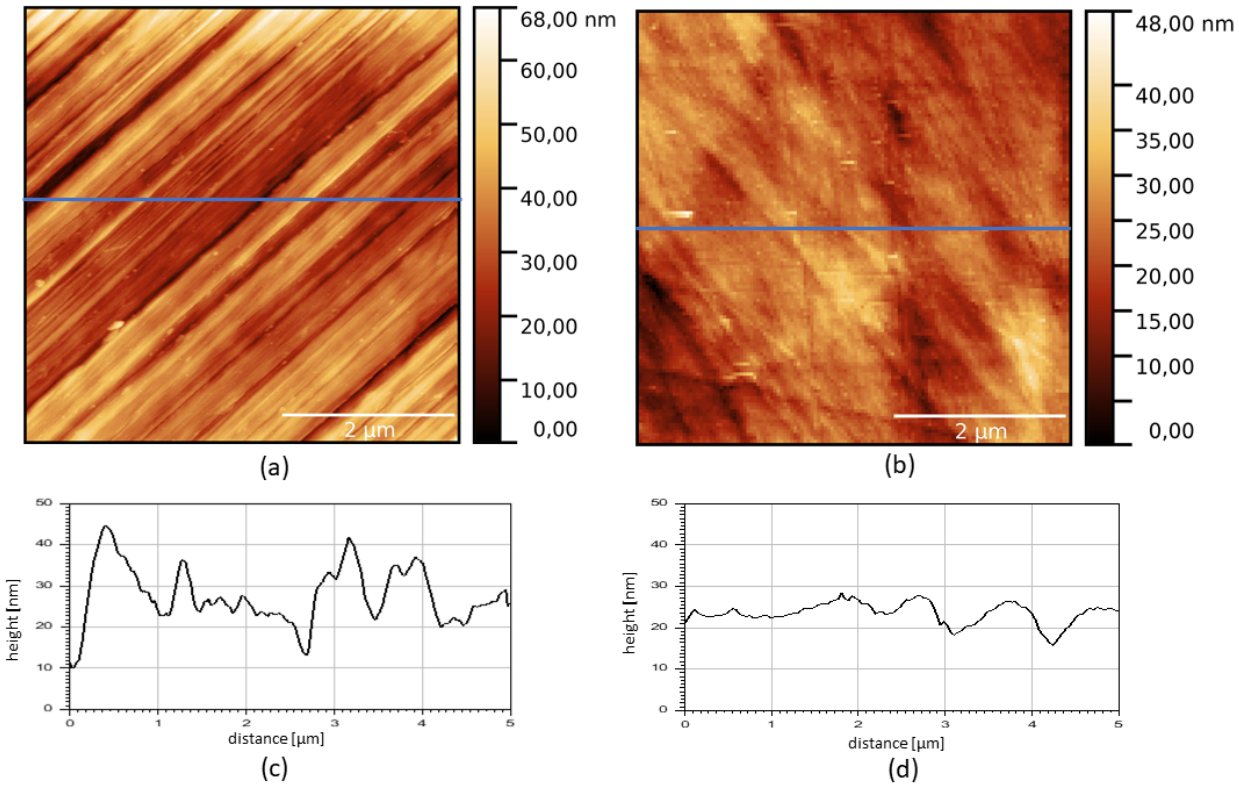

Figure 1.6: AFM images of polished surfaces of PEEK substrates: (a) PEEK sample prepared by SPL, (b) PEEK sample prepared at Pprime lab. (PFT mode, RT), (c) Surface profile of PEEK prepared by SPL, (d) Surface profile of PEEK prepared at Pprime lab.

the average surface roughness in two dimensions and the sample's mean surface height (S_a) which is the extension of R_a in three dimensions with a suppressed influence of directional scratches were measured using Gwyddion software. Results from the software indicate an R_a value of 9 nm and S_a value of 7.3 nm for sample A.

The topography of a 5×5 μm^2 area of the sample surface we prepared in the lab (shown in Fig. 1.6b) shows fewer polishing scratches. A profile (taken along the blue line in Fig. 1.6b) of the surface as shown in Fig. 1.6d indicates that polishing defects on the surface are less than 10 nm and sparsely distributed, therefore large flat regions are easily accessible compared to the previous case. Statistical analyses shows that the scanned region has an R_a value of 5.4 nm and S_a of 4.3 nm. The results presented show that the PEEK sample polished in our laboratory has a flatter surface than the sample prepared at SPL and therefore considered more suitable for the purpose of this work. That notwithstanding, both samples have lower roughness than samples whose preparation protocols have been reported in the literature [82].

1.2.2 PMMA-Assisted MoS_2 Film Transfer

1.2.2.1 Method

MoS_2 monolayer continuous films grown by CVD on sapphire were purchased from *Six Carbon Technology* and a commonly used transfer method as described by Ma *et.al* [74] was adopted. PMMA (4%) solution was prepared by dissolving PMMA powder (M_w = 350,000) in anisole (dichloromethane was avoided due to carcinogenic classification). The solution was deposited on the commercially acquired MoS_2/sapphire by spin coating at 1250 rpm for 1 minute. Fig. 1.7 shows a schematic illustration of the PMMA-assisted MoS_2 film transfer. The PMMA serves as film support. The PMMA/MoS_2/sapphire stack was cured at 180 °C for 15 minutes to remove residual solvent. After cooling in air, the stack was immersed in a beaker of DI water for ultrasonication and kept at 80 °C. The ultrasonication process induced several tiny bubbles at the MoS_2 - sapphire interface. These bubbles grew larger and collapsed, forcing delamination of the film from the growth substrate. Due to the hydrophilic nature of sapphire, water could penetrate the film-substrate interface. After a few minutes of ultrasonication, PMMA/MoS_2 was observed floating on the DI water surface. Using a pair of tweezers, the already prepared copper substrate was immersed in the DI water and placed directly below the floating PMMA/MoS_2 stack. By gently lifting the copper substrate from the bath, PMMA/MoS_2 was deposited on its surface. To ensure complete removal of PMMA from the MoS_2 surface, the sample was cleaned in 3 acetone baths inserted in water baths at 80 °C, an ethanol bath and an isopropanol bath. The cleaned sample was left in air to dry.

1.2.2.2 Sample Characterisation

Using the PMMA-assisted transfer protocol described earlier, monolayer MoS_2 on sapphire was transferred to an already prepared Cu(100) surface. The sample was taken into the nanoplast test bench for surface characterisation. To remove water molecules and other impurities from the free surface, the sample was heated in the nanoplast oven at 200 °C for 2 hours. After cooling, the sample was transferred to the test chamber for scanning probe microscopy (SPM) characterisation. The AFM images in Fig. 1.8 show monolayer MoS_2 on sapphire (growth substrate) before transfer (Fig. 1.8a) and on Cu(100) surface after transfer (Fig. 1.8b).

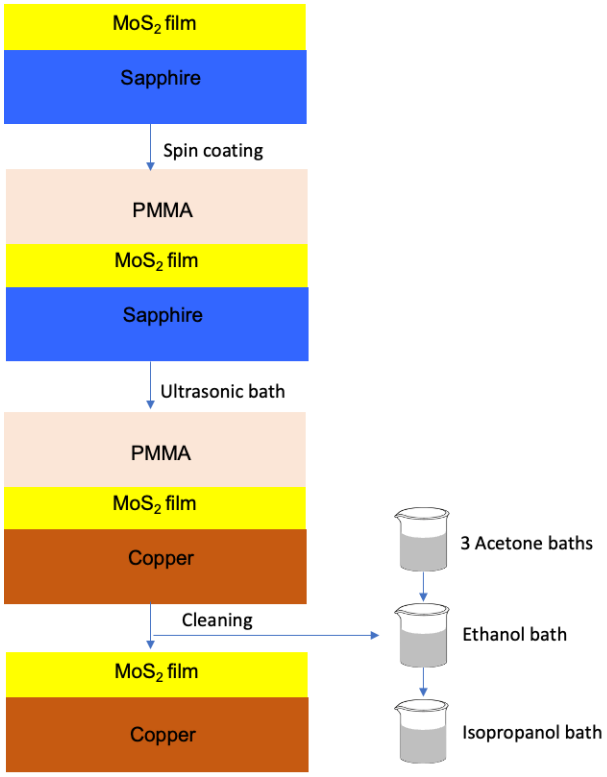

Figure 1.7: Illustration of PMMA-assisted MoS_2 film transfer from sapphire to copper

Fig. 1.8c shows a surface profile taken along the blue line on the MoS_2-sapphire surface. It shows that the monolayer has a thickness of 0.77 nm before transfer. The thickness measured is slightly higher than the theoretical value of 0.65 nm thickness reported in the literature [23], but it is in the range of other experimental characterisations. AFM scan of the transferred film taken under UHV as shown in Fig. 1.8b reveals surface cracks on the sample. Profile line drawn across the crack (Fig. 1.8d) indicates a crack depth of about 6.7 nm which is higher than MoS_2 film thickness. This suggests the possibility of multiple folding of the film during transfer and/or the presence of PMMA residue deposited on the film during the transfer procedure. It was suspected that despite several cleaning cycles and annealing under UHV, PMMA residue was not completely removed from the surface. The difficulty of removing the sacrificial layer has been reported in the literature with many concluding that it is impossible to completely get rid of the residue [84].

To ascertain the constituent elements at the free surface, the sample was characterised by low-energy Auger Energy Spectroscopy (AES) under UHV in Nanoplast preparation chamber. Auger electron spectroscopy for chemical analysis of surfaces is based on the Auger process. When

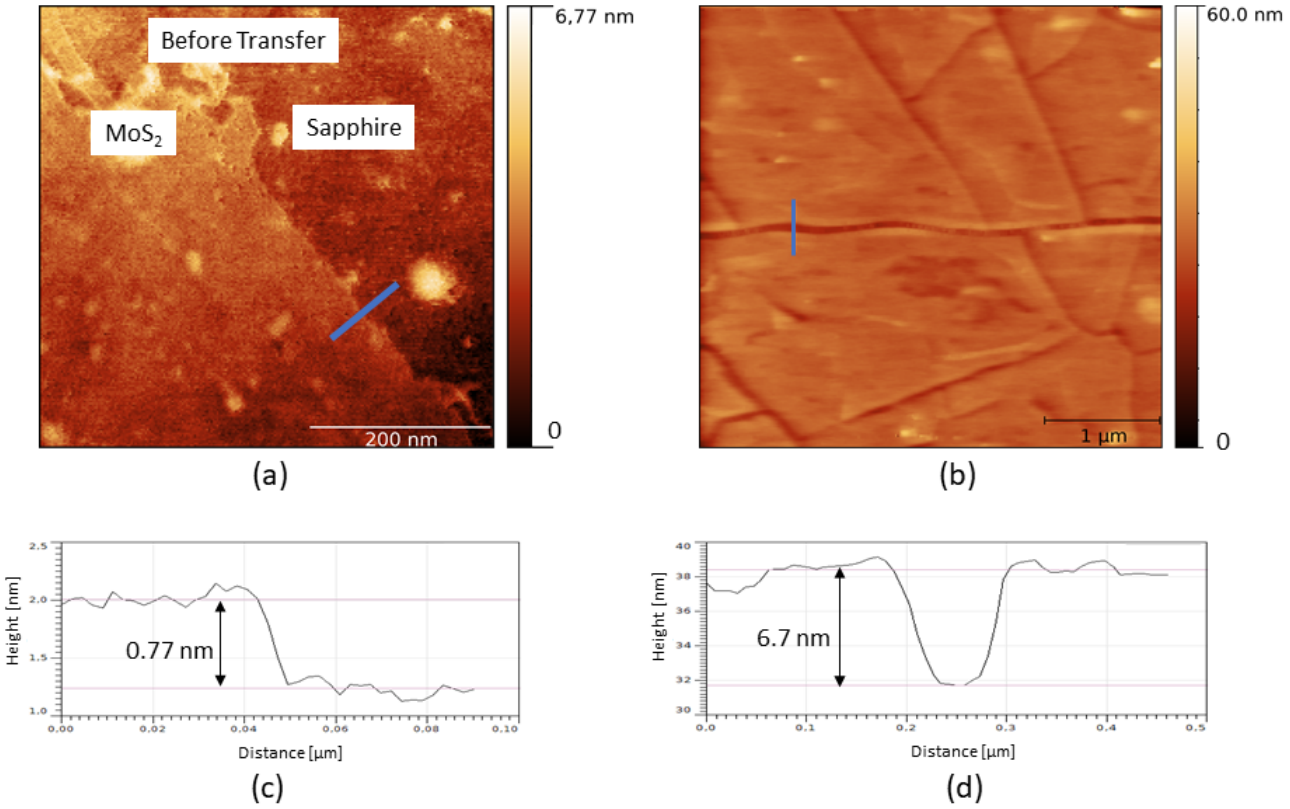

Figure 1.8: Single layer MoS_2 film transfer using PMMA-assisted technique. (a) AFM image (in air) of single-layer MoS_2 film on sapphire before transfer showing the MoS_2-sapphire boundary, (Peak Force Tapping mode, RT). (b) AFM image (in UHV) of MoS_2 film transferred to Cu showing deep cracks on its surface (Non-contact, Δf = -10 Hz, gain = 127%, RT), (c) Profile showing MoS_2 film thickness before transfer, (d) Profile showing the depth of the crack observed on the sample surface after transfer.

electromagnetic radiation from the Auger beam gun falls onto a core electron of the sample, the core electron gets excited and causes the electron to be ejected in the form of a photo-electron. This is known as photo-emission. Consequently, a hole is created in the core shell (the K shell). To fill the hole created, an electron from a higher level falls into the hole and during the fall, energy is emitted in the form of radiation. The radiation further excites another electron in the same sub-shell. The excited electron gets ejected and is known as an Auger electron. This phenomenon is known as Auger effect. This Auger electron has the kinetic energy characteristic of the parent atom. If the Auger transition occurs within a few angstroms of the surface, the Auger electrons are ejected from the surface without losing energy, resulting in a spike in the secondary electron energy distribution function. The shape and energy of these Auger features can be used to precisely identify the composition of the solid sample surface [85]. The AES spectrum shown

in Fig. 1.9 reveals peaks of binding energies of elements present in the analysed sample.

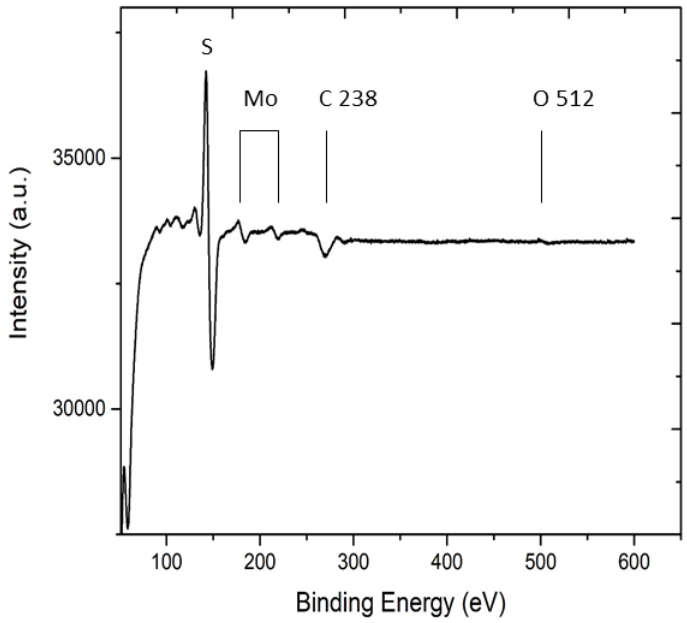

Figure 1.9: Low energy AES of transferred film showing carbon and oxygen peaks.

AES peaks were observed at 152 eV, 186 eV, 222.8 eV, 238 eV and 512 eV. These peaks correspond to sulphur, molybdenum, carbon and oxygen respectively with Mo having two peaks at both 186 eV and 222.8 eV [85, 86]. Copper peak is not shown in the figure as it is off chart at 920 eV. We expected that a clean and impurity-free surface would show vivid peaks corresponding to atoms of molybdenum and sulphur. Small peaks of carbon and oxygen were also expected due to the relatively non-polar nature of the basal plane of MoS_2 causing it to show affinity for hydrocarbons. Therefore small carbon peak is usually observed after exposure to air. Oxygen peak is also observed because of adsorption of water molecules on the non-polar surface [87]. However, the peaks of carbon and oxygen observed are higher than what would be expected on a clean and heat-treated surface. The intensities of the C and O peaks are similar to that of a contaminated MoS_2 surface as reported in [87], confirming the presence of carbon and oxygen atoms in relatively large quantities. The presence of carbon and oxygen atoms on the free surface confirms that the PMMA support layer was not completely removed from the sample. PMMA, which has a chemical formula: $(C_5O_2H_8)_n$, has a large molecular weight (350,000) and low solubility in solvents [88]. When subjected to high temperature in the absence of oxygen, as was done under UHV, PMMA

decomposes to its monomer, methyl methacrylate (CH_2=C(CH_3)$COOCH_3$) [89]. This explains why carbon and oxygen peaks were observed from the AES. One major limitation of the AES characterisation technique is its inability to analyse elements with less than 3 electrons since the process requires the involvement of 3 electrons (photo electron ejected by electromagnetic beam, an electron from to fill the hole created by the photo-electron, and the Auger electron). It is therefore impossible to observe any peak that corresponds to hydrogen [85]. However, we are confident that carbon and oxygen observed on the sample surface are residues from the PMMA support layer.

The film thickness measured from the surface cracks and the presence of oxygen and carbon atoms confirm the presence of PMMA residue on the transferred film. Despite the several cleaning protocols were adopted to remove PMMA residue from the free surface, there was no major improvement on the surface cleanliness. The presence of residue of PMMA has been reported to degrade the properties of 2D materials [90,91]. It, therefore, became imperative to develop a new transfer technique that would ensure an impurity-free surface instead of further improving the PMMA protocol.

1.2.3 Direct Transfer

1.2.3.1 Method

Due to the drawback recorded in the PMMA-assisted transfer technique, we developed a technique that guarantees to a large extent, a clean, impurity-free surface by eliminating the use of support coating. This was done by optimising the PMMA-assisted transfer technique as shown in Fig. 1.10. Firstly, the film on its growth substrate is inserted in a specially designed groove of a stainless-steel block and the polished surface of the target substrate is placed directly on the film. The stack is secured firmly using a high carbon steel piano string to keep the substrate in place during ultrasonication. The stack is then immersed in DI water for a few seconds of ultrasonication. The ultrasonication process causes MoS_2 delamination as previously explained. Film transfer from the growth substrate to our substrate of interest is encouraged due to the higher hydrophilicity of the growth substrate as compared to the film and the targeted substrate. Hence, the water at the interface forces the film to stay glued to the targeted substrate surface [80]. The sample is then

removed from the stack and allowed to dry in air.

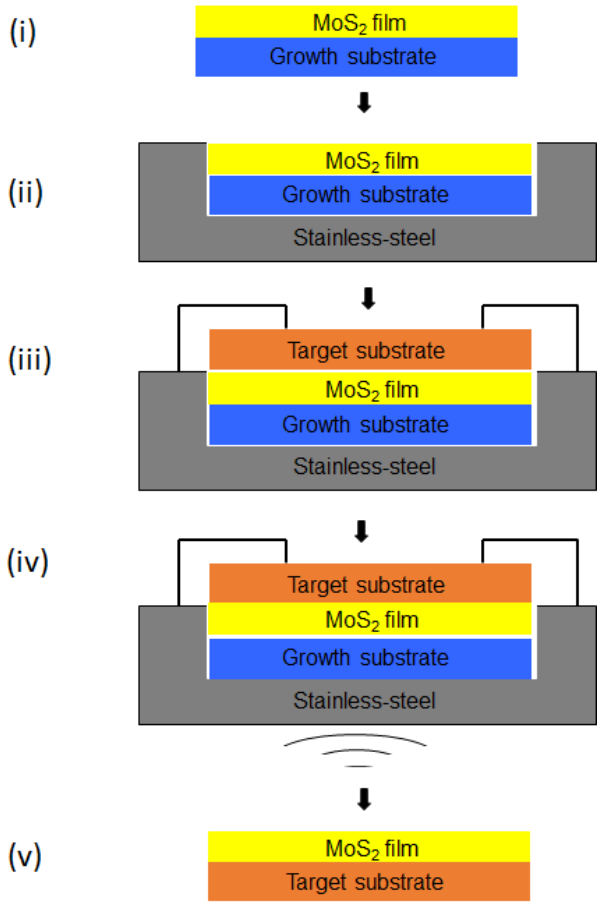

Figure 1.10: Illustration of direct MoS_2. (i) MoS_2 film on its growth substrate as purchased. (ii) The stack is inserted in the groove of a stainless-steel block. (iii) Target substrate directly placed on MoS_2 film and firmly secured with high carbon steel string to the stainless steel block. (iv) Ultrasonication of the stack in DI water to induce film delamination and transfer. (v) Transferred MoS_2 on target substrate

1.2.3.2 Topography Validation

Using the optimised direct transfer technique, monolayer MoS_2 film was first transferred to Au(111) substrate. After transfer, the prepared sample was heated in the nanoplast oven at 200 °C for 2 hours to remove any surface impurity and water molecules that may be present on the surface. After cooling, the sample was transferred to the mechanical test chamber of the device for further SPM characterisations. The STM image in Fig. 1.11 reveals the topography of the transferred film.

STM image of the sample taken around the edge of the MoS_2 film on Au in Fig. 1.11 gives an

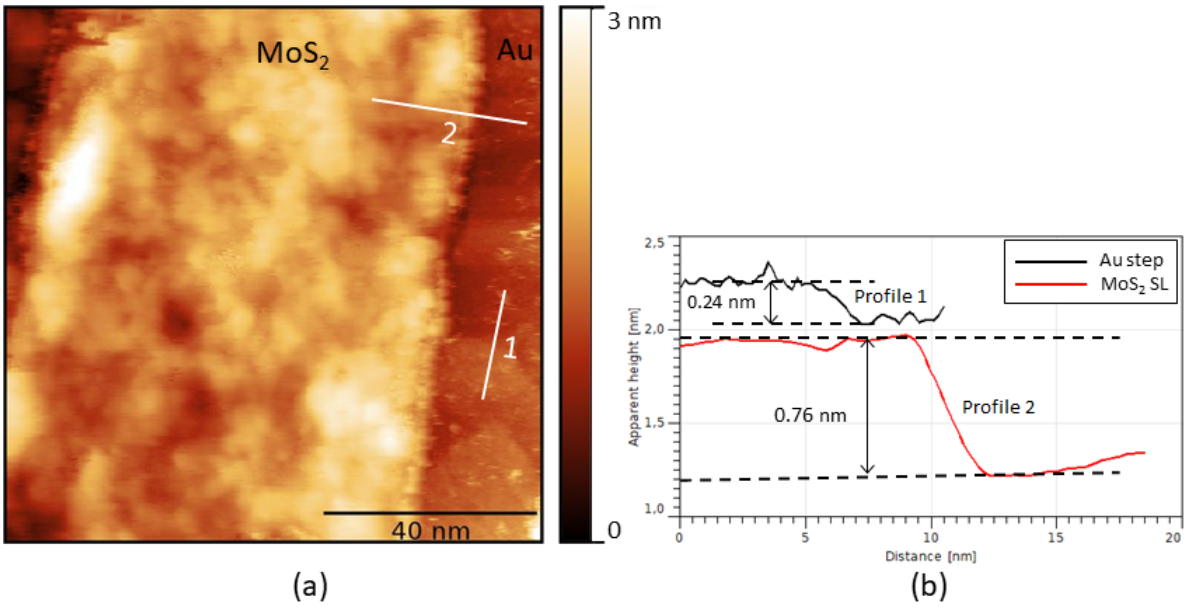

Figure 1.11: (a) STM image of a single layer MoS_2 film transferred to Au(111) using the direct transfer technique showing MoS_2–Au boundary ($V_b = 0.3$ V, $I_t = 600$ pA, RT), (b) Surface profile of the sample showing an apparent film thickness of 0.76 nm and Au steps of about 0.24 nm. Profiles are shifted for better visibility.

insight into the transferred film thickness. The scanned area, being the sample edge, has a lot of defects and that explains the cloudy contrast of the MoS_2 film. Nevertheless, the film edge and Au(111) steps are clearly visible. Variation in the height of the substrate terrace was measured by topographic profile (1) drawn across the substrate. The height (shown in Fig. 1.11b) is measured to be around 0.24 nm which corresponds to the height of Au(111) mono-atomic steps [92]. A topographic profile (2) taken from the MoS_2 surface to the substrate surface indicates (as shown in Fig. 1.11b) a film thickness of about 0.76 nm. This is in close agreement with the height of monolayer MoS_2 film [23]. To have a better resolution of the transferred film, a zoom on an MoS_2-only region is shown in Fig. 1.12.

The 50×50 nm^2 STM image in Fig. 1.12a shows a characteristic Moiré pattern which is a distinct marker of monolayer MoS_2 film on Au(111) with a regular periodicity of 3 nm as shown in Fig. 1.12b. The herringbone reconstruction of the Au(111) surface is lifted by the MoS_2 film which then causes an irregular orientation of the soliton lines around the MoS_2 film [93]. The film, which consists of a regular S-Mo-S stacking pattern hence, shows a lattice mismatch with the underlying Au(111) surface, forming a Moiré superstructure [94–96]. The STM images prove

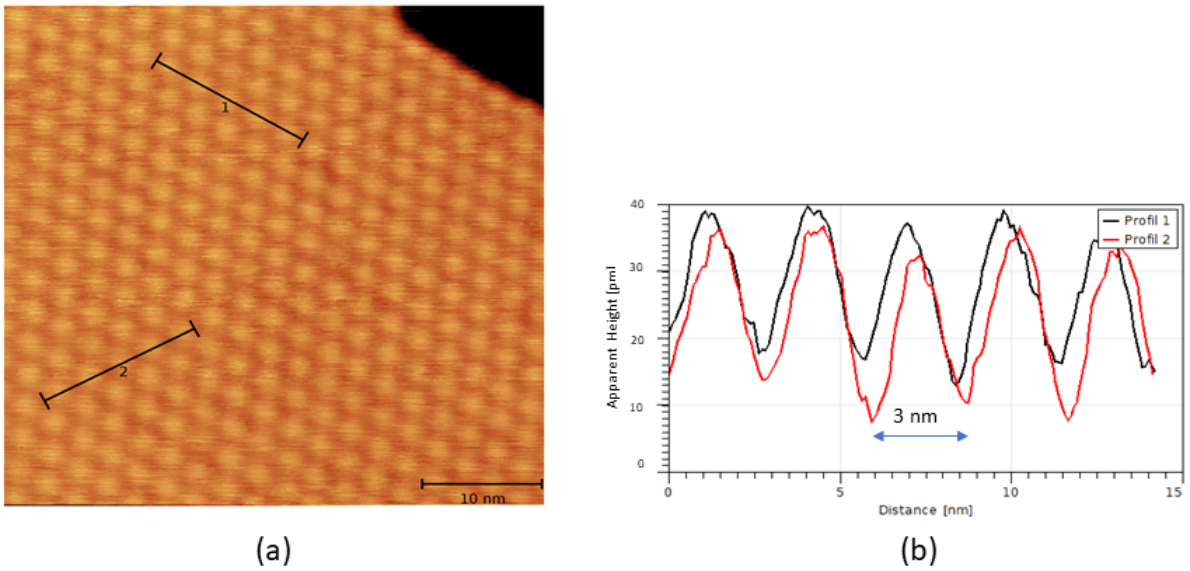

Figure 1.12: (a) STM image MoS_2 on Au(111) surface showing Moiré pattern ($V_b = 0.3$ V, $I_t = 600$ pA, RT), (b) Profiles of the Moiré with regular periodicity of 3 nm.

that MoS_2 single layer was indeed transferred to Au(111) surface with an appreciable surface cleanliness.

1.2.3.3 Band Gap Validation

Further characterisation by Scanning Tunnelling Spectroscopy (STS) measurement was performed on the sample surface at room temperature and is shown in Fig. 1.13. The STS is a useful tool for the provision of information about the density of electrons in a sample as a function of their energy. An important advantage of the STM is the possibility of recording local spectroscopies. To achieve this, the height z of the tip is fixed and the tunnelling current is measured as a function of the bias voltage. The regulation loop is opened in order to keep the distance z constant and a voltage ramp is applied.

At a given voltage, the tunnelling current is proportional to the density of state of the tip and the local density of state of the sample near the Fermi level. However, the state density of the tip varies very little as a function of the applied voltage [97]. The expression for the current is given as:

$$I \propto \int_0^{eV} n_s(E, \overrightarrow{r_0}).T(E, V, d).dE \tag{1.1}$$

where $n_s(E, \overrightarrow{r_0})$ is the density of states at the Fermi level for the surface, d the tip-surface distance, *T(E,V,d)* is the transmission coefficient of the tunnel barrier for an electron with energy E. This depends on the nature of the barrier and includes the exponential of the current versus distance *d*.

The derivative of equation 1.1 with respect to the bias voltage provides access to the conductance, which is given as:

$$\frac{dI}{dV} = n_s(E, \overrightarrow{r_0}).T((E_F - eV), d) \tag{1.2}$$

The conductance is therefore proportional to the local density of state of the surface, $n_s(E, \overrightarrow{r_0})$ near the Fermi level.

The dI/dV curve is shown in Fig. 1.13 by averaging 4 *I-V* curves per point before taking the derivative numerically, a method typically used in the literature to determine the band gap of TMDCs [98]. The measurement was taken far from the edge to avoid perturbation or confinement effect which could be caused by defects around the edge. Using this approach, we were able to determine the band edges as where the dI/dV signal becomes distinct from the background noise levels. From the curve, the valence band maximum (VBM) is observed around -1.65 eV and the

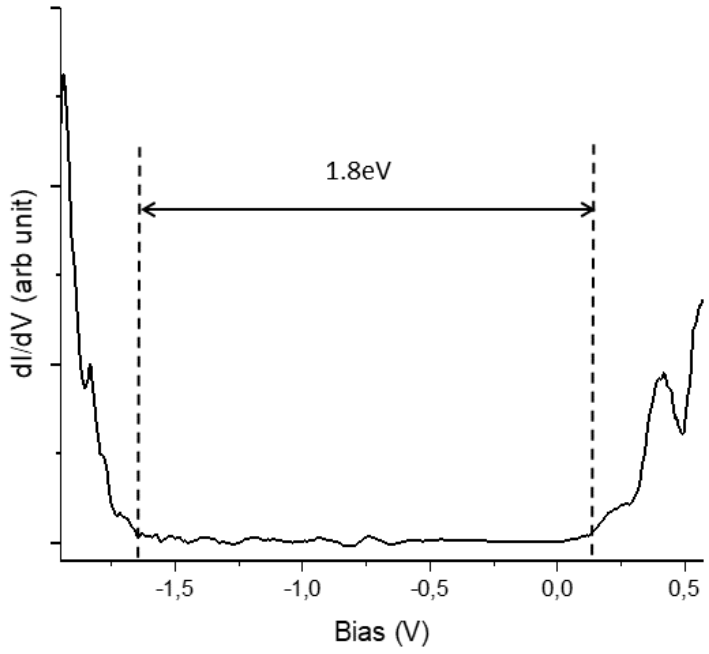

Figure 1.13: STS spectrum of the transferred film with a band gap of 1.8 eV.

conduction band minimum (CBM) around 0.15 eV. This gives a band gap of about 1.8 eV which corresponds to the value of the direct band gap of single-layer MoS_2 [99, 100]. This indicates that the state density of the transferred MoS_2 film is kept intact. It goes further to prove the efficacy of our optimised transfer technique.

1.2.3.4 Raman Characterisation

The sample was withdrawn from the nanoplast device and taken for Raman spectroscopy characterisation. Raman spectra of the sample were measured at the IC2MP research institute of the University of Poitiers using a *Raman Labram HR 800 confocal microscope* with a 532 nm wavelength laser.

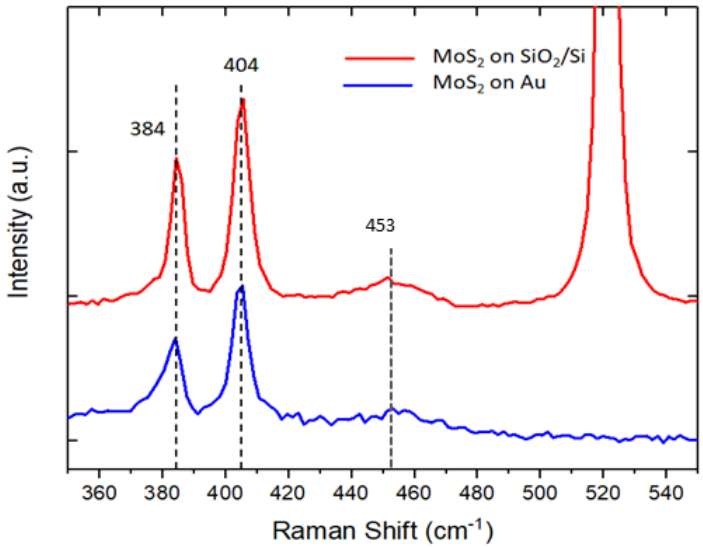

Figure 1.14: Raman spectra of monolayer MoS_2 film on its growth substrate (SiO_2/Si) and transferred MoS_2 film on Au.

Raman characterisations in Fig. 1.14 show the spectrum of MoS_2 on SiO_2/Si (growth substrate) represented by red line and the spectrum of MoS_2 transferred to Au substrate represented by blue line. Each spectrum shows two main peaks and a weak peak in the spectrum which correspond to Raman mode of E^1_{2g}, A_{1g} and E_{1g} respectively. The Raman spectrum of the transferred sample exhibits two typical peaks with in-plane vibration of Mo and S atoms (E^1_{2g}) at 384 cm^{-1} and the out-of-plane vibration of S atoms (A_{1g}) at 404 cm^{-1}. A weak E_{1g} peak is observed at 453 cm^{-1}. The peaks correspond to the Raman spectra of the pristine monolayer MoS_2 on

the SiO_2/Si growth substrate. The presence of the E^1_{2g} peak indicates that the film maintains a trigonal prismatic co-ordination as compared to MoS_2 monolayer prepared from Li-intercalation which do not show the E^1_{2g} peak due to the presence of metastable octahedral co-ordination that causes the Raman vibration inactive [101]. The major peaks (E^1_{2g} and A_{1g}) on both samples show a frequency difference of 20 cm^{-1} which shows the preservation of the film thickness after transfer and corresponds to that of a monolayer of MoS_2 film. In case of a bi-layer, the frequency difference of the E^1_{2g} and A_{1g} peaks is expected to increase by about 3 cm^{-1} compared to the monolayer and keeps increasing by the same value as the number of layer increases [102]. The Raman spectrum confirms the preservation of the morphology, quality and thickness of the transferred MoS_2 film.

1.2.3.5 MoS_2 on PEEK Substrate

To confirm its versatility, we transferred MoS_2 film from sapphire to an already prepared PEEK substrate using the direct transfer technique. The prepared sample could not be characterised using the STM technique due to the non-conductive nature of the substrate. Therefore, the sample was characterised using the already discussed Bruker's Dimension Icon AFM. After transfer, the sample underwent no further drying or surface cleaning process.

A scan of the sample surface, as shown in Fig. 1.15a, shows that MoS_2 was indeed transferred to the PEEK surface. The film thickness was measured via a crack across a 5×5 μm^2 area of the sample surface. A line profile across the crack shows a depth of 1.5 nm (Fig. 1.15b). This gives an estimate of the film thickness; however, there is a possibility of the presence of water molecules at the sample surface and at the MoS_2-PEEK interface since there was no heat treatment to expel water from the sample to preserve the sample from oxidation. As already established in the literature, water molecules are absorbed from the atmosphere and can contribute to the overall thickness of the film if heat treatment is not carried out [103]. Additionally, pockets of water are most likely trapped at the PEEK-MoS_2 interface due to the surface roughness of PEEK substrate.

The direct transfer technique was put to the test for the transfer of multi-layer MoS_2 film. To do this, three layers of MoS_2 film (represented as 3L MoS_2 henceforth) grown on sapphire substrate by CVD technique and purchased from *Six Carbon Technology* was transferred to a

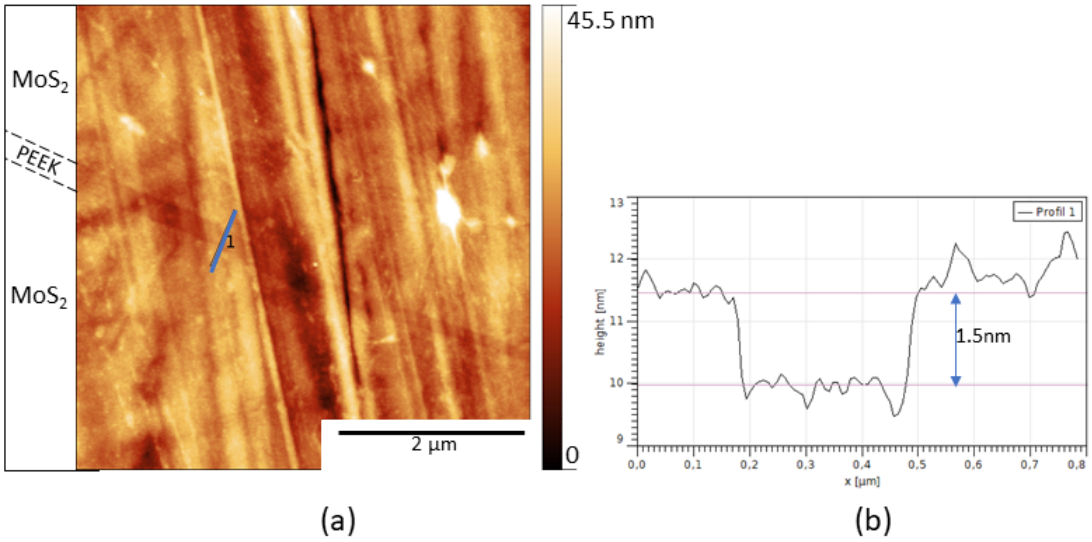

Figure 1.15: (a) AFM image of transferred MoS_2 monolayer to PEEK (Peak Force Tapping Mode, RT) (b) Profile indicating the thickness of the transferred film.

PEEK substrate to test the procedure on a new substrate. This was done without any modification to the transfer protocol. The sample was characterised before and after transfer using the AFM technique, as shown in Fig. 1.16, specifically to measure the film thickness. A variation in film thickness would suggest the possibility of incomplete film transfer.

The thickness of 3L MoS_2 on its growth substrate (Fig. 1.16a), measured by a line profile across the film-substrate boundary, is given as 6 nm, a value higher than an expected thickness (less than 3 nm). The high value measured could be due to a small lift-off of the film during debonding from the substrate. Also, since the film is a continuous film, an area with defect was scanned to measure the film thickness. Alternatively, it is possible that the measured value is the true thickness of the film as we did not independently verify the number of MoS_2 layers present in the film as purchased since the number of layers is not of paramount concern, but the thickness. After transfer, a thickness of about 8 nm is measured from the film-PEEK boundary (Fig. 1.16b). Although the measured thickness after transfer is slightly higher than the measured thickness of the film on the growth substrate, the presence of water at the film-PEEK interface can not be ruled out since characterisation was done in ambient condition and without heat treatment.

The results discussed in this section prove the efficacy of our technique to transfer monolayer MoS_2 from the growth substrate to both metallic and non-metallic substrates. The technique, which is quick and easy to use, ensures the preservation of the morphology of the transferred

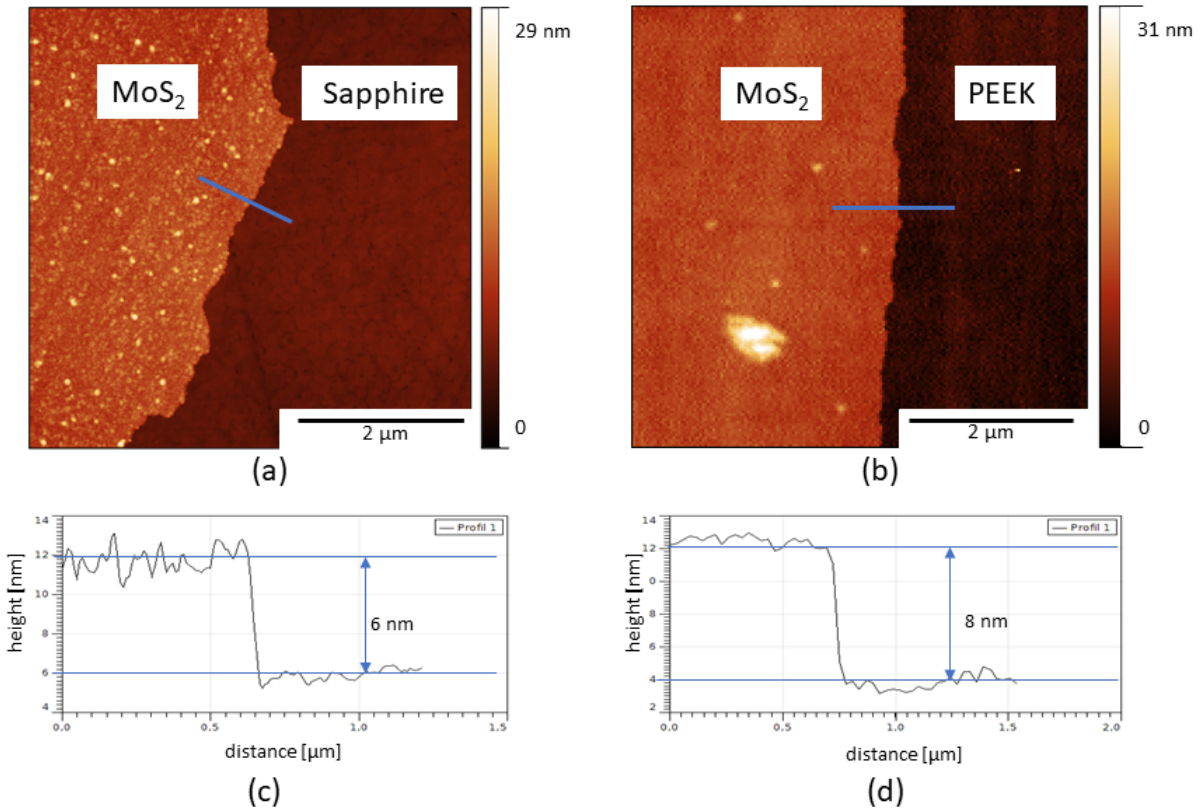

Figure 1.16: AFM images of 3L MoS_2: (a) 3L MoS_2 on sapphire (growth substrate), (b) 3L MoS_2 transferred to PEEK using direct transfer technique (PFT mode, RT)

film. When compared to other reported techniques, our technique gives a clean surface, devoid of external contamination or impurities from additional coatings.

1.3 Summary

This chapter discusses the experimental techniques and devices used for characterisation of samples used for this study. In section 1.1, STM and AFM techniques were briefly discussed with descriptions of the devices used for these characterisations - Nanoplast device and Bruker's Dimension Icon AFM device. Other sections of this chapter are dedicated to experimental details of sample preparation for this study.

We considered different reported techniques for the transfer of 2D films from growth substrate to another substrate of interest. To achieve a good result, we started with the preparation of the surfaces of target substrate. In section 1.2.1, we discussed preparation procedures for

substrate surfaces. These procedures include several cycles of polishing and Ar ion sputtering of the substrate. We highlighted procedures to achieve clean and flat surfaces for metallic and non-metallic substrates; specifically Cu and PEEK substrates.

In section 1.2.2, we discussed an existing technique used for the transfer of 2D materials including MoS_2 films. This technique employs the use of PMMA which serves as a support/sacrificial layer for the film during transfer. The coating is then cleaned after the transfer process is completed. Experimental results by AFM and AES indicate the presence of PMMA residue at the sample surface despite several cleaning.

Finally, in section 1.2.3, we proposed an optimised procedure for the transfer of MoS_2 films in order to eliminate surface contamination from PMMA residue. Using the proposed technique, MoS_2 films of different thicknesses were transferred to metallic and non-metallic substrates. Results of sample characterisation by STM, STS, Raman spectroscopy and AFM all indicate that MoS_2 film was indeed transferred with its morphology preserved. AFM characterisation of transferred 3L MoS_2 shows that all layers of the film were transferred by comparing the thickness of the film before and after transfer.

1.4 Résumé en Français

La compréhension des propriétés des matériaux ultra-fins ouvre un large éventail de possibilités dans les applications qui impliquent notamment l'utilisation d'électronique flexible et de nanodispositifs. Le disulfure de molybdène MoS_2, membre des dichalcogénures de métaux de transition (TMDC), a été largement étudié en raison de ses impressionnantes propriétés optiques et électroniques. Plusieurs analyses numériques ont permis de prédire que le MoS_2 possède également des propriétés mécaniques exceptionnelles, bien qu'il n'existe que peu de rapports expérimentaux à l'appui de cette affirmation. La difficulté de transférer des couches simples ou peu nombreuses de films de MoS_2 de leurs substrats de croissance à d'autres substrats d'intérêt rend difficile l'exploration expérimentale du matériau. L'objectif de cette thèse est donc d'étudier expérimentalement le comportement mécanique de films de MoS_2 ultra-minces sur des substrats sous contraintes et d'exploiter la validité des modèles numériques existant pour les films minces pour ces matériaux de dimension ultime.

Le premier chapitre de ce travail se concentre sur les procédures expérimentales et l'équipement utilisé dans le cadre de cette recherche.

I. Equipement

Ce travail de thèse s'est appuyé principalement sur des techniques de caractérisation de surface et de la microscopie champ proche, en particulier la microscopie à force atomique (AFM). L'AFM permet d'imager la topographie de la surface d'un échantillon en mesurant la force d'interaction entre les atomes de la sonde et les atomes de la surface balayée. Il existe de nombreux modes de balayage AFM et, dans le cadre de cette thèse, le mode Peak Force Tapping (PFT) a été utilisé. Le mode PFT fonctionne en utilisant un levier AFM spécialisé oscillant de manière contrôlée, tout en maintenant une force constante entre la pointe et la surface de l'échantillon par une boucle de rétroaction. Ce mode permet d'obtenir rapidement une image à haute résolution de la surface de l'échantillon.

II. Transfert des films de MoS_2 sur substrats d'intérêt

Les films de MoS_2, comme d'autres films 2D, sont crûs sur peu de substrats. Il est donc régulièrement nécessaire de les transférer de leur substrat de croissance vers d'autres substrats d'intérêt. Les échantillons utilisés dans cette étude consistent en des films de MoS_2 crûs par CVD sur des substrats de SiO_2/Si et de saphir, puis transférés sur substrats métalliques et non métalliques. L'utilisation de substrats métalliques a permis la validation de l'intégrité des films des films de MoS_2 transférés. Les substrats non métalliques ont quant à eux été utilisés pour les études mécaniques.

1) Préparation des substrats

Avant de transférer un film de MoS_2, il est nécessaire de préparer le substrat d'intérêt. Deux modes de préparations ont été utilisé.

Substrats métalliques: La préparation s'est concentrée sur des monocristaux de cuivre et d'or. Ils ont tout d'abord subi plusieurs cycles de polissage impliquant une réduction progressive de la suspension de diamant monocristallin. Les substrats ont ensuite été introduits sous UHV où ils ont été soumis à une succession de bombardements ioniques et recuits avant d'être contrôlés par microscopie champ proche.

Substrats polymères: Le polyéther-éther-cétone (PEEK), un polymère semi-cristallin, a été plébiscité comme substrat non métallique pour étudier le comportement mécanique des films de MoS_2. Les procédés de préparation de surface décrits dans la littérature étant limités, nous avons conçu un protocole qui implique l'utilisation de différents tissus de polissage et de suspensions diamantées de différentes tailles de grain afin de réduire autant que possible la rugosité de la surface. La topographie de la surface de PEEK préparée a été imagée par l'AFM et montre des terrasses plates avec une rugosité de surface moyenne de 4 à 5 nm, ce qui valide la méthode de polissage.

2) Transfert en utilisant une couche de support

Les films continus monocouches de MoS_2, crûs sur saphir, ont été transférés sur une surface de Cu(100) à l'aide d'une méthode régulièrement utilisée dans la littérature. Cette méthode a consisté déposer par spin-coating la surface du film d'une solution de poly méthacrylate de méthyle (PMMA), un polymère qui sert de couche de support au film de MoS_2. L'empilement PMMA/MoS_2/saphir durci a été traité par ultrasons dans de l'eau distillée afin d'introduire de minuscules bulles à l'interface MoS_2 – saphir et entraîner la délamination du film du saphir. L'empilement PMMA/MoS_2, flottant sur l'eau désionisée, a été "repêché" via le substrat Cu déjà préparé. Pour garantir l'élimination complète du PMMA de la surface du MoS_2, l'échantillon a été nettoyé dans 3 bains d'acétone à 80°C, un bain d'éthanol et un bain d'isopropanol, puis séché. La caractérisation de la surface par AFM illustrée par les Fig. 1.17a et b indique que l'épaisseur du film de MoS_2 transféré par PMMA a une épaisseur d'environ 6,7 nm par rapport à une épaisseur de film de 0,77 nm avant le transfert. Cela suggère la présence de résidus de PMMA à la surface de l'échantillon. Un examen plus approfondi par spectroscopie d'énergie Auger (AES), illustré à la Fig. 1.17c, indique la présence d'atomes de carbone et d'oxygène en quantités relativement importantes sur la surface de l'échantillon, ce qui confirme la présence de résidus de PMMA sur la surface libre.

3) Mise en place d'une nouvelle méthode de transfert

En raison des inconvénients de la technique de transfert assistée par PMMA, nous avons mis au point une technique qui garantit dans une large mesure une surface propre et exempte d'impuretés en éliminant l'utilisation d'un revêtement de support. Pour ce faire, nous avons éliminé l'utilisation de PMMA et placé le substrat ciblé en contact avec le film, puis nous avons fixé fermement le tout à une palette en acier avant l'ultrasonication. Le procédé est schématisé Fig. 1.18. Le transfert du film est favorisé par l'hydrophilie plus élevée du substrat de croissance par rapport au film et au substrat d'interêt. Ainsi, comme avec la méthode précédente, l'ultrasonication génère des microbulles d'eau qui entraînent le décollement du film de son substrat de croissance. La présence de l'eau force ensuite le film à adhérer à la surface du substrat ciblé. L'analyse STM sous UHV d'une monocouche de MoS_2 transférée sur Au(111) révèle une épaisseur de film transférée de

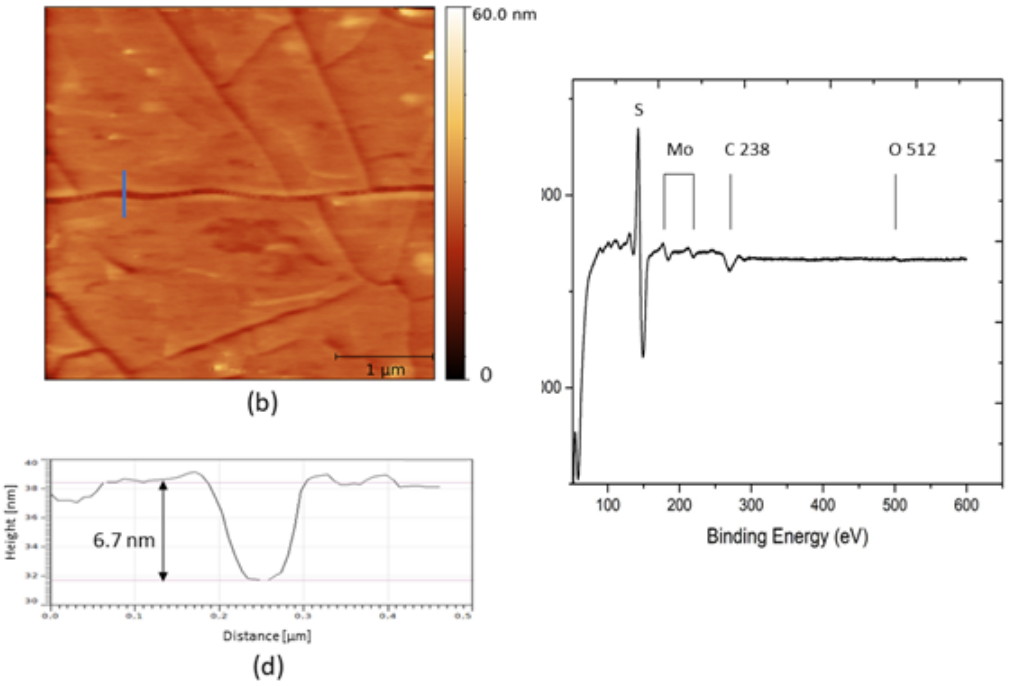

Figure 1.17: (a) AFM image sous UHV d'une monocouche de MoS_2 après transfert sur Cu(100) utilisant une couche de PMMA. (Non-contact, f = -10 Hz, gain = 127%, RT), (b) Profil à travers une cassure le long de la ligne bleue tracée en (a), (c) AES à basse énergie d'un film de MoS_2 transféré montrant les pics de carbone et d'oxygène majoritairement liés à la présence résiduelle de PMMA sur la surface de l'échantillon.

0,76 nm. La spectroscopie à effet tunnel à température ambiante a permis de déterminer que la bande interdite du film transféré était d'environ 1,8 eV. Les pics des spectres Raman de la monocouche transférée confirment la préservation de la morphologie et de l'état vierge du film.

Afin de confirmer la validation de la technique de transfert optimisée, un film de MoS_2 une monocouche (1L) a été transféré sur un substrat polymère. L'analyse AFM de l'échantillon montre que le film a bien été transféré et qu'il présente une épaisseur d'environ 1,5 nm. Cette épaisseur est supérieure à l'épaisseur du film original avant le transfert. Cependant, nous notons qu'aucun traitement thermique n'ayant été effectué sur l'échantillon après le transfert, la présence de molécules d'eau pourrait contribuer à l'épaisseur globale du film. De même, un film de MoS_2 à trois couches (3L) a été transféré de son substrat de croissance vers un substrat polymère. L'épaisseur du film avant et après le transfert a été mesurée à 6 nm et 8 nm respectivement (Fig. 1.19). La différence d'épaisseur pourrait également être liée à la présence de molécules d'eau comme dans le cas d'une monocouche.

En conclusion, les résultats présentés dans ce chapitre prouvent l'efficacité de notre technique

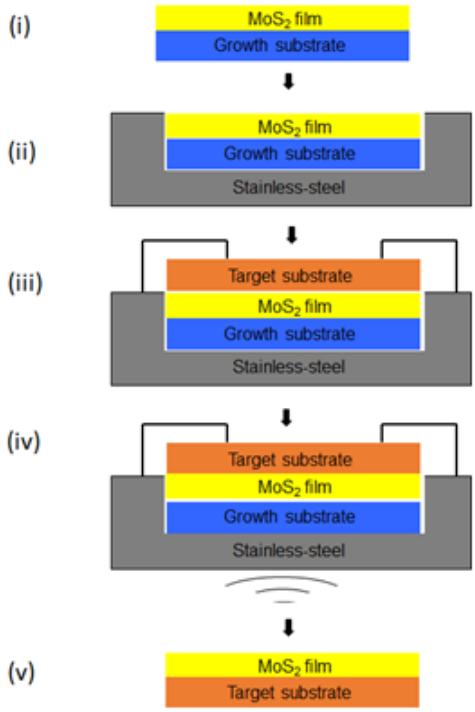

Figure 1.18: Illustration du transfert direct. (i) Film de MoS_2 sur son substrat de croissance, (ii) Insertion dans l'encoche d'un bloc en acier, (iii) Placement et fixation du substrat cible sur le film, (iv) Ultrasonication, (v) MoS_2 transféré sur substrat cible.

pour transférer un film 2D de MoS_2 du substrat de croissance sur divers substrats d'intérêt. La technique, qui est rapide et facile à utiliser, garantit la préservation de la morphologie du film transféré. Comparée à d'autres techniques rapportées, notre technique permet d'obtenir une surface propre, dépourvue de contamination externe ou d'impuretés provenant de revêtements supplémentaires.

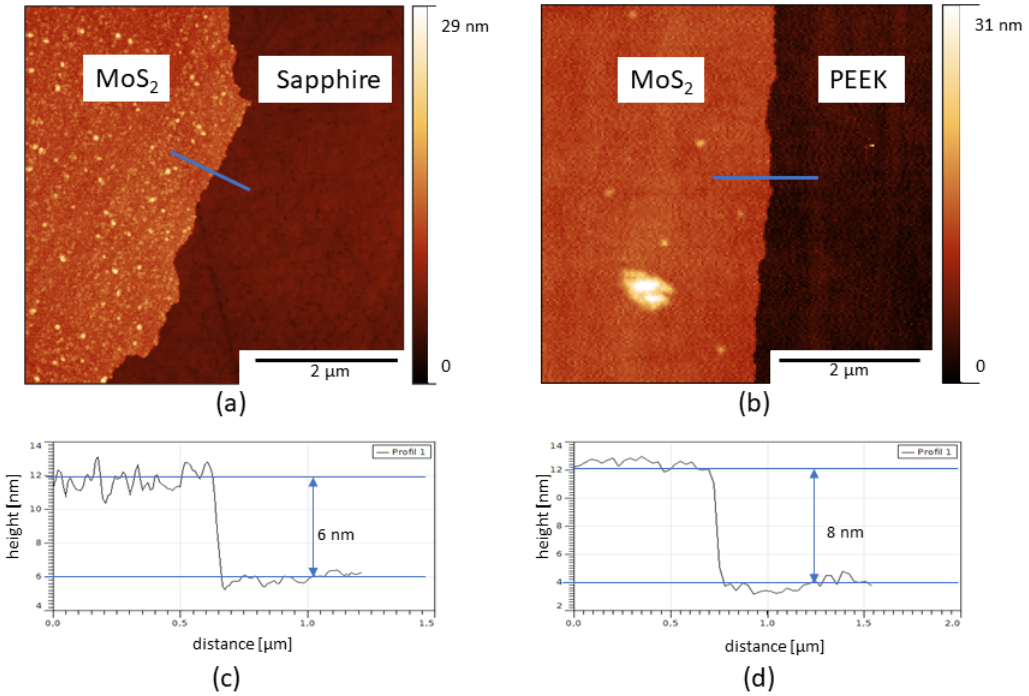

Figure 1.19: Images AFM du MoS_2 3L : (a) MoS_2 3L sur saphir (substrat de croissance), (b) MoS_2 3L transféré sur PEEK à l'aide de la technique de transfert direct.

Chapter 2

Buckling of MoS_2 films: a descriptive study

Contents

2.1 Experimental Procedure and Characterisation 44
2.1.1 Substrate Characterisation under Compressive Stress 44
2.1.2 Experimental Device and Protocol 45
2.2 AFM Results 47
2.2.1 Emergence of Straight-Sided Buckles 47
2.2.2 Strain-Induced Cracks on Film 49
2.2.3 Interactions Between Buckles 52
2.2.4 *In-situ* Cyclic Compression 61
2.3 Summary 62
2.4 Résumé en Français 64

Objective

The mechanical behaviour of metallic films under compression have been extensively studied in the past by means of experiments and simulations. In many cases, especially in the case of uni-

axial compression, straight-sided buckles (SSBs) have been observed to propagate with increasing stress and in a direction perpendicular to the compression axis [104]. Interactions between two SSBs propagating in opposite directions were also reported [105], and found to be dependent on the distance between them and linked to the mechanical properties of the film/substrate system. It is therefore our interest to investigate by experiments and to further compare the mechanical behaviour of ultrathin MoS_2 to what has been observed in thick metallic films.

After the successful film transfer described in Chapter 1, the interest of this Chapter is to observe the response of 2D MoS_2 films on PEEK substrates to compressive strains. This Chapter is divided into two sections. The first section discusses the mechanical test procedure of the samples including the mechanical behaviour of PEEK substrates under compression. The second section discusses experimental observations of the response of the MoS_2 film to compressive stresses in particular in the scope of SSBs interactions observed in thick metallic plates and reported in the literature.

2.1 Experimental Procedure and Characterisation

2.1.1 Substrate Characterisation under Compressive Stress

PEEK is chosen as the substrate for this study due to some of its interesting physical and mechanical properties. Unlike many other polymers, water does not play a significant role in its elasticity. Therefore, its performance is not affected by the film transfer procedure which was performed in water. It is a semi-crystalline material with a large elastic range and a high Young's modulus for a polymer (E_s = 4.0 GPa), which gives it good rigidity by reducing the risk of bending during compression.

Compression tests were carried out on a PEEK 450G substrate to determine its performance and how it can influence the response of the transferred film. The substrate was deformed uniaxially by cyclic compressive strains at room temperature using a Deben microtest device (5 kN dual leadscrew stage with 1526:1 gearbox and 512-line encoder, calibrated at 5070 N), which allows both stress and/or strain readings to be taken during loading (compression) and unloading (relaxation) at a constant rate of 10^{-3} s^{-1}. The stress-strain curve of four cycles of loading and

unloading is presented in Fig. 2.1. It should be noted that the stress-strain values recorded are engineering values (nominal values) and not true values. However, since the elastic region of the substrate is not exceeded, the difference between the engineering and true values are infinitesimally small and therefore can be negligible. The sample was deformed to a strain value of 6% and completely unloaded for every cycle before reloading for the next cycle.

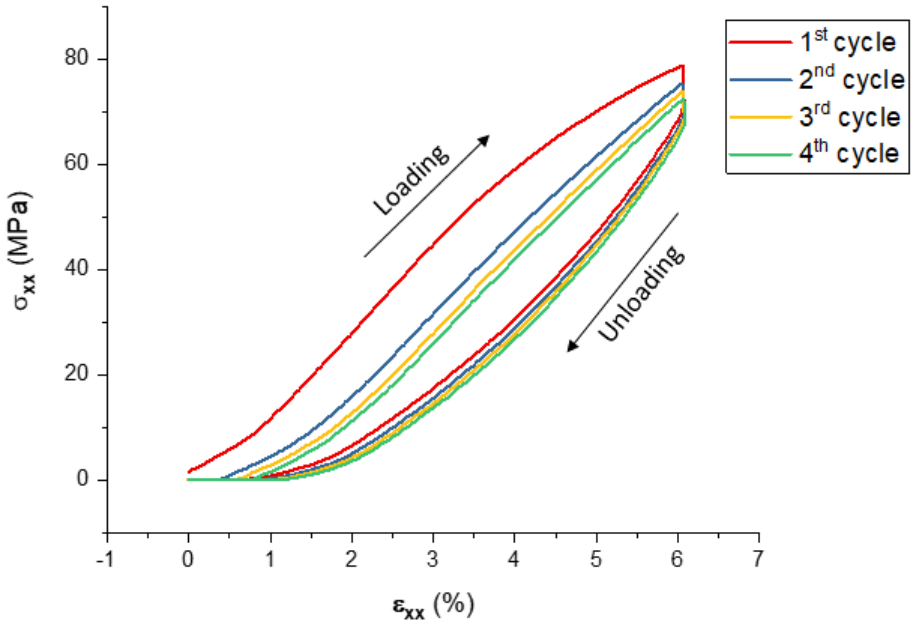

Figure 2.1: Stress-strain curve of PEEK substrate ($2\ mm \times 2\ mm \times 6\ mm$) over 4 cycles. Compression rate: $10^{-3}\ s^{-1}$.

The stress-strain curve in Fig. 2.1 reveals that PEEK exhibits an elastic hysteresis, typical of viscoelastic materials [106]. This indicates an energy loss during each loading and unloading cycle. After the first cycle, other cycles appear to have similar hysteresis. Up to 6% strain, PEEK remains in its elastic regime; therefore, strain is almost totally recoverable for all the cycles. Hence, it is expected that PEEK substrate can be compressed up to 6% strain for several cycles with little or no alteration of its mechanical properties.

2.1.2 Experimental Device and Protocol

To induce stress on the prepared samples, a manual micro-compression device (shown in Fig. 2.2) was designed by Bruno Lamongie (from P' Institute) and home-fabricated. It was necessary to design a small compression device that would fit into the AFM compartment and allow *in-situ*

compression and imaging. The compression device allows the samples to be deformed by uniaxial compression of the substrate so as to trigger a response from the film. The deformation, which can be incremental, is then observed by AFM.

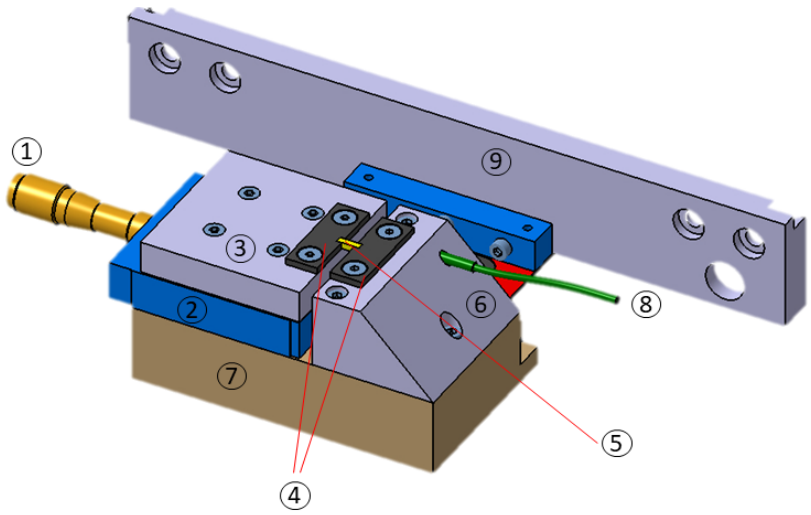

Figure 2.2: 3D view of the manual micro-compression device for sample compression. (1) Ratchet attached to the thimble, (2) Moveable rectangular frame controlled by the ratchet, (3) Stainless steel block screwed to the moveable frame, (4) Jaws to accommodate the sample, (5) Sample, (6) Fixed stainless steel block, (7) Ceramic base, (8) Optical fiber to measure the displacement of the jaw, (9) Brace to AFM.

The device is mostly fabricated from stainless steel material. There are two blocks on which flat jaws are firmly attached. The jaws provide secure accommodation for samples to be compressed. One of the blocks is placed above a modified micrometer screw gauge and held firmly with screws while the other block is fixed to the base of the device. Turning the ratchet knob of the micrometer screw gauge causes the block above it to move in the horizontal direction, consequently causing the jaw screwed to it to open or close. The distance travelled by the jaw, which corresponds to the displacement imposed on the sample, can be measured directly from the scales on the sleeve of the micrometer screw gauge. Another way of measurement is to use a vernier calliper which is more convenient. A brace attached to the compression device is screwed to the side of the computer-controlled sample stage of the AFM device (as earlier shown in Fig. 1.2). This allows the sample to be placed under the AFM scanner and also be moved in any direction of interest by controlling the movement of the sample stage. Therefore, it makes it possible to follow precisely any area of interest on the sample surface. The sample is inserted between the jaws of the micro-compression device and strained along the x-axis, as shown in Fig. 2.3, by turning the

device ratchet. When the sample is compressed, the strain in the system remains intact through the help of a spring system which minimises relaxation. This allows the sample to be scanned for several hours without "losing" the film morphology to substrate relaxation.

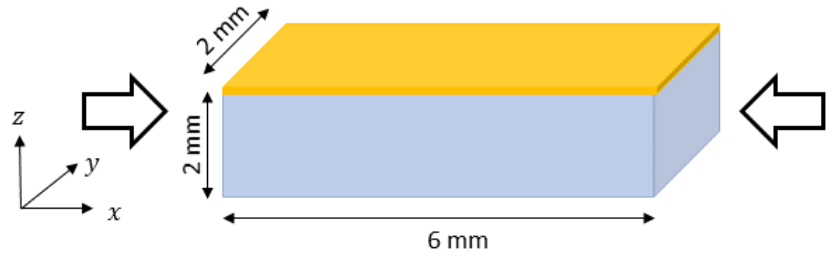

Figure 2.3: Representation of the sample (MoS_2 film on PEEK) showing the compression direction represented by arrows along the x-axis.

2.2 AFM Results

This section is dedicated to a comprehensive description of observations from the AFM. The results will be further analysed in Chapter 3. Both single and three layer MoS_2 (labelled 1L MoS_2 and 3L MoS_2 in the following) films on PEEK substrates were subjected to a gradual compressive strain. Specific areas on the samples were scanned after every strain step of about 1% (huge step is taken in order to minimise error since the straining device is manually controlled) to observe the surface evolution of each sample under increasing strain. Fig. 2.4 shows the AFM images of specific regions of the sample surfaces. The scanned areas are not perfectly flat due to residual scratches on the PEEK substrates from polishing (as already discussed in the first chapter). The residual scratches are shown by blue arrows in Fig. 2.4a and d. MoS_2 film cracks are also observed on the scanned surface of 1L MoS_2 and shown by extended broken lines in Fig. 2.4a-c. These defects serve as markers to locate areas of interest.

2.2.1 Emergence of Straight-Sided Buckles

The AFM images of 1L MoS_2 are shown in Fig. 2.4a, b and c to represent the topography of the film at compressive substrate strain $\varepsilon_s = 1\%$, 2% and 3%, respectively. Likewise, Fig. 2.4d, e and f represent the topography of 3L MoS_2 at $\varepsilon_s = 1\%$, 2% and 3%, respectively. No difference was observed on both samples from $\varepsilon_s = 1\%$ to 3%. At $\varepsilon_s = 4\%$, several straight-sided buckles

(SSBs) of the MoS_2 films were observed on both 1L and 3L MoS_2 surfaces (shown by black arrows in Fig. 2.4c and f). These straight-sided buckles appear to propagate along the y-axis, which is perpendicular to the compression axis (horizontal direction) just as it has been observed and reported in the literature for uniaxially compressed metallic films [107–109]. The morphology of out-of-plane displacement of these buckles is measured by taking a profile across the buckle which helps in determining the deflection (height) δ and the width $2b$ of the buckle. They will be the key elements to investigate whether the Föppl-von Kármán thin plate model, which has been used over the years to effectively model the elastic behaviour of plates under stress/strain, can be extended to 2D materials.

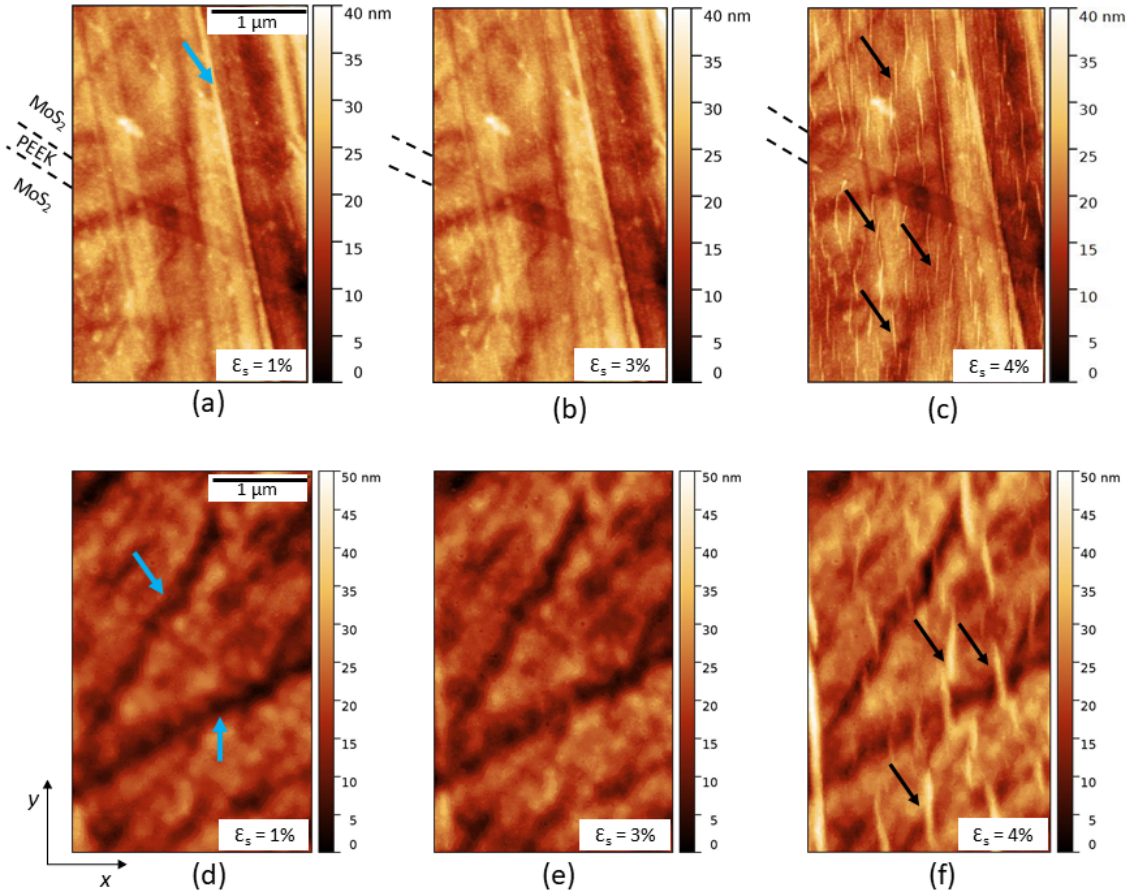

Figure 2.4: Observation by AFM of 1L MoS_2 on PEEK during compression strain ε_s = (a) 1%, (b) 3%, (c) 4%, and 3L MoS_2 on PEEK at ε_s = (d) 1% (e) 3%, (f) 4%. Blue arrows point at residual scratches on the PEEK surface and black arrows point at the SSBs. (PFT mode, RT).

Fig. 2.5 shows the superposition of the buckle profiles obtained for both 1L MoS_2 with thickness $h = 1$ nm and 3L MoS_2 with thickness $h = 6$ nm. Note that, just as in the case of 1L

MoS_2, buckles were first observed at $\varepsilon_s = 4\%$ for 3L MoS_2. This implies that the experimental critical buckling strain of both samples lies between 3% strain on substrate (when no buckle was observed) and 4% (when buckles were first observed) *i.e.* $3\% < \varepsilon_s^* < 4\%$ substrate strain.

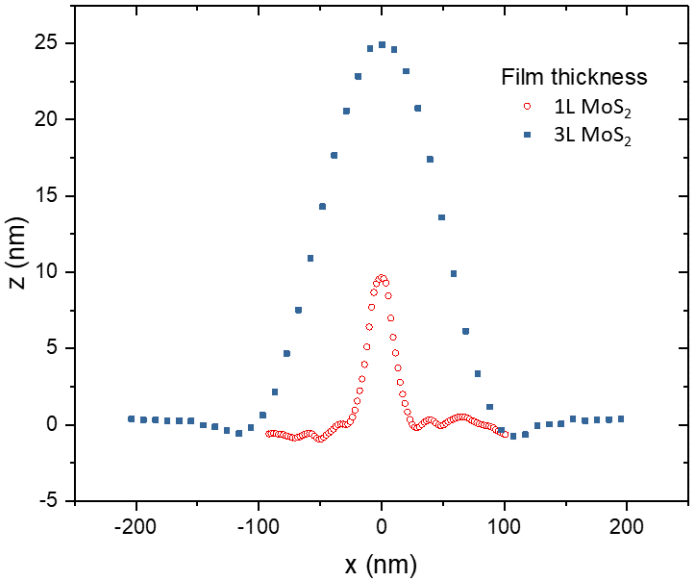

Figure 2.5: AFM profiles of the buckling structures obtained for two thicknesses of MoS_2/PEEK deformed at 4% applied strain on substrate.

Under the same strain condition, the buckle structure of the 1L MoS_2 film has a deflection δ and width $2b$ of 10 nm and 42 nm respectively, as compared to the buckle of the 3L MoS_2 film which has a deflection and width of 25 nm and 180 nm respectively. When h is increased, δ and $2b$ are increased. As the elastic energy stored in the film is consequently increased, the delamination at the interface $2b$ is increased, the deflection δ as a result. In both cases, $h/b \ll 1$ (0.067 and 0.048, respectively), satisfying the condition for the validity of the Euler's theory, further described in Chapter 3. This also indicates that the mechanical behaviour of the films can be further analysed under the frame-work of Föppl-von Kármán theory of thin plates.

2.2.2 Strain-Induced Cracks on Film

As compressive strain is increased, the buckles were observed to grow in size (up to 50% and 80% increase in δ of 1L and 3L MoS_2 buckles respectively). Also, as compressive strain increased, cracks were induced on the film surface. Images in Fig. 2.6 show a region of 5×5 μm^2 of 1L MoS_2/PEEK with increased strain corresponding to $\varepsilon_s = 4\%$, to 6%. A wide crack induced

during the transfer is seen on the sample surface (indicated by the broken extension lines) and it is consistent in all the images. In Fig. 2.6b, at $\varepsilon_s = 5\%$, a first crack (indicated by a red arrow) appears and propagates approximately along the horizontal direction. The crack cuts through several buckles on its path. Increasing ε_s to 6% shown in Fig. 2.6c, an increase in the width of the crack is observed (from about $l = 49$ nm at $\varepsilon_s = 5\%$ to $l = 78$ nm at $\varepsilon_s = 6\%$). This change in the width suggests a movement of the film over the substrate. Also, a new crack can be seen propagating in the upper half of the image. We therefore stopped the compression at $\varepsilon_s = 6\%$ in order not to induce too many cracks on the film and to remain in the elastic region of the substrate.

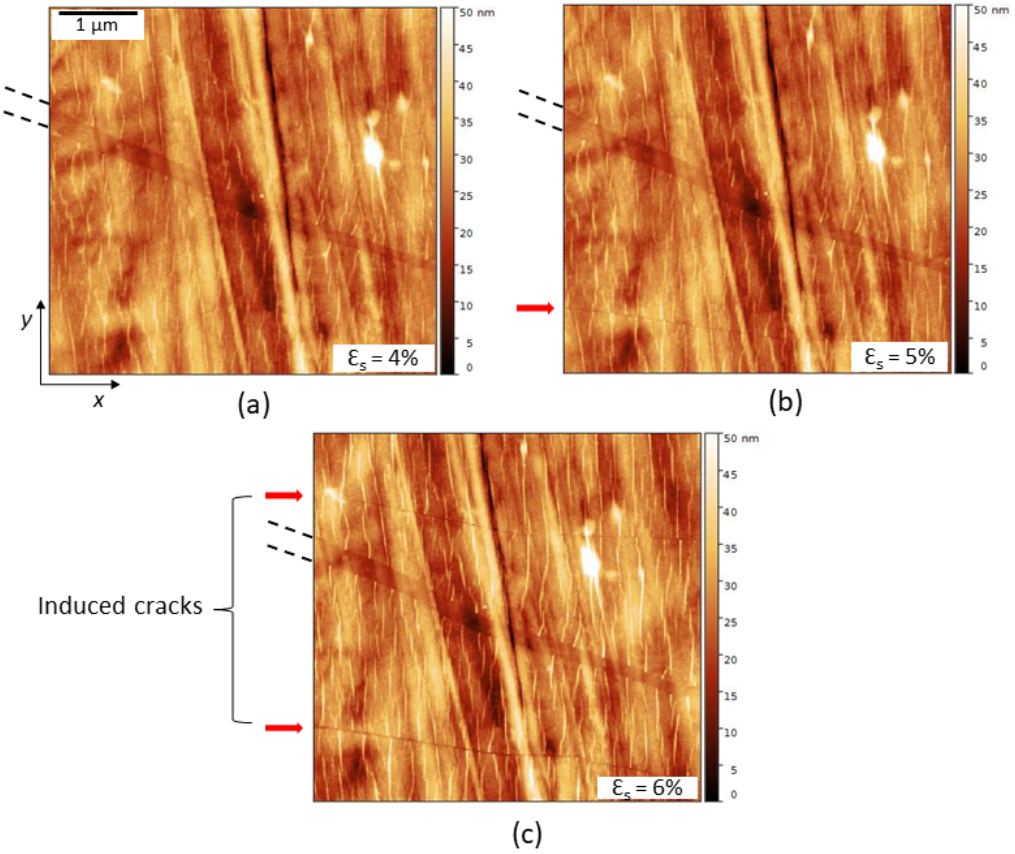

Figure 2.6: Cracks induced by imposed strain on 1L MoS_2 (h = 1 nm)/PEEK with increasing substrate strain (a) $\varepsilon_s = 4\%$ (b) $\varepsilon_s = 5\%$ (c) $\varepsilon_s = 6\%$.

A similar observation was made in the case of 3L MoS_2/PEEK, as shown in Fig. 2.7a, b and c corresponding to the sample under compression at $\varepsilon_s = 4\%$, 5% and 6%, respectively. Similar to what was observed in 1L MoS_2/PEEK, a crack was observed as strain increased to 6% (Fig. 2.7c)

which also propagates in the horizontal direction, approximately parallel to the compression axis. The crack also cuts through the buckles on its path and abruptly terminates the propagation of several buckles. Also observed is the disappearance of small buckles close to the crack. Examples of these small buckles are shown by the two white arrows in Fig. 2.7b. These two buckles are no longer observable after the crack emerges in Fig. 2.7c. It is therefore believed that the crack locally relaxes the stress in the film. Another possibility is that the excess film in those small buckles slides on the substrate and moves towards other buckles causing them to increase in size as a result.

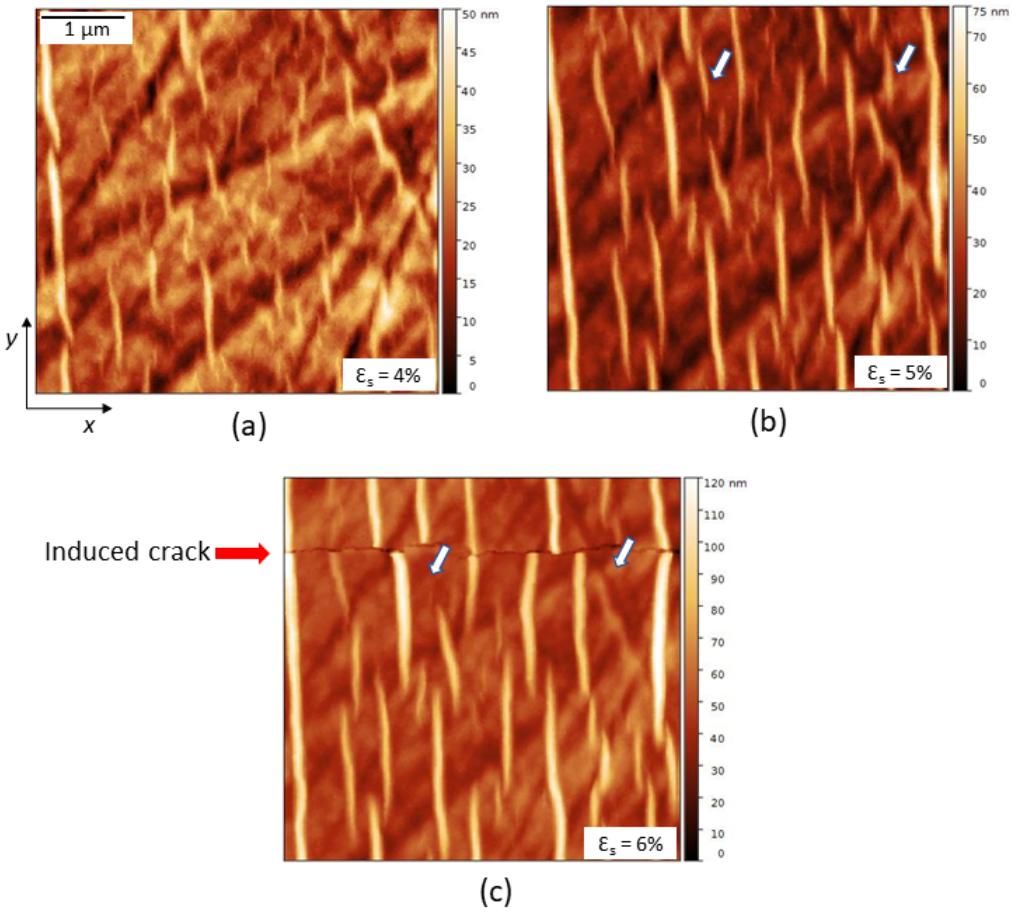

Figure 2.7: Crack induced by strain on 3L MoS_2/PEEK (h = 6 nm) with increasing strain with an resulting relaxation of smaller buckles close to the emerging crack (a) $\varepsilon_s = 4\%$ (b) $\varepsilon_s = 5\%$ (c) $\varepsilon_s = 6\%$. White arrows in (b) show smaller SSBs which have been relaxed by induced crack in (c).

In all cases, the strain-induced cracks propagate parallel to the compression direction. This is due to the Poisson effect, as deformation caused by applied strain along the x-axis results in the film being stretched (in tension) along the perpendicular direction (y-axis). As substrate

compression increases, the film reaches a breaking point and crack is initiated.

2.2.3 Interactions Between Buckles

Interactions between SSBs of Ni thin films (100 nm and 200 nm thickness) on polycarbonate (PC) substrates, propagating in opposite directions, were recently observed by AFM and studied by finite element simulations (FEM) [105]. Results shown in Fig. 2.8 reveal that depending on the distance d between them, two SSBs propagating in opposite directions can be attracted to each other with their fronts slightly deviated from their initial propagation direction and wrapped around each other (2.8b) and their progression is stopped despite stress increase. When the distance between two SSBs is significantly small, the buckles can have their fronts merge to form one buckle when stress is increased (2.8c). These interactions have been related to the elasticity mismatch between the film and the substrate defined by the Dundurs' coefficient, which is given as:

$$\alpha = \frac{\bar{E}_f - \bar{E}_s}{\bar{E}_f + \bar{E}_s}, \tag{2.1}$$

where $\bar{E}_f$ and $\bar{E}_s$ correspond to the reduced Young's moduli of the film the substrate, respectively. The reduced Young's modulus $\bar{E}_i$ is given as:

$$\bar{E}_i = \frac{E_i}{\left(1 - v_i^2\right)}. \tag{2.2}$$

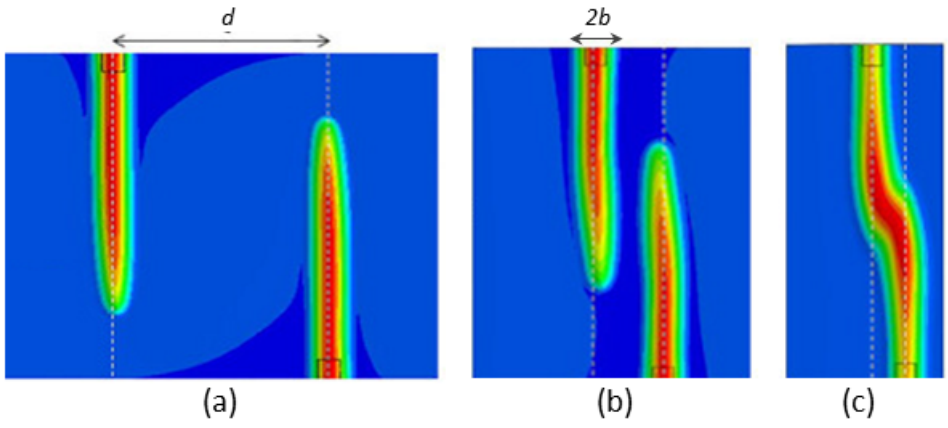

Figure 2.8: Equilibrium shapes of SSBs propagating in opposite directions at various separating distances d obtained by FEM simulations of nickel plate with thickness $h = 200$ nm on polycarbonate substrate: (a) no interaction of the SSBs (b) slight interaction at buckle fronts (c) coalescence of the SSBs. [105].

A mechanical analysis by finite element simulations of 200 nm thick nickel film on PC substrate with a compressive stress of 2.3 GPa has shown that such interactions are influenced by the elastic properties of the system. An interaction mapping of SSBs (shown in Fig. 2.9) was then developed as a function of the Dundurs' coefficient α and the distance d between the two interacting SSBs (Fig. 2.9).

The mapping shows three behaviours (coalescence, interaction, non-interaction) of two propagating SSBs extracted from FEM simulations as a function of Dundurs' parameter α and a normalised inter-buckle distance $\bar{d}$, where $\bar{d} = d/2b$. The mapping is divided into three regions and denoted as C, I and NI representing domains of coalescence, interaction and no-interaction areas, respectively. The boundary between (C) and (I) domains is labelled $\bar{d}_{C/I}$ and the boundary between (I) and (NI) domains is labelled $\bar{d}_{I/NI}$. For a rigid substrate (where α = -1), $\bar{d}_{C/I}$ is about 1, therefore coalescence is expected when d is less than $2b$. The interaction domain for a rigid substrate is limited to $\bar{d}_{I/NI} = 1.2$. This means that two SSBs on a rigid substrate do not interact when their centre-to-centre distance is higher than 20% of their widths. The map further shows that $\bar{d}_{C/I}$ and $\bar{d}_{I/NI}$ do not significantly change up to $\alpha = 0.5$. As α tends towards +1 from 0.5, there is an increase in both $d_{C/I}$ and $\bar{d}_{I/NI}$. For instance, for a soft substrate where $\alpha = 0.94$, coalescence may be observed up to $d_{C/I} = 1.2$ and interaction may also be observed up to $d_{I/NI} = 5$.

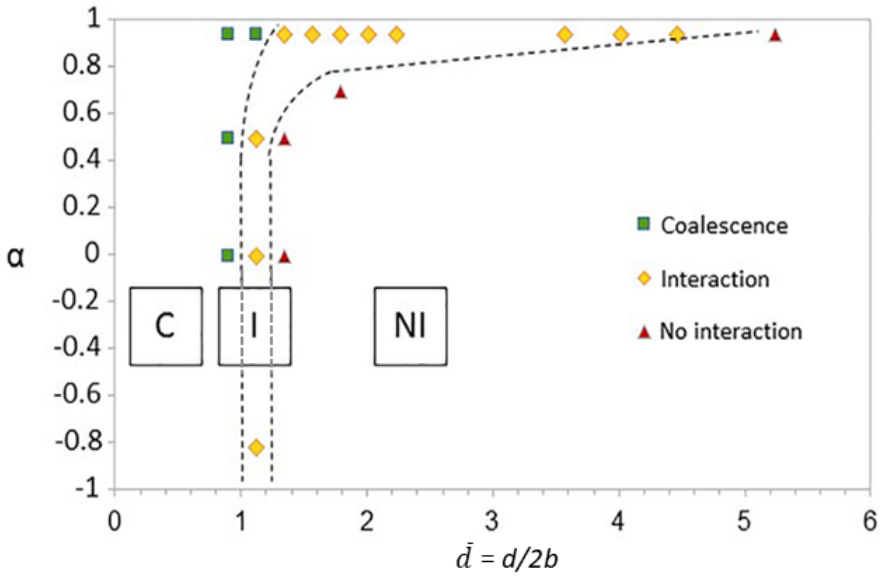

Figure 2.9: Interaction mapping of two SSBs as a function of *alpha* and inter-buckle distance d developed by FEM simulations of 200 nm thick Ni at compressive stress $\sigma = 2.3$ GPa [105].

2.2.3.1 Attraction and Wrapping of Progressing SSBs

The interactions of MoS_2 buckles have been investigated to check for similarities with reported thick metallic films. Figs. 2.10 and 2.12 show the evolution of SSBs of 1L MoS_2/PEEK (h = 1.0 nm) and 3L MoS_2/PEEK (h = 6.0 nm), respectively at different stages of their propagation, under increasing applied strain. As usual the propagation of the buckles occurs perpendicular to the compression axis. The buckles progress towards each other as the strain increases with their fronts tapered and eventually flatten out. In both samples, the trajectory of buckles dips slightly, reflecting a form of attraction between two fronts as they propagate towards each other.

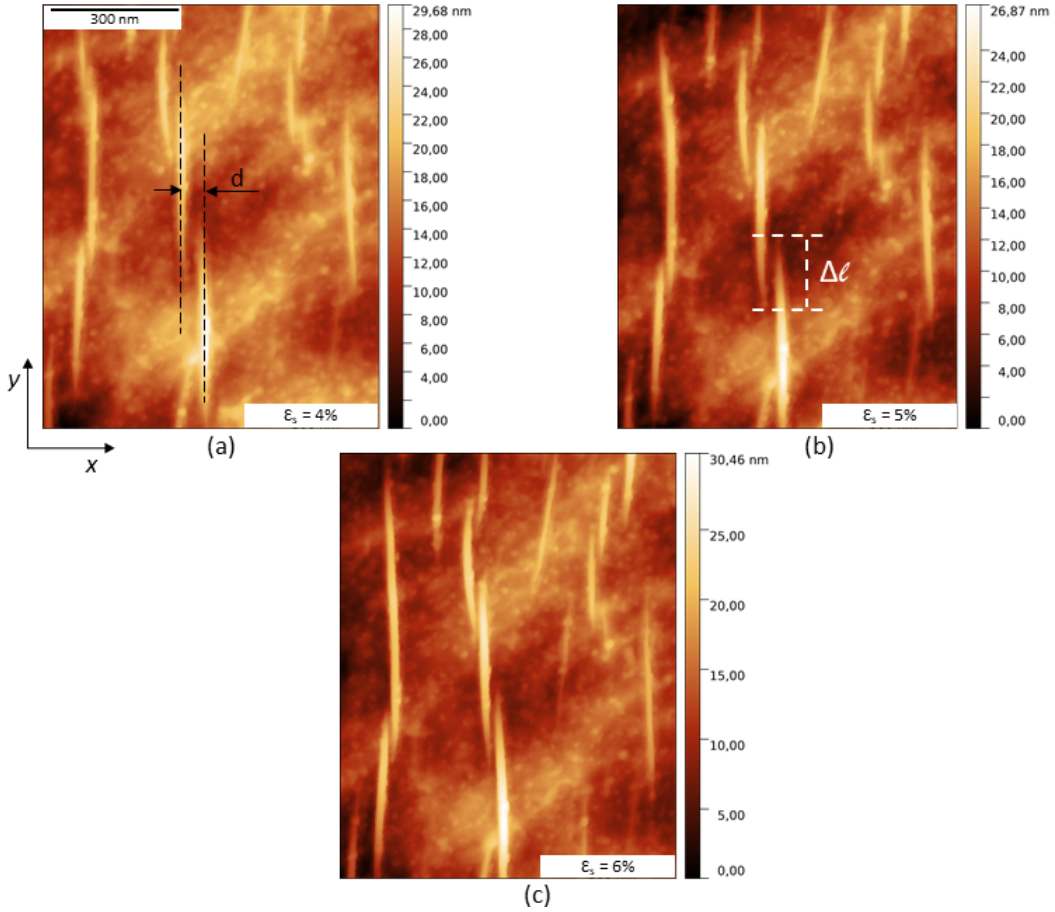

Figure 2.10: Evolution of SSBs of 1L MoS_2/PEEK (h = 1 nm) with increasing deformation (a) $\varepsilon_s = 4\%$ (b) $\varepsilon_s = 5\%$ (c) $\varepsilon_s = 6\%$. d is the centre-to-centre distance between the two SSBs propagating in opposite direction and Δl is the propagation of one buckle with respect to the other.

The evolution of 1L MoS_2/PEEK is shown in Figs. 2.10a, b and c corresponding to the sample surface at $\varepsilon_s = 4\%$, 5% and 6%, respectively. It should be noted that buckling occurred between 3% and 4% strain but due to the difficulty of gradual increase in strain using the manual micro-

compression device, it was not possible to follow the nucleation and initial propagation of the buckles.

At $\varepsilon_s = 4\%$, two buckles with similar size ($\delta = 8.5$ nm and $2b = 40$ nm) observed in the scanned area are spaced apart with distance $d = 53$ nm (measured centre to centre) indicated with broken lines in Fig. 2.10a. The interaction between the two buckles is graphically described by the evolution of their morphologies in Fig. 2.11. As the compressive strain increases, buckle deflection δ increases to 12.4 nm at $\varepsilon_s = 6\%$ (Fig. 2.11a). There is a gradual decrease in the buckle width $2b$ from 40 nm at $\varepsilon_s = 4\%$ to 35 nm at $\varepsilon_s = 6\%$ (Fig. 2.11b). Also observed is the progressive decrease in the d value from 53 nm at $\varepsilon_s = 4\%$ to 38 nm at $\varepsilon_s = 6\%$ (Fig. 2.11c). The trend is similar for almost all the buckles observed on this sample. An increase in the propagation of the buckle fronts represented as Δl is observed as ε_s is increased from 4% to 5% but beyond Δl remains constant from $\varepsilon_s = 5\%$ to 6% (Fig. 2.11d), indicating an arrest in their propagation despite the strain increase. This further confirms the attraction phenomenon between the two buckles, just as reported in the case of Ni film on PC [105].

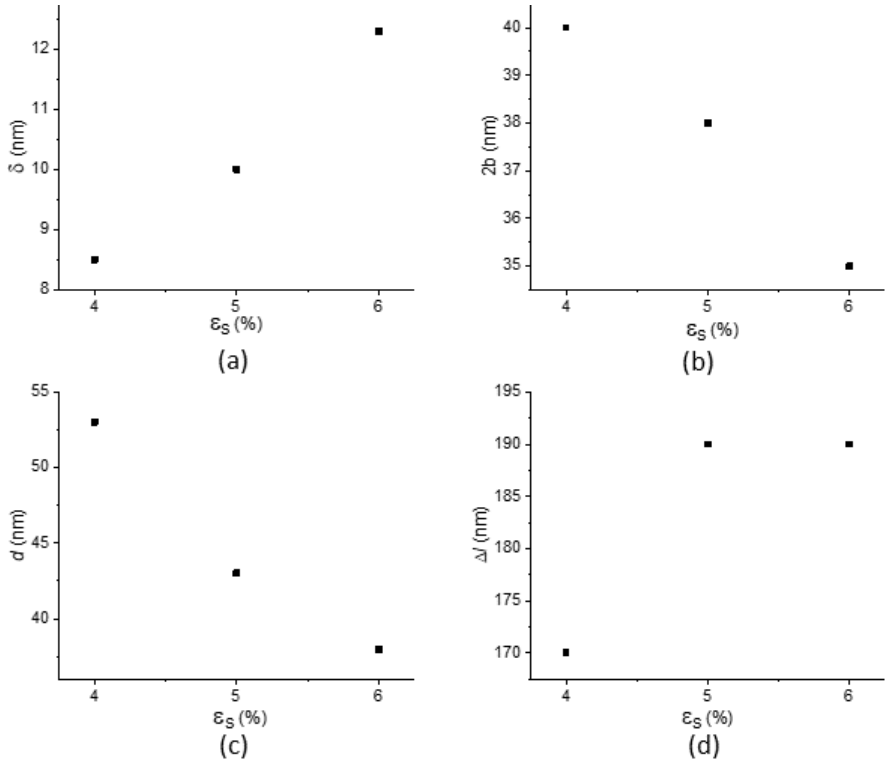

Figure 2.11: Evolution of the morphologies of two 1L MoS_2 SSBs propagating in opposite direction as ε_s increases from 4% to 6%. (a) maximum deflection δ (b) buckle width $2b$ (c) centre to centre distance d of the two SSBs (d) Propagation (Δl) of one SSB with respect to the other.

Fig. 2.12 shows the evolution of 3L MoS_2/PEEK with a, b and c corresponding to the sample at $\varepsilon_s = 4\%$, 5% and 6%, respectively. Just as it was observed on 1L MoS_2/PEEK sample, the fronts of the buckles are tapered but the change in the trajectory of propagation is slightly more obvious in the 3L MoS_2/PEEK sample as two buckles in close proximity propagate towards each other as indicated by the white dashed circles.

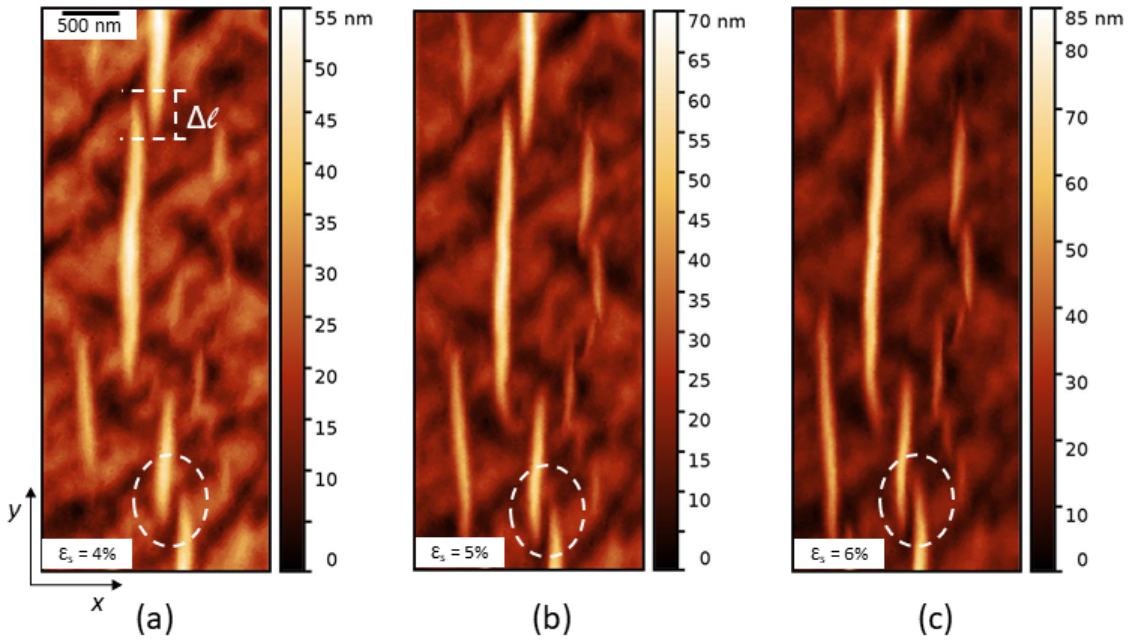

Figure 2.12: Evolution of SSBs of 3L MoS_2/PEEK (h = 6 nm) with increasing deformation (a) $\varepsilon_s = 4\%$ (b) $\varepsilon_s = 5\%$ (c) $\varepsilon_s = 6\%$.

The interaction between two buckles in this sample is described by the graphs in Fig. 2.13. For two buckles of similar size, deflection δ increases from 25 nm at $\varepsilon_s = 4\%$ to 51 nm at $\varepsilon_s = 6\%$ (Fig. 2.13a). Similar to what was observed in 1L MoS_2 SSB, a gradual decrease in buckle width $2b$ is observed as ε_s is increased (Fig. 2.13b). The centre to centre distance d of the two SSBs shows only a slight increase with increasing strain (Fig. 2.13c). An increase in the propagation of the buckle fronts is also observed and represented as Δl (Fig. 2.13d).

In conclusion, we have observed similarities in the interactions of SSBs of the both 1L and 3L MoS_2 and Ni plate already reported in the literature, particularly a slight tilt in the buckle front of 3L MoS_2 SSBs. We also observed an apparent decrease in buckle width as strain increases which is more surprising.

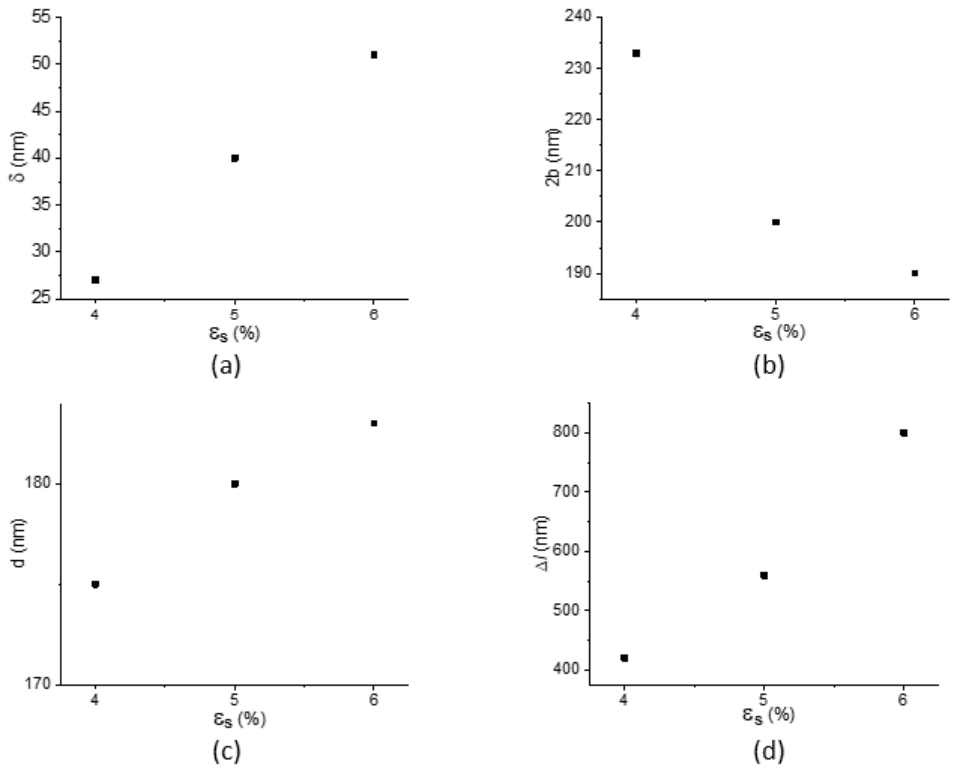

Figure 2.13: Evolution of the morphologies of two 3L MoS_2 SSBs propagating in opposite direction as ε_s increases from 4% to 6%. (a) maximum deflection δ (b) buckle width $2b$ (c) centre to centre distance d of the two SSBs (d) Propagation (Δl) of one SSB with respect to the other.

2.2.3.2 Coalescence of Buckles

When two buckles propagate towards each other, there is a possibility that they coalesce into a single buckle, particularly when the inter-buckle distance, d, is less than the buckle width, $2b$. This implies that the buckles are almost face to face and a frontal collision can occur [110]. Buckle coalescence can also occur even if $d > 2b$ when the elastic contrast between the film and substrate is high enough (*i.e.* in cases of high Dundurs' coefficient) [105].

Fig. 2.14 illustrates the coalescence of 1L MoS_2/PEEK buckles, obtained as compression strain increases from 4% to 6%. Two buckles with their fronts highlighted by dashed white circle in Fig. 2.14a at $\varepsilon_s = 4\%$ appear to propagate in different directions, with the upper buckle blocking the path of the lower. As they propagate at $\varepsilon_s = 5\%$ (Fig. 2.14b), the lower buckle continues in its original direction. However, the upper buckle appears to change its direction of propagation caused by an attraction to the lower buckle (the black arrow points in the initial direction of the propagation of the buckle). There appears to be a discontinuity in the propagation of the upper

buckle and the lower buckle approaches the upper just before contact is made. At $\varepsilon_s = 6\%$, shown in Fig. 2.14c, the two buckles coalesce into a single buckle (with values of $2b$ and δ increasing from 33.9 nm and 9.6 nm at $\varepsilon_s = 5\%$, to 37.3 nm and 15 nm, respectively). It is also observed that the resulting buckle takes the direction of the direction of the lower buckle. The shifting of the upper buckle suggests a reorganisation of the buckle structures and film movement as strain increases.

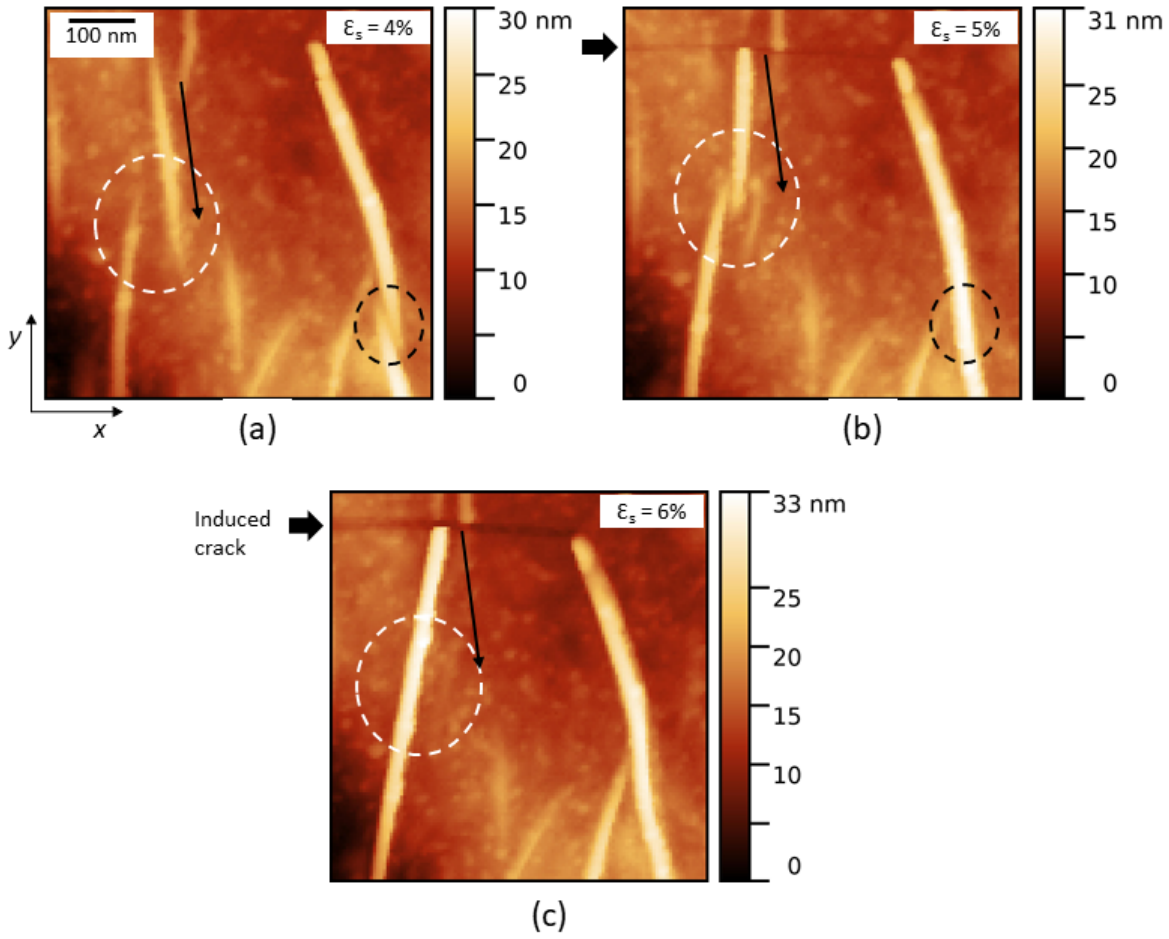

Figure 2.14: Coalescence of SSBs of 1L MoS_2/PEEK (h = 1 nm) with increasing strain (a) $\varepsilon_s = 4\%$ (b) $\varepsilon_s = 5\%$ (c) $\varepsilon_s = 6\%$.

Another coalescence of two other buckles is observed as strain is increased from 4% to 5% shown by dashed black circle in Fig. 2.14a. Initially, the two buckles (with $2b = 48$ nm) have similar direction of propagation and are in proximity to each other ($\bar{d} = d/2b = 0.5$). At $\varepsilon_s = 5\%$, an expansion on the sides of the buckle fronts causes them to merge and become a single buckle, as shown in Fig. 2.14b. Several other cases of similar buckle coalescence are observed in different

regions across the sample surface.

Similar occurrence is observed in 3L MoS_2/PEEK and shown in Fig. 2.15 where two SSBs propagating towards each other merge and form a single large buckle as strain is increased. There is a high tendency for buckle nucleation and propagation along the edges of surface defects of the substrate. The buckles continue to propagate as strain increases without crossing the grooves (defects) on the substrate surface. As in the previous cases, two propagating buckles whose fronts are close to each other ($\bar{d} = 0.9$) at 4% strain (dashed white circle in Fig. 2.15a) continue in their direction of propagation as strain is increased. They are observed to coalesce at $\varepsilon_s = 6\%$ (Fig. 2.15c). The lower end of the buckle (circled in black) has its direction of propagation changed as it is attracted to a smaller buckle for coalescence to occur (the initial direction of the buckle propagation is indicated by the small black arrow). Just as earlier stated, coalescence depends on the normalised inter-buckle distance $\bar{d}$ as no coalescence is observed for large value of $\bar{d}$ (as seen in Fig. 2.12).

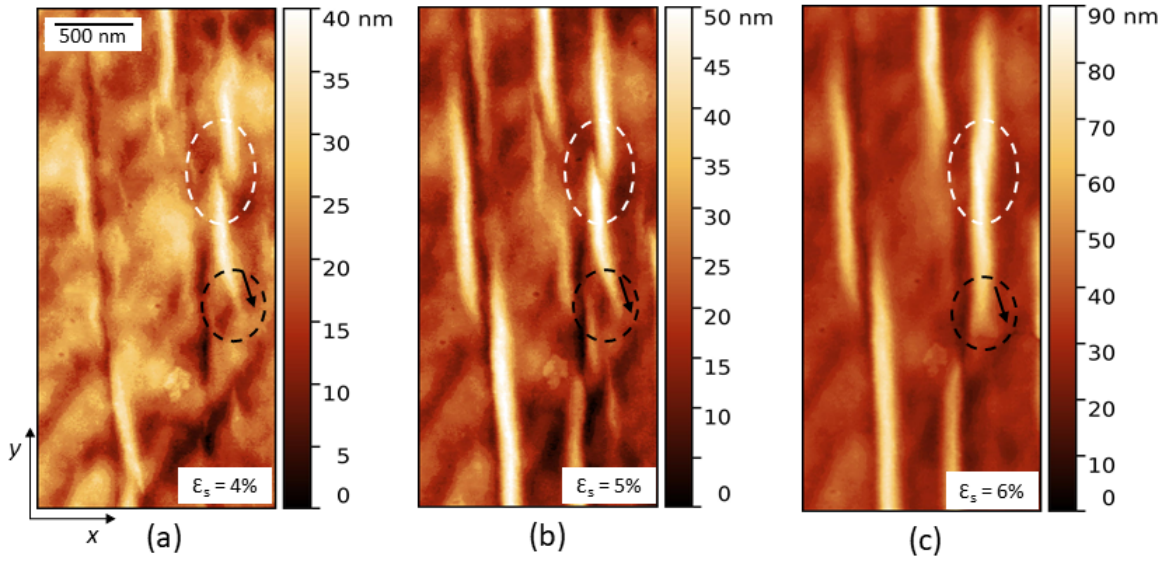

Figure 2.15: Coalescence of SSBs of 3L MoS_2/PEEK (h = 6 nm) with increasing strain (a) $\varepsilon_s = 4\%$ (b) $\varepsilon_s = 5\%$ (c) $\varepsilon_s = 6\%$.

Fig. 2.16 highlights that buckles which are not nucleated at the edges of the substrate grooves can cross the groove and continue with their propagation. Examples of these buckles where the surface defects are inclined at an angle to the direction of SSBs propagation are seen in Fig. 2.16a. The propagation and coalescence of the buckles are not hindered by the substrate defects

as buckles in white circles can be seen coalesce in Fig. 2.16b. Another interesting phenomenon to note is the gradual diminishing and eventual disappearance of some small buckles as compression is increased. Examples of these buckles are shown by the white arrows in Fig. 2.16a. At $\varepsilon_s = 6\%$ (Fig. 2.16b), these two buckles are observed to have flattened out and the buckles beside them are observed to be larger, suggesting that the smaller buckles collapse and the film slides over the substrate surface into the bigger buckles.

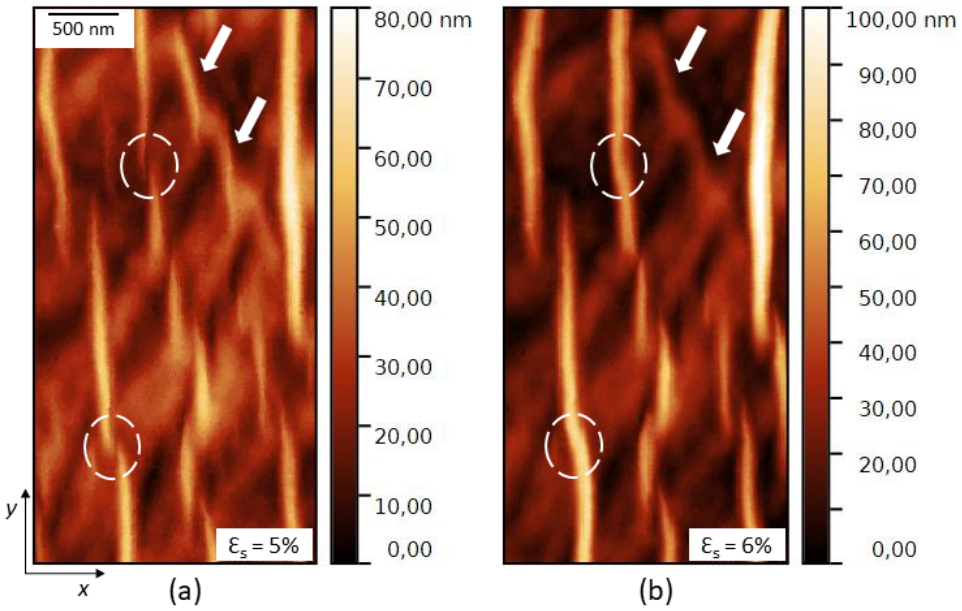

Figure 2.16: Coalescence of SSBs of 3L MoS_2/PEEK and disappearance of small with increasing strain (a) $\varepsilon_s = 5\%$ (b) $\varepsilon_s = 6\%$.

These interactions should have allowed the extraction of the elastic property of the film (since that of the substrate is known) using the buckle interaction mapping (see Fig. 2.9). However, we note that the simulations to generate data for this mapping were performed for a given uniaxial stress σ of 2.3 GPa which is different from our experiment where maximum stress was about 80 MPa. Therefore, the difference in the imposed stress for the FEM simulations and our experimental procedure increases the margin of error in the extraction of α. Also, the mapping gives a range of α depending on the interaction of the buckles observed. The FEM study presents the full data of the interactions of all the buckles. Whereas, our data is limited to the regions scanned which is not sufficient enough to have a full statistics of all interactions of the SSBs. Therefore, we have decided to use the morphology of the buckles for the extraction of the elastic

modulus of the film.

2.2.4 *In-situ* Cyclic Compression

Both samples (1L and 3L MoS_2 films) were progressively compressed to $\varepsilon_s = 6\%$ and gradually relaxed to 0%, then followed by another loading up to 6% substrate strain. Data from buckles are plotted as a function of substrate strain ε_s and shown in Fig. 2.17. Buckling structures were first observed at $\varepsilon_s = 4\%$ in both samples and this explains the jump (indicated by black arrows) in the deflection and widths of the buckles.

A general overview of the evolution of both maximum deflection δ and width $2b$ of the buckles of both samples shows a good agreement between the unloading and reloading cycles. In both samples, buckles are still observed after the complete removal of external strain (*i.e.* when $\varepsilon_s = 0$). This is linked to presence of internal strain in the films, labelled ε_0, in the following. For the 3L MoS_2 (Fig. 2.17a), δ increases gradually as ε_s is increased. The evolution of the buckle width (represented as b being half the measured width) shows a slight decrease as strain increases. The evolution of the 1L MoS_2 film buckle presents an interesting case as shown in Fig. 2.17b. As shown by a black arrow, there appears to be a change in slope of the δ evolution at $\varepsilon_s = 4\%$, which is typically unexpected. Also, there is an obvious reduction in b as ε_s increases. This suggests re-adhesion of the MoS_2 layer to the substrate at the buckle edges. This could be due to a form of sliding of the film with respect to the substrate, which we will refer to as "buckling-induced sliding" of the film. As the flat film tries to extend towards the buckle, the buckle edge is consequently pushed in, thereby forcing a re-adhesion along the edges; thus the buckle width is reduced.

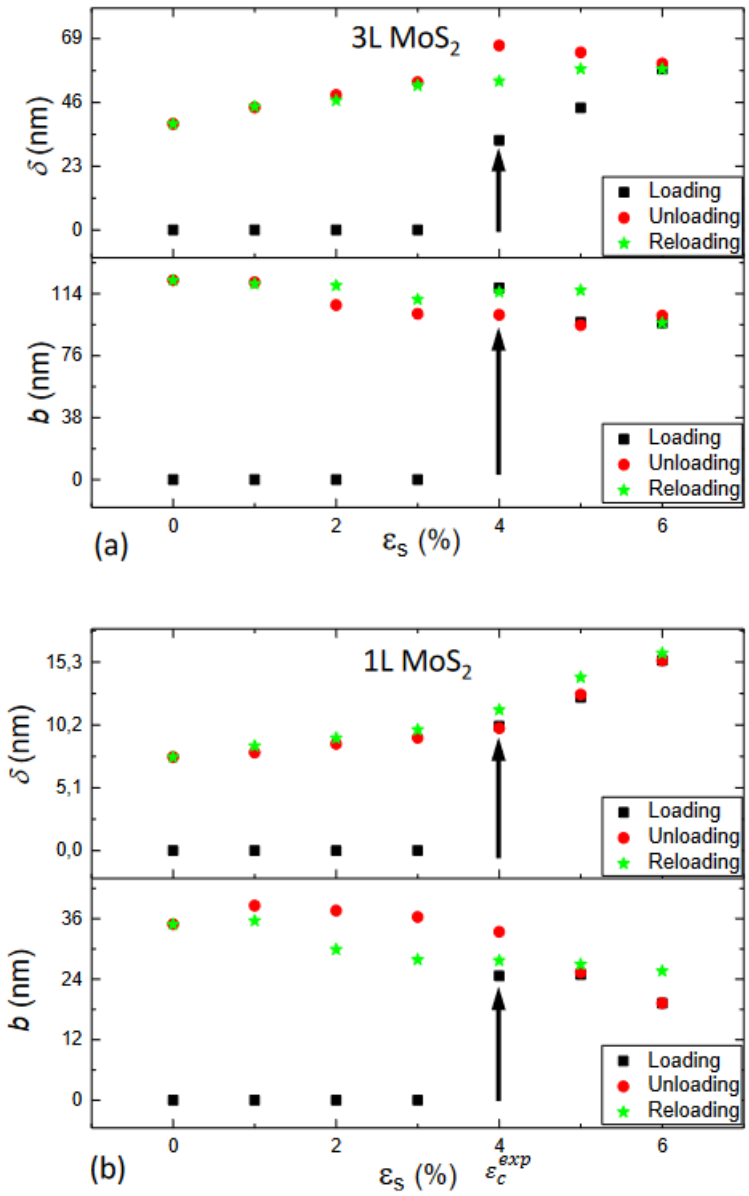

Figure 2.17: Evolution of the maximum deflection δ and half width of the buckle b of (a) 3L MoS_2 film, and (b) 1L MoS_2 film, as a function of applied strain on the substrate ε_s. The black arrows show the jump observed at $\varepsilon_s = 4\%$, which corresponds to the experimental critical buckling strain ε_c^{exp}.

2.3 Summary

This chapter discusses the response of ultrathin MoS_2 films to uni-axial compressive strain. The first section discusses the mechanical properties of PEEK substrate and its viscoelastic nature. The substrate is observed to remain in its elastic region up to 6% of compressive strain. Also, a home-fabricated compression device is described. This device allows samples to be uni-axially

strained and can be incorporated to the AFM microscope which allows *in-situ* scanning of the sample.

The second section discusses AFM observations of the strained films. Straight-sided buckles were observed when the imposed strain is up to 4%, in both 1L and 3L MoS_2 films. Interactions like attraction, wrapping and coalescence of buckles propagating in opposite directions, depending on the distance between the buckles, were observed. These interactions have already been reported in strained metallic thick films where they were explained by the elasticity mismatch of the film/substrate system based on FEM simulations. In the study, an interaction mapping was developed which could be useful for the extraction of the Dundurs' coefficient α of a film/substrate system. However, the huge difference in stress between the model and our experiment could render the interaction mapping inaccurate for the extraction of α of our sample and therefore, we have opted to use the morphology of observed buckles.

A number of unexpected behaviour of the buckles were observed. These observations include; an increase in the inter-buckle distance d with SSBs interaction as strain ε_s is increased, also, the re-adhesion of film leading to decrease in buckle width b when ε_s is increased and the coalescence of two SSBs separated by a long distance. All these observations will be discussed in Chapter 3 in the context of strain-induced sliding of the film.

2.4 Résumé en Français

Le comportement mécanique des films métalliques sous compression a été largement étudié par le passé au moyen d'expériences et de simulations. Dans de nombreux cas, en particulier dans le cas de la compression uni-axiale, on a observé que les flambages rectilignes (SSB) se propagent avec l'augmentation de la contrainte et dans une direction perpendiculaire à l'axe de compression. Des interactions entre deux SSB se propageant dans des directions opposées ont également été rapportées et se sont avérées dépendre de la distance qui les sépare et être liées aux propriétés mécaniques du système film/substrat. Il est donc intéressant d'étudier par des expériences et de comparer le comportement mécanique du MoS_2 ultra-mince à ce qui a été observé dans les films métalliques épais. Après le transfert de film réussi décrit au Chapitre 1, l'intérêt de ce chapitre est d'observer et de décrire la réponse des films de MoS_2 2D sur des substrats en PEEK à des contraintes de compression.

I. Propriétés mécaniques du PEEK

Le PEEK a été choisi comme substrat pour cette étude en raison de certaines de ses propriétés physiques et mécaniques intéressantes (module d'Young de 4 GPa). Contrairement à de nombreux autres polymères, l'eau ne joue pas un rôle important dans son élasticité. Des essais de compression cyclique ont été réalisés sur le substrat PEEK afin de déterminer ses performances et la manière dont il peut influencer la réponse du film transféré. La courbe contrainte-déformation obtenue à partir de l'essai révèle que le PEEK présente une hystérésis élastique typique des matériaux viscoélastiques. Cela indique une perte d'énergie au cours de chaque cycle de chargement et de déchargement. Jusqu'à une déformation de 6%, on observe que le PEEK reste dans son régime élastique et que sa dimension initiale est récupérable. Aucune déformation permanente n'a été observée après quatre cycles.

II. Description du mécanisme de compression des échantillons

Pour induire une contrainte sur les échantillons préparés, un dispositif de micro-compression manuelle qui s'adapte à l'AFM a été conçu et fabriqué localement, permettant une compression et une imagerie in-situ. Le dispositif de compression permet de déformer les échantillons par

compression uni-axiale du substrat afin de déclencher une réponse du film. La contrainte est imposée à l'échantillon en tournant manuellement la vis reliée à la mâchoire où l'échantillon est maintenu. La déformation peut être directement déterminée en mesurant la distance parcourue par la mâchoire.

III. Observations expérimentales

1. Emergence de rides droites (SSB)

Des films de MoS_2 1L (1 monocouche) et 3L (3 monocouches) ont été soumis à des contraintes de compression graduelles. Des zones spécifiques des échantillons ont été scannées après chaque étape de déformation de 1% afin d'observer l'évolution de la surface de chaque échantillon, comme le montre la Fig. 2.18. Les images AFM des deux échantillons montrent des défauts de surface des substrats dûs au polissage (indiqués par des flèches bleues dans les Fig. 2.18a et d). Les fissures du film induites par le transfert sont représentées par les lignes noires en pointillés, ce qui permet de mesurer l'épaisseur du film. À une déformation de 4%, l'apparition de SSB (indiquées par des flèches noires dans les Fig. 2.18c et f) a été observée, ce qui signifie que la déformation expérimentale de flambage (la déformation au-delà de laquelle le film se déforme) se situe entre 3 et 4%.

Ces flambages rectilignes semblent se propager dans une direction perpendiculaire à l'axe de compression, comme cela a été observé et rapporté dans la littérature pour des films métalliques comprimés uni-axialement. Pour des films 1L, les profils établis sur différentes rides montrent une déviation δ d'environ 10 nm et une largeur $2b$ d'environ 42 nm. Les dimensions des rides observées sur film 3L donnent quant à elles une déviation δ d'environ 25 nm et une largeur de 180 nm. Dans les deux cas, le rapport entre l'épaisseur du film h et la moitié de la largeur de la ride b est largement inférieur à 1. Ceci satisfait la condition de validité de la théorie d'Euler qui sera discutée dans le chapitre suivant.

2. Fissures induites sur le film par la contrainte

Au fur et à mesure de l'augmentation de la contrainte de compression, on observe une augmentation de la taille des rides et l'apparition de fissures à la surface du film. Les fissures induites par

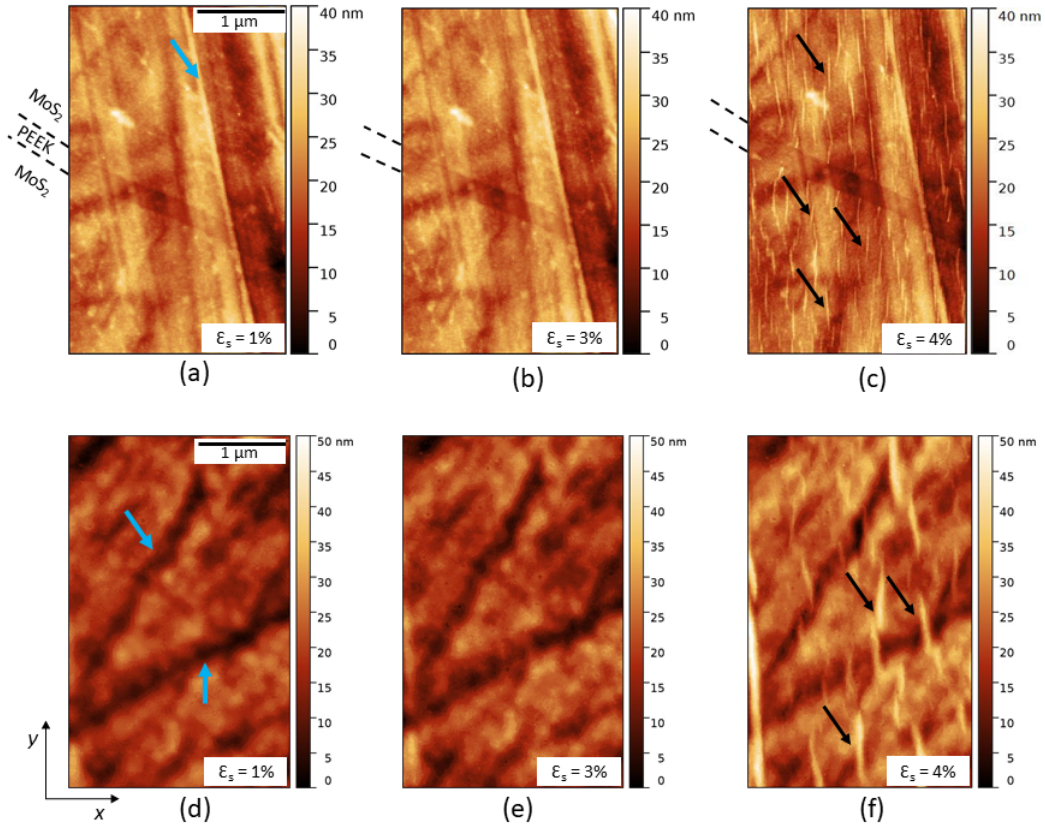

Figure 2.18: Observation par AFM de 1L MoS_2 sur PEEK pendant la contrainte de compression ε_s = (a) 1%, (b) 3%, (c) 4%, et de 3L MoS_2 sur PEEK à ε_s = (d) 1% (e) 3%, (f) 4%. Les fleches bleues indiquent les rayures résiduelles sur la surface du PEEK et les fleches noires indiquent les SSB.

la déformation se propagent dans une direction parallèle à l'axe de compression. Cela est dû à l'effet de Poisson, car la déformation causée par l'application d'une contrainte le long de l'axe x entraîne l'étirement (en tension) du film le long de la direction perpendiculaire (axe y). Lorsque la compression du substrat augmente, le film atteint un point de rupture et une fissure apparaît. Une nouvelle augmentation de la déformation appliquée entraîne une augmentation de la largeur de la fissure, ce qui suggère un mouvement apparent du film sur le substrat. Dans certains cas, les fissures traversent des rides et mettent brusquement fin à leur propagation. On observe également que de plus petites rides proches de la trajectoire des fissures disparaissent après l'apparition de ces dernières. Nous croyons fermement que la fissure relâche localement la contrainte dans le film, ce qui provoque l'aplatissement du film.

3. Interactions entre les rides

Les interactions entre des SSB de films minces de nickel sur polycarbonate se propageant dans des directions opposées, ont été observées par AFM et étudiées par simulation par éléments finis par G. Parry *et al*[1]. Les rapports de l'étude suggèrent qu'en fonction de la distance d qui les sépare, deux SSB se propageant dans des directions opposées peuvent être attirées l'une vers l'autre avec leurs fronts légèrement déviés de leur direction de propagation initiale et s'enrouler l'une autour de l'autre, après quoi leur propagation est stoppée malgré l'augmentation de la contrainte. Lorsque la distance entre deux SSB est significativement faible, les fronts des rides peuvent fusionner pour ne former une seule ride en cas d'augmentation supplémentaire de la contrainte. Ces interactions sont reliées au défaut d'élasticité entre le film et le substrat, défini par le coefficient de Dundurs α, qui décrit le module d'élasticité du système film/substrat. Ainsi, en comparant le type et la distance d'interactions obtenues avec des rides de MoS_2 à ceux obtenus pour des rides sur films minces, il peut être possible d'extraire des propriétés mécaniques telles que le module d'Young.

Nous avons observé des interactions similaires entre les rides apparaissant sur des films de MoS_2 1L et 3L lorsque la déformation augmente. Ces rides progressent l'une vers l'autre, avec leurs fronts effilés, au fur et à mesure que la déformation augmente, puis finissent par s'aplatir. Dans les deux échantillons, leur trajectoire s'infléchit légèrement, reflétant une forme d'attraction entre deux fronts lorsqu'ils se propagent l'un vers l'autre, comme le montre la Fig. 2.19. Nous avons également observé la coalescence de 2 SSB à proximité immédiate ($d < 2b$) lorsque la déformation augmente, comme dans le cas des films métalliques. Malgré des phénomènes similaires dans nos échantillons et dans ceux rapportés dans la littérature, nous ne sommes pas en mesure d'extraire le module d'Young du MoS_2 sur la base de l'interaction des SSB en raison de la différence de contrainte appliquée dans l'étude FEM et dans notre expérience. Par conséquent, une méthode basée sur la morphologie des rides a été utilisée pour déterminer le module d'Young du film et est discutée au Chapitre 3.

[1] C. Coupeau, R. Boijoux, Y. Ni, and G. Parry, "Interacting straight-sided buckles: an enhanced attraction by substrate elasticity," Journal of the Mechanics and Physics of Solids, vol. 124, pp. 526–535, 2019.

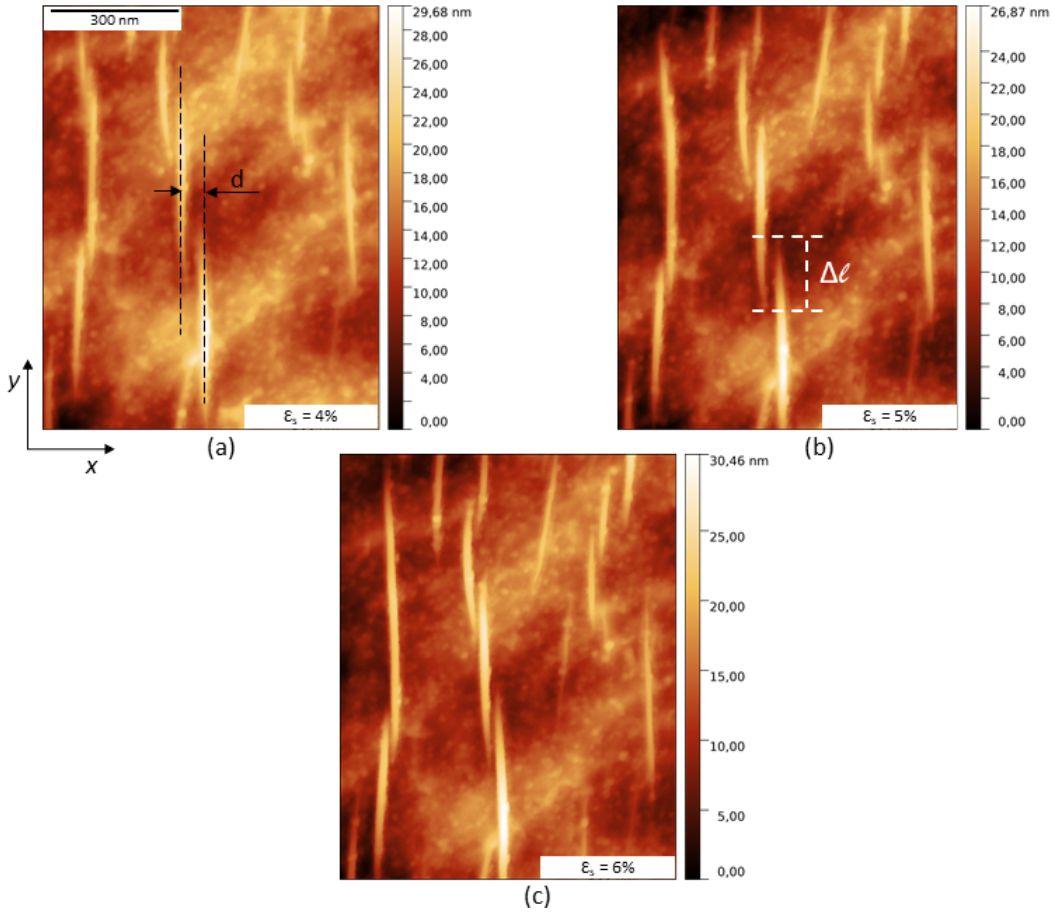

Figure 2.19: Évolution des SSB de 1L MoS_2/PEEK (h = 1 nm) avec une déformation croissante (a) ε_s = 4% (b) ε_s = 5% (c) ε_s = 6%. *d* est la distance centre à centre entre les deux SSBs se propageant dans des directions opposées. Δl correspond à la distance de propagation des fronts de rides.

4. Déformation cyclique

Les deux types d'échantillons ont été progressivement déformés jusqu'à 6% et progressivement relaxés jusqu'à 0%, puis à nouveau déformés jusqu'à 6%. Dans les deux échantillons, des rides étaient toujours présentes malgré l'élimination complète de la contrainte externe. Ce phénomène a été lié à la présence d'une déformation interne dans le film. Comme prévu, une augmentation de la déviation d'une ride est observée à mesure que la déformation augmente, mais de manière inattendue, on observe une réduction de la largeur de la ride avec l'augmentation de la déformation. Cela suggère une réadhésion du film sur les bords de la boucle. Cela pourrait être dû à une forme de glissement du film par rapport au substrat, que nous appellerons "glissement induit par le flambage" du film. Lorsque le film plat tente de s'étendre vers la ride, le bord de la ride est par conséquent poussé vers l'intérieur, ce qui force une réadhésion le long des bords; la largeur de

la ride est donc réduite. Les différentes observations expérimentales faites dans ce chapitre sont analysées dans le chapitre suivant.

Chapter 3

Analyses of Strain-Induced Buckling on MoS_2 Film

Contents

3.1 Thin Plates under Compression 72

3.1.1 Föppl-von Kármán Model of Thin Plates 72

3.1.2 The Straight-Sided Buckle (Euler's column) 75

3.1.3 Influence of Substrate Elasticity on Buckling Phenomenon 78

3.1.4 Effect of Film Sliding on Maximum Deflection 81

3.2 Extraction of MoS_2 Young's Modulus from Buckle Morphology . . . 83

3.3 Strain in 2D MoS_2 Films 86

3.3.1 Total Strain in MoS_2 Film 87

3.3.2 Internal Strain in MoS_2 Film 87

3.4 Analyses of MoS_2 Buckle Evolution 89

3.4.1 Predicted Critical Buckling Strain Versus Observed Critical Buckling Strain 89

3.4.2 Determination of Interfacial Adhesion Energy 90

3.4.3 MoS_2 Buckle Evolution 92

3.5 Summary 100

3.6 Résumé en Français 102

Objective

Generally, the elastic behaviour of a mechanically stressed material is observed by modifications in its dimensions, which is studied in the framework of linear elasticity for deformations. The modifications in dimensions are then related to the first derivatives of the displacements [111]. When we consider thinner materials under stress, there is a change in their shape in addition to the change in their dimensions. It is therefore, necessary to consider the relationship between the mechanical stress (or strain) and the response of the material in the form of change of shape. Hence, the buckling phenomenon is analysed in this context.

This Chapter is divided into four sections. The first section explores the literature on buckling of thin plates in the frame-work of the Föppl-von Karman equations. In the second section, we describe the extraction of MoS_2 Young's modulus using parameters from the buckle morphology. The third section discusses strain transfer from compressed substrate to the film and also the internal strain present in the film which is independent of substrate compression. The fourth section focuses on the analyses of our experimental data to determine and quantify the displacement of the film on the substrate due to interfacial sliding and shearing with respect to applied strain.

3.1 Thin Plates under Compression

3.1.1 Föppl-von Kármán Model of Thin Plates

We recall the work of A. Föppl [46] and T. von Kármán [47] which has been elaborately described in the works of others, such as H.L. Langhaar [112]. The work has been used by J.W. Hutchinson and Z. Suo [113] and L.B. Freund and S. Suresh [114] to model buckling-driven delamination of thin films. The FvK model is suited for the study of buckling where a vertical displacement of the film is observed. The theory takes into account the non-linear terms of the deformation characterising the flexions. Consider a film with thickness h over a rigid substrate. The film plane is defined by the orthonormal axes (O_x) and (O_y), shown in the Fig. 3.1. When compressed along the (O_x) direction, buckling is observed in the direction (O_z), perpendicular to the film plane (Fig. 3.1b).

To model the film in the framework of FvK theory, it is assumed that the film thickness is

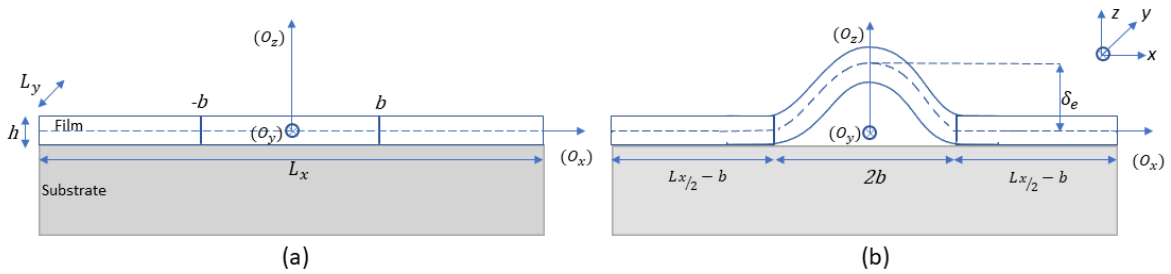

Figure 3.1: Schematic diagram of the film-substrate system (a) in flat configuration and (b) in buckled configuration.

much less than b ($h \ll b$) and the film is delaminated over a width of $2b$ along the (O_x) direction. The film is assumed to be infinite along the edges with b remaining constant. The film/substrate adhesion is not taken into account in the delaminated zone. The median plane of the supposedly infinite film is located in the middle of the film thickness, $(h/2)$, and corresponds to $z = 0$ according to (O_z). The system being invariant along the (O_y) axis, we will not consider any displacement in this direction and the characteristic quantities will be taken independent of y, thus considering the problem as two-dimensional. In this case, it is possible to show in the FvK formalism that the strain tensor within the thin film is written by [114]:

$$\varepsilon_{xx}^{rd}(x,z) = \varepsilon_{xx} - z\frac{\partial^2 w(x)}{\partial x^2}, \tag{3.1}$$

where:

$$\varepsilon_{xx} = \varepsilon_i + \frac{\partial u(x)}{\partial x} + \frac{1}{2}\left(\frac{\partial w(x)}{\partial x}\right)^2. \tag{3.2}$$

ε_i in Eq. 3.2 represents the isotropic internal strain in the initial plane and u and w represent the displacements along (O_x) and (O_z) of a point on the film located in the median plane, respectively. We recall that the dependence between the strain given by Eq. 3.1 and out-of-plane displacement w is non-linear. This displacement will be a relevant parameter to describe the deflection of the thin film in the (O_z) direction.

If we consider the film to be homogeneous and isotropic, the potential energy of the film U is

written as:

$$U = \frac{\bar{E_f} L_y}{2} \int_{-\frac{h}{2}}^{\frac{h}{2}} \int_{-b}^{b} \left(\varepsilon_{xx}^{rd}(x,z)\right)^2 dxdz, \tag{3.3}$$

where:

$$\bar{E_f} = \frac{E_f}{1 - v_f^2}. \tag{3.4}$$

$\bar{E_f}$ is the in-plane reduced elastic modulus, E_f and v_f being the Young's modulus and the Poisson's ratio of the thin film, respectively. By integrating Eq. 3.3 with respect to z, we obtain:

$$U = \int_{-b}^{b} W dx, \tag{3.5}$$

where W is the linear energy density, given as:

$$W = \frac{\bar{E_f} h L_y}{2} \left[\varepsilon_{xx}^2 + \frac{h^2}{12}\left(\frac{\partial^2 w(x)}{\partial x^2}\right)^2\right]. \tag{3.6}$$

For the system to be in equilibrium, the equations that must be satisfied are determined using a variational method which involves cancelling to the first order the differential of the potential energy of the system [115]. This leads to the two Euler equations:

$$\frac{\partial W}{\partial w(x)} - \frac{\partial}{\partial x}\left(\frac{\partial W}{\partial\left(\frac{\partial w(x)}{\partial x}\right)}\right) + \frac{\partial^2}{\partial x^2}\left(\frac{\partial W}{\partial\left(\frac{\partial^2 w(x)}{\partial x^2}\right)}\right) = 0, \tag{3.7}$$

$$\frac{\partial W}{\partial u(x)} - \frac{\partial}{\partial x}\left(\frac{\partial W}{\partial\left(\frac{\partial u(x)}{\partial x}\right)}\right) + \frac{\partial^2}{\partial x^2}\left(\frac{\partial W}{\partial\left(\frac{\partial^2 u(x)}{\partial x^2}\right)}\right) = 0. \tag{3.8}$$

By replacing W with its expression given by Eq. 3.6, and considering the relation from Eq. 3.2:

$$\frac{\partial}{\partial x}\left(\frac{\partial \varepsilon_{xx}^2}{\partial\left(\frac{\partial w(x)}{\partial x}\right)}\right) = 2\varepsilon_{xx}\frac{\partial^2 w(x)}{\partial x^2} + 2\frac{\partial w(x)}{\partial x}\frac{\partial \varepsilon_{xx}}{\partial x}, \tag{3.9}$$

Therefore, Eqs. 3.7 and 3.8 become:

$$\bar{E}_f h L_y \left[-\frac{\partial \varepsilon_{xx}}{\partial x}\frac{\partial w(x)}{\partial x} - \varepsilon_{xx}\frac{\partial^2 w(x)}{\partial x^2} + \frac{h^2}{12}\frac{\partial^4 w(x)}{\partial x^4} \right] = 0, \tag{3.10}$$

$$\frac{\partial \varepsilon_{xx}}{\partial x} = 0. \tag{3.11}$$

Eq. 3.11 shows that the uniaxial strain in the thin film, ε_{xx}, is constant. This will be taken as negative since strain is in compression and this allows us to define the positive parameter[1]:

$$\alpha^2 = 12\frac{-\varepsilon_{xx}}{h^2} \tag{3.12}$$

The equilibrium equations can then be further simplified as:

$$\frac{\partial^4 w(x)}{\partial x^4} + \alpha^2 \frac{\partial^2 w(x)}{\partial x^2} = 0, \tag{3.13}$$

$$\varepsilon_i + \frac{\partial u(x)}{\partial x} + \frac{1}{2}\left(\frac{\partial w(x)}{\partial x}\right)^2 + \frac{\alpha^2 h^2}{12} = 0. \tag{3.14}$$

These are the two FvK equations which describe the mechanical equilibrium of a thin film stressed along (O_x). In the next sub-section, these equations will be used to determine the solutions of w and u which describe a straight-sided buckle, also called Euler's column.

3.1.2 The Straight-Sided Buckle (Euler's column)

The general solution of Eq. 3.13 is given by $w(x) = c_1 sin[\alpha x] + c_2 cos[\alpha x] + c_3 x + c_4$ where the constants c_i are determined from the boundary conditions of the system. In the case of a relaxed buckle, these conditions are:

$$u(\pm b) = w(\pm b) = \left.\frac{\partial w(x)}{\partial x}\right|_{x=\pm b} = 0. \tag{3.15}$$

[1] α here is a positive parameter to define the compressive strain and is different from the Dundurs' coefficient.

It is necessary that the solution satisfies the following conditions:

$$w(x) \geq 0, \tag{3.16}$$

$$w(0) = \delta, \tag{3.17}$$

$$\left.\frac{\partial w(x)}{\partial x}\right|_{x=0} = 0, \tag{3.18}$$

where δ represents the maximum deflection of the straight-sided buckle (refer to Fig. 3.1b). The vertical displacement $w(x)$, corresponding to a single buckle with $\alpha \neq 0$ is obtained from the above conditions when:

$$\alpha^2 = \left(\frac{\pi}{b}\right)^2, \tag{3.19}$$

which therefore leads to:

$$w(x) = \frac{\delta}{2}\left(1 + cos\left[\frac{\pi x}{b}\right]\right). \tag{3.20}$$

The graphical representation of $w(x)$ is shown in Fig. 3.2. The solution, as observed, corresponds to the structure of a straight-sided buckle with width $2b$ and maximum deflection δ.

By combining Eqs. 3.19 and 3.12, we show that the deformation within the straight-sided buckle is indeed constant and equals to:

$$\varepsilon_c = -\frac{\pi^2}{12}\left(\frac{h}{b}\right)^2. \tag{3.21}$$

The Eq. 3.21 corresponds to the critical strain, above which buckling is observed on the film [113]. In terms of stress, Eq. 3.21 can equally be expressed as:

$$\sigma_c = -\frac{\pi^2}{12}\frac{E_f}{1-v_f^2}\left(\frac{h}{b}\right)^2. \tag{3.22}$$

This value ε_c correlates with the deformation from which a physical solution exists and can

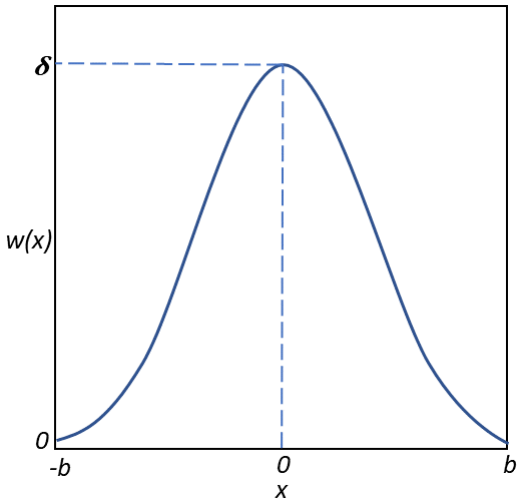

Figure 3.2: Representation of the out-of-plane displacement $w(x)$, of a straight-sided buckle of width $2b$ and deflection δ.

be found by determining the value of α from which $w(x) \leq 0$. Mathematically, this value then corresponds to the solution of the equations $\frac{\partial^2 w(x)}{\partial x^2}\Big|_{x=\pm b} = 0$. The expression for the maximum deflection δ is then obtained from Eq. 3.14 integrated between the fixed limits $x = -b$ and $x = +b$:

$$\delta = \frac{4b}{\pi}\sqrt{\varepsilon_c - \varepsilon_i}. \tag{3.23}$$

The maximum deflection δ in Eq. 3.23 has been expressed in terms of applied stress and film thickness [113] and given as:

$$\delta = h\sqrt{\frac{4}{3}\left(\frac{\sigma_i}{\sigma_c} - 1\right)}, \tag{3.24}$$

where σ_c is the critical stress above which buckling is observed, σ_i is the applied stress and h is the film thickness. Within an elastic region, stress and strain are proportional which makes the expression $\frac{\sigma_i}{\sigma_c}$ correspond to $\frac{\varepsilon_i}{\varepsilon_c}$. Therefore, Eq. 3.24 can be written as:

$$\delta = h\sqrt{\frac{4}{3}\left(\frac{\varepsilon_i}{\varepsilon_c} - 1\right)} \tag{3.25}$$

Eqs. 3.24 and 3.25 show that the maximum deflection δ of a straight-sided buckle depends on the film thickness h.

The analytical expression of the in-plane displacement $u(x)$ is then obtained from the Eq. 3.14

by integrating and considering the expressions $w(x)$ and ε_{xx} given by the Eqs. 3.20 and 3.21, respectively:

$$u(x) = \frac{\pi\delta^2}{32b} sin\left[\frac{2\pi x}{b}\right]. \tag{3.26}$$

Quantitatively, these expressions satisfactorily describe the behaviour of a straight-sided buckle as long as the FvK hypotheses remain valid: in particular, the h/b ratio must be less than 1 [113].

3.1.3 Influence of Substrate Elasticity on Buckling Phenomenon

A number of factors can influence the buckled shape of a film; one of them is the elasticity of the substrate. Studies by finite element simulations (FEM) reported by G. Parry *et al* [109] reveal how buckled structures can be influenced by the substrate elasticity. Fig. 3.3 shows the buckle profile of a film modelled on a soft substrate (it is worthy of note that the previously described FvK model is based on thin plates on rigid substrates). A careful observation of the profile reveals the presence of a depression at the foot of the buckle structure. There is also an upward stretching of the substrate under the buckled part. The overall profile of the buckle is thus modified and adopts the shape of the so-called "Mexican hat", which describes the slight sinking of the film into the substrate.

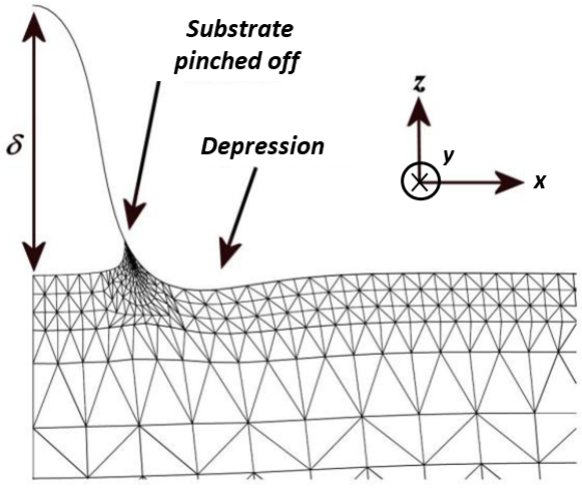

Figure 3.3: Half-profile of a buckling structure demonstrating a depression at the base of the buckle and an upward stretching of the substrate, on the edge of the delaminated part of the film from [109].

In order to quantify the influence of the substrate elasticity, two factors γ_σ and γ_δ have been

numerically determined. These correcting factors take into account the compliance of the substrate and make it possible to modify equations describing the critical stress (Eq. 3.22) for buckling and the maximum deflection (Eq. 3.24), as:

$$\sigma_c^* = \gamma_\sigma \sigma_c, \tag{3.27}$$

and

$$\delta^* = \gamma_\delta \delta. \tag{3.28}$$

γ_σ and γ_δ depend on the elastic properties of both the film and substrate. It is therefore imperative to recall from Chapter 2, the Dundurs' coefficient α which describes the elasticity mismatch between the film and the substrate, and will be useful for the analyses of the experimental data in this chapter. α is given by:

$$\alpha = \frac{\bar{E_f} - \bar{E_s}}{\bar{E_f} + \bar{E_s}}, \tag{3.29}$$

where $\bar{E_f}$ and $\bar{E_s}$ correspond to the reduced Young's moduli of the film and the substrate, respectively. We also recall that the reduced Young's modulus $\bar{E_i}$ is given as:

$$\bar{E_i} = \frac{E_i}{1 - v_i^2}. \tag{3.30}$$

The value of α ranges between -1 to 1 for any film/substrate system. For a soft film on a hard substrate, α tends towards -1 and for a hard film on a soft substrate, the value of α tends towards +1. The evolution of the correcting factors γ_σ and γ_δ as a function of α is shown in Fig. 3.4. With the introduction of the correction factors, there is a reduction of the critical stress for buckling and an amplification of the maximum deflection, when compared to the classic case of the Euler column (where $\alpha = -1$), which results from the compliance of the substrate. Experimental studies of buckling of different metallic films show an excellent agreement with the numerical results [109].

It should be noted that experiments for this study were performed with deformation measured in terms of the compressive strain ε, hence it is necessary to express the modified maximum

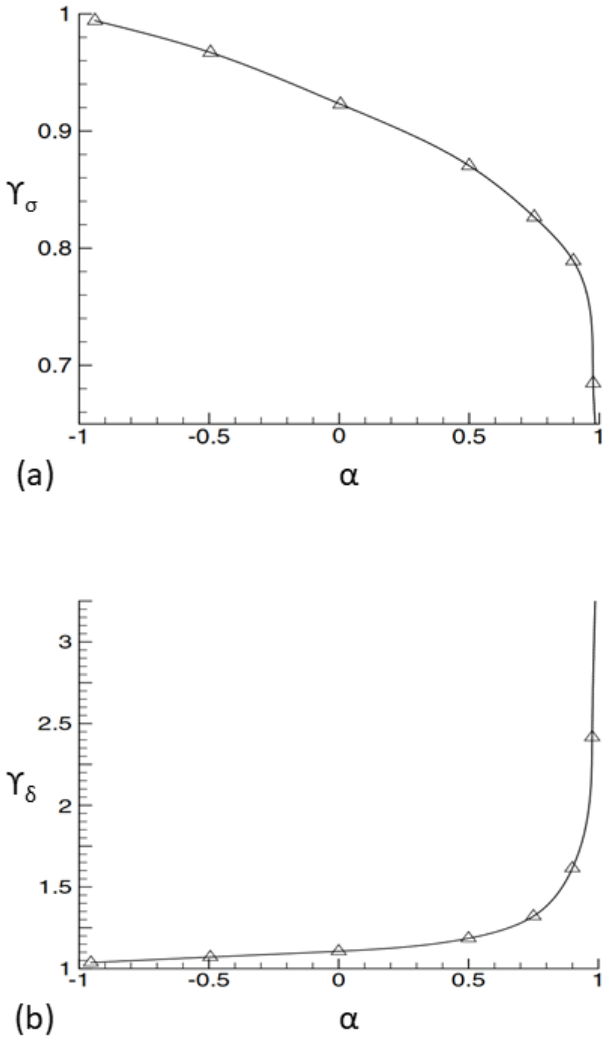

Figure 3.4: Evolution of correction factors taking into account the elasticity of the substrate. $\alpha = -1$ corresponds to the FvK modelling: (a) γ_σ applied to the critical stress and (b) γ_δ applied to the maximum deflection of the buckling structure, as a function of Dundurs' coefficient α [109].

deflection in terms of ε. Since stress σ is proportional to ε within the elastic region of a material, therefore the correction factor applied to the critical stress γ_σ is assumed to be equivalent to the correction factor to be applied to the critical strain γ_ε *i.e.* $\gamma_\sigma \equiv \gamma_\varepsilon$. We can then assume that the graph in Fig. 3.4a equally corresponds to the evolution of γ_ε as a function of α.

Therefore, when we consider the correction factor of the substrate compliance, the critical stress from Eq. 3.21 becomes:

$$\varepsilon_c^* = -\gamma_\varepsilon \frac{\pi^2}{12} \left(\frac{h}{b}\right)^2, \tag{3.31}$$

also, the modified maximum deflection of the buckle from Eq. 3.23 and 3.25 become

$$\delta^* = \gamma_\delta \frac{4b}{\pi} \sqrt{\varepsilon_c^* - \varepsilon_i} \tag{3.32}$$

and

$$\delta^* = \gamma_\delta h \sqrt{\frac{4}{3}\left(\frac{\varepsilon_i}{\varepsilon_c^*} - 1\right)}, \tag{3.33}$$

respectively.

3.1.4 Effect of Film Sliding on Maximum Deflection

The buckling-induced sliding phenomenon can be described as the gliding and shearing of the film at the film/substrate interface from the adherent part (flat part) to the buckled part without further expansion of the delaminated zone. In his thesis, A. Ruffini reported through the means of molecular static simulations, the sliding phenomenon of Cu thin film on W substrate at the edges of buckle which was interpreted as the glide of misfit dislocations. He then proposed a modified expression of the FvK equations which takes into consideration the effect of buckling-induced sliding on the maximum deflection [116]. Supplemental displacements of film, Δ_{-b} and Δ_{+b} along the (O_x) direction in the mid-plane of the film at $x = -b$ and $x = +b$ respectively, have to be taken into account, as shown in Fig. 3.5.

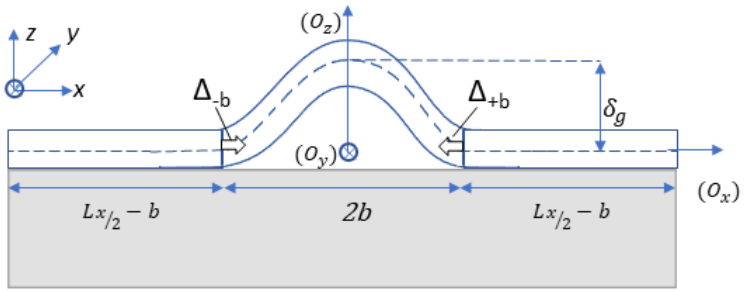

Figure 3.5: Schematic diagram of a film-substrate system in buckled configuration when the sliding mechanism is taken into account. Adapted from [116].

The boundary conditions are thus considered to be:

$$u_s(\pm b) = \mp\Delta, \tag{3.34}$$

$$w_s(\pm b) = \left.\frac{\partial w_s(x)}{\partial x}\right|_{x=\pm b} = 0, \tag{3.35}$$

where $\Delta = \frac{\Delta_{-b}-\Delta_{+b}}{2}$ is a positive value which accounts for the sliding of the flat part of the film located at the tip of the crack in the median plane shown in Fig. 3.5.

The procedure for solving the FvK equations is similar to that which is presented in section 3.1 when describing the embedded straight-sided buckle, also known as the Euler's column, and therefore, not repeated here. When the SSB is no longer embedded and the buckling-induced sliding is considered, the equations which describe the equilibrium of the film can be written as:

$$w_s(x) = \frac{\delta_s}{2}\left(1 + cos\left[\frac{\pi x}{b}\right]\right), \tag{3.36}$$

$$u_s(x) = \frac{\pi\delta_s^2}{32b} sin\left[\frac{2\pi x}{b}\right] - \frac{\Delta}{b}x, \tag{3.37}$$

$$\delta_s = \frac{4b}{\pi}\sqrt{\varepsilon_c - \varepsilon_i + \frac{\Delta}{b}}, \tag{3.38}$$

where δ_s corresponds to the modified maximum deflection predicted by FvK when sliding is considered in the flat part of the film. The sliding effect results in an additional strain in the FvK equations. Quantitatively, these expressions are valid as long as h/b is much less than 1 and δ_s is lower than $b/3$ [113].

Having discussed the elastic theory of thin plates under compression, experimental data from MoS_2 are subsequently analysed in the framework of this theory. For the purpose of this study, we have opted to take all compressive strains and stresses as positive in the following, instead of the negative convention.

3.2 Extraction of MoS_2 Young's Modulus from Buckle Morphology

The morphology of the buckling structures of the film and coatings provides interesting information about the mechanical properties of the film/substrate system. By experimental and numerical studies of buckle morphologies, properties like adhesion of the film to the substrate [117,118] and the Young's moduli of the system [119] have been successfully extracted. While many reports in the literature are based on strain-induced wrinkle measurements where the coated films stay bonded to the substrates, R. Boijoux *et al.* [120] have demonstrated a method to extract the elastic modulus mismatch in a film/substrate system by buckle morphology measurements where there is delamination of the film from the substrate but remain clamped at the buckle edges. This method takes into consideration the presence of the buckle depression (sinking of the film into the substrate at the base of the buckle structure; see Fig. 3.3) observed in cases where there is a high elastic contrast between the film and the substrate. In this section, we thus attempt to extract the Young's modulus of the 2D material (E_f) by taking the advantage of small depressions experimentally observed at the base of the buckles.

Consider a film with thickness h on a soft substrate under compressive strain. The emerging buckle has a deflection δ_1, depression δ_2 on both sides and width $2b$ (Mexican-hat profile). We observed that the depression δ_2 is a small percentage of the maximum deflection δ_1 of the buckle, typical in the case of hard films on soft substrates [121]. A profile obtained from AFM image of a 3L MoS_2 film characteristic of the film buckles is shown in Fig. 3.6.

A non-dimensional parameter B has been proposed by Zhang *et. al.* [122] which describes the morphological features of the Mexican-hat profile and the elastic properties of the film/substrate system, represented by α. B is given as:

$$B = 1.2\left(\frac{b}{h}\right)\left(\frac{1-\alpha}{1+\alpha}\right)^{\frac{1}{3}}, \tag{3.39}$$

with α being the Dundurs' coefficient, already defined in Eq. 3.29. The evolution of δ_2/δ_1 obtained from experiments, simulations and analytical modelling follows a curve when plotted as a function of B, shown in Fig. 3.7.

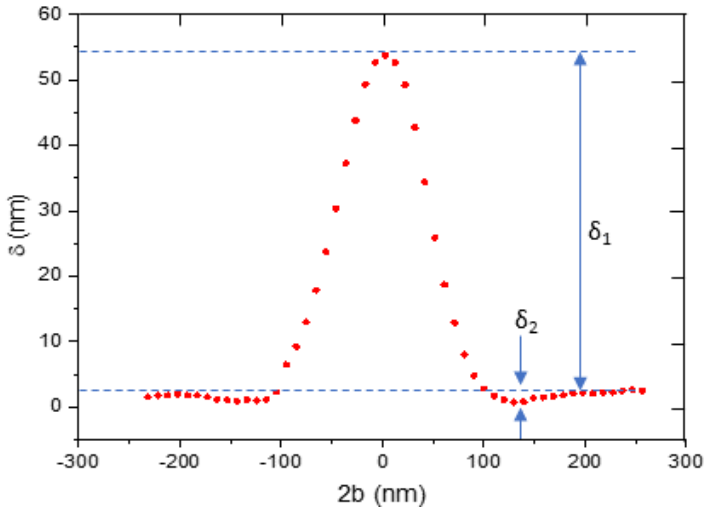

Figure 3.6: Characteristic profile of a buckle of 3L MoS_2 on PEEK substrate. δ_1 corresponds to the maximum buckle deflection, δ_2 to the depression at the buckle edges.

Low values of B correspond to hard film on soft substrate where depression δ_2 is easily observed. On the other hand, as B increases, δ_2 tends to zero. Using FEM analysis, a line of best fit (indicated by dashed blue line) has been determined which gives the relationship between B and δ_2/δ_1. The equation of the fit is given by [120]:

$$\frac{\delta_2}{\delta_1} = 0.178B^{-1.52} \tag{3.40}$$

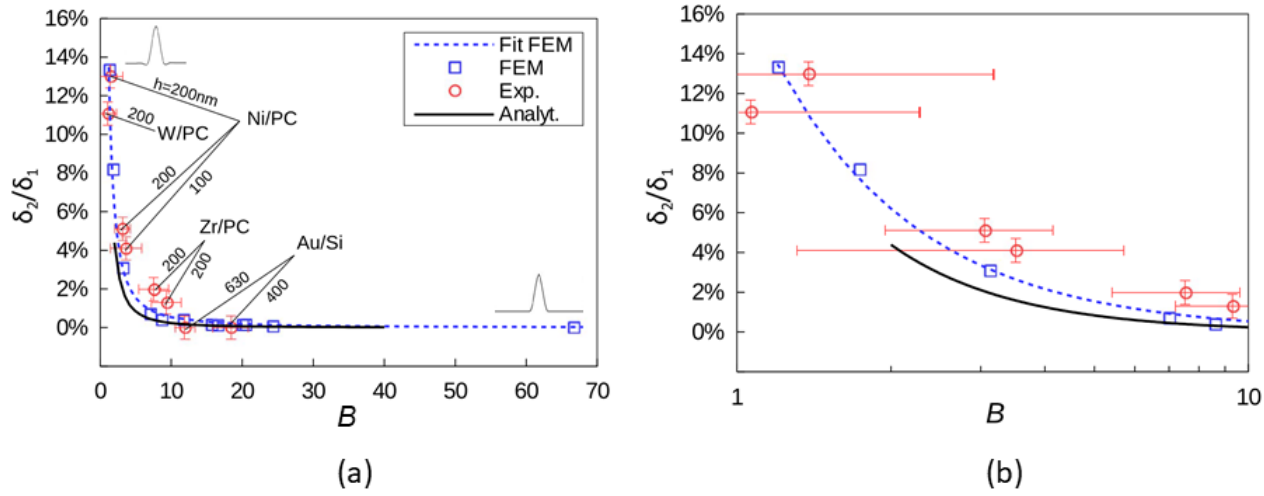

Figure 3.7: δ_2/δ_1 against B derived from FEM simulation, experimental data (with error bars) and analytical modelling (represented with black curve). (a) Linear scale overview. (b) Logarithmic scale zoom on the non-linear area ($0 < B < 10$). Adapted from [120].

By combining Eqs. 3.39 and 3.40, α is determined as a function of non-dimensional parameter λ:

$$\alpha = \frac{\lambda^3 - 1}{\lambda^3 + 1}, \tag{3.41}$$

where λ is defined as:

$$\lambda = 3.75 \left(\frac{b}{h}\right) \left(\frac{\delta_2}{\delta_1}\right)^{\frac{2}{3}}. \tag{3.42}$$

As b, h, δ_1 and δ_2 are accessible from a SSB profile (as the one shown Fig. 3.6), it is possible to extract λ directly from AFM experimental results. Therefore, it is possible to determine the elastic mismatch value α of a film/substrate.

Several buckles were analysed for 3L MoS_2 films on PEEK with observed $\delta_2/\delta_1 = 1.6 \pm 0.2\%$ to determine the non-dimensional parameter λ using Eq. 3.42, and subsequently, the Dundurs' coefficient α using Eq. 3.41. This gives the system elastic mismatch value $\alpha \approx 0.97$. The α value indicates a high contrast between the film's Young's modulus and the substrate's modulus. With the obtained α value, the film's Young's modulus E_f can thus be determined by inserting known parameters into equations (substrate's Young's modulus E_s given as 4 GPa, substrate's Poisson's ratio v_s given as 0.38 (both according to the data sheet from the manufacturer) and MoS_2 Poisson's ratio v_f given as 0.25 [123]). For various buckles of the 3L MoS_2, E_f is estimated to be 290 ± 10 GPa. It is to be noted that only buckles of 3L MoS_2 were evaluated as very small δ_2 values for 1L MoS_2 buckles (which is expected to be in the order of 10s of pm) is difficult to resolve considering the surface roughness of the substrate and the vertical resolution of the AFM which is only around 0.1 nm. The obtained E_f value is in good agreement when compared with the values extracted from other experimental techniques in the literature, but slightly higher than those extracted from numerical analyses as shown in Table 3.1.

Table 3.1: Comparison of MoS_2 Young's modulus determined by buckle morphology with previous experimental and theoretical studies.

Method	Number of layers	Young's modulus (GPa)	Reference
Buckle morphology	**Few layers**	290 ± 10	**Present work**
Nanoindentation	Few layers	270 ± 100	[124]
Laser Interferometry	Few layer	305 ± 10	[125]
Nanoindentation	Few layers	300 ± 70	[126]
First-principle molecular dynamics	Single layer	262	[127]
Lattice dynamics calculation of dispersion curves	Bulk	240	[128]
Stillinger-Weber based molecular dynamics at 300 K	Single layer	120	[129]
REBO based molecular dynamics at 10 K	Single layer	232	[130]
First-principle density functional theory calculations	Single layer	221 ± 2	[131]
First-principle density functional theory calculations	Single layer	240	[132]
ReaxFF based molecular dynamics at 300 K	Single layers	245 ± 15	[133]

3.3 Strain in 2D MoS_2 Films

Thin films deposited on substrates have been observed to undergo some form of deformation even without any externally applied stress. This is largely due to internal stresses in the film caused, for instance, by a mismatch in the thermal expansion coefficients of the film/substrate system [134]. In the case of our MoS_2 transferred to PEEK, internal stress in the film may be imposed by the intense vibration induced by ultrasonication during the transfer process. A number of techniques

have been described and employed in the past to quantify internal strain in thin films, the simpler one being the Stoney curvature method [135]. Another technique is the Raman spectroscopy which has been adopted to characterise the strain in graphene film [136]. However, due to the unavailability of a suitable Raman spectrometer, we have employed the buckling phenomenon to estimate the internal strain in the film.

3.3.1 Total Strain in MoS_2 Film

The total strain of our buckled film is a summation of the internal strain in the film and the transferred strain from the external stress applied to the substrate which is then imposed on the film. It is important to examine the efficiency of stress/strain transferred from the substrate to the film. Strain transfer efficiency from substrates to 2D materials has been found to depend highly on the Young's modulus of the film-substrate system. As reported by Liu *et. al.*, experimental data from strain-dependent photoluminescence spectroscopy and DFT calculations show that only about 10% strain is transferred from PDMS (Young's modulus of 1.5 MPa) to 1L MoS_2. On the other hand, experimental data and further calculations show that interfacial stress/strain transfer efficiency increases to up to 90% for substrates with modulus greater than 1 GPa [137]. Although this was reported for tensile strain transfer, for the purpose of this work, we assume a similar trend for compressive strain transfer. In a related study of strain mapping of strained MoS_2 films, the strain distribution of a few layers of MoS_2 was found to be similar to that of 1L MoS_2 [138]. We can therefore assume that since the Young's modulus of PEEK is given as 4 GPa, all the applied strain is transferred to the film and the strain distribution is similar for both samples.

Therefore, the total strain in the film ε_f can thus be given as:

$$\varepsilon_f = \varepsilon_o + \varepsilon_{s,a}, \tag{3.43}$$

where ε_o is the internal strain and $\varepsilon_{s,a}$ is the externally applied strain on the substrate.

3.3.2 Internal Strain in MoS_2 Film

We recall that buckles were observed on the sample surfaces after the complete removal of external strains. These residual buckles are an indication of the internal strain ε_0 present in the film. To

determine ε_0, we have employed equations describing the Euler's column where the substrate compliance is considered.

We recall Eqs. 3.31 and 3.33:

$$\varepsilon_c^* = \gamma_\varepsilon \frac{\pi^2}{12} \left(\frac{h}{b}\right)^2,$$

and

$$\delta^* = \gamma_\delta h \sqrt{\frac{4}{3}\left(\frac{\varepsilon_f}{\varepsilon_c^*} - 1\right)}.$$

By combining the two equations, we obtain:

$$\delta^{*2} = \left(\frac{16.\gamma_\delta^2.\varepsilon_f}{\pi^2.\gamma_\varepsilon}\right) b^2 - \left(\frac{4.\gamma_\delta^2}{3}\right) h^2 \tag{3.44}$$

Having determined the elasticity mismatch value of the system α, we can hence extract the substrate compliance parameters from the curves in Fig. 3.4. Extracted values of γ_ε and γ_δ are given as 0.76 and 1.75, respectively. By incorporating these values in Eq. 3.44, we obtain:

$$\delta^{*2} = 6.53\varepsilon_f b^2 - 4.08h^2 \tag{3.45}$$

Eq. 3.45 can be considered as a linear equation of square of buckle deflection δ^{*2} against the square of buckle width b^2, where the gradient is a function of the total strain in the film ε_f, the intercept being a function of the film thickness h.

Data obtained from numerous residual buckles from 1L MoS_2 (when $\varepsilon_{s,a} = 0$) are plotted and shown in Fig. 3.8. As expected, there is a linear relationship between δ^{*2} and b^2. A line of best fit is determined; the equation is inserted in the graph (with the linear regression $R^2 = 0.83$). The slope of the fit implies that the residual strain in the film is approximately $\varepsilon_o = 0.77\%$ and the intercept also estimates the film thickness to be approximately 1 nm.

With our assumption of a complete strain transfer from the substrate to the film, we can then conclude that the total strain in the film is greater than the applied strain in the substrate by 0.77%.

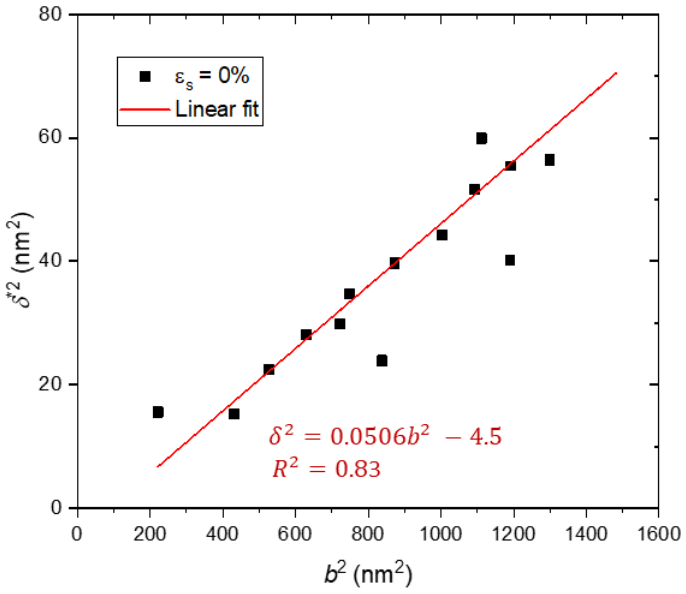

Figure 3.8: Square of maximum buckle deflection (δ^2) versus square of buckle width (b^2) of 1L MoS_2 on PEEK after a complete removal of the externally applied strain ($\varepsilon_s = 0\%$). Equation of the linear fit is inserted in the graph.

3.4 Analyses of MoS_2 Buckle Evolution

3.4.1 Predicted Critical Buckling Strain Versus Observed Critical Buckling Strain

We have observed from the AFM results that the critical buckling strain ε_c^{exp} for both 1L and 3L MoS_2 lies between 3% and 4% strain of the compressed substrate. However, if we consider values predicted by Eq. 3.21 which expresses the critical strain as a function of film thickness and buckle width, ε_c for 1L MoS_2 is calculated[2] as 0.0015 (or 0.15%). Similarly, predicted ε_c for 3L MoS_2 is calculated as 0.0041 (or 0.41%). If we further consider the effect of substrate compliance on the critical strain given in Eq. 3.31, the value of ε_c^* is calculated as 0.1% in 1L MoS_2 and 0.4% in 3L MoS_2. The huge discrepancy between the expected and observed values is thus a subject of interest which we seek to understand.

A major cause of the discrepancy between the theory and experiment arises from the fact that the theory does not put into consideration the adhesion of the film to the substrate. Before buckling occurs, sufficient energy is required to delaminate the bonded film. By compressing the

[2]The film thickness h is taken as 1 nm and the buckle width $2b$ value is taken as the width measured when the buckle was first observed at 4% strain.

sample, the internal elastic energy stored in the film is increased and when sufficient enough, it compensates for the adhesion energy at the interface which consequently causes the film to delaminate in certain regions on the surface. Once delamination occurs, the non-adherent parts can then be considered as thin plates whose behaviour has been predicted by the Euler's column. For the film to buckle, the strain is increased to a new value which is greater than the theoretical critical strain ($\varepsilon_c^{exp} > \varepsilon_c$). The difference between the two strains (or stresses) have been found to be directly related to the adhesion of the film/substrate system [42].

The evolution of the maximum deflection δ of buckles of compressed 1L and 3L MoS_2 films on PEEK is shown in Fig. 3.9. Experimental values of δ during the first loading of the samples are plotted as a function of the film strain. Predicted values of δ according to FvK equations (see Eqs. 3.31 and 3.32) are plotted as well. The difference between ε_c^{exp} and ε_c is extracted for both samples and will be useful in the determination of the adhesion energy.

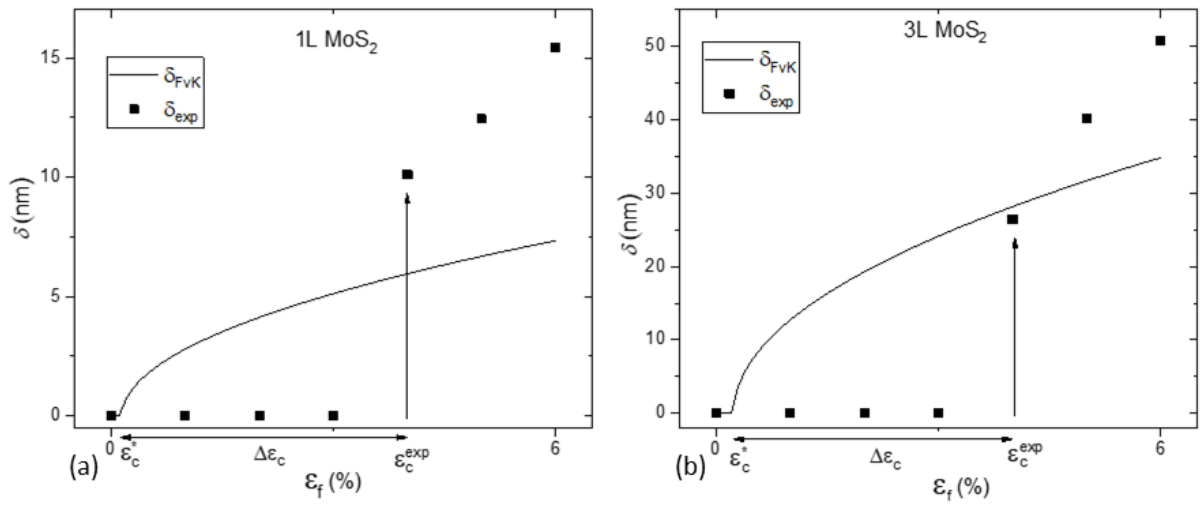

Figure 3.9: Evolution of maximum deflection obtained from experiment (δ_{exp}) and from FvK equations (δ_{FvK}) of a buckle of (a) 1L MoS_2, and (b) 3L MoS_2 on PEEK as a function of the film strain ε_f

3.4.2 Determination of Interfacial Adhesion Energy

As previously discussed, buckling occurs to release the build-up of elastic energy in the film induced by stress/strain. The total energy W_0 of the still-bonded film to the substrate over a

length $2b$ in a planar state is given as:

$$W_0 = \frac{h}{2}\left(\frac{1-v_f^2}{E_f}\right)2b\sigma^2, \tag{3.46}$$

where h is the film's thickness, v is the Poisson's ratio, E_f is the Young's modulus of the film and σ is the applied stress on the film. After delamination and buckling, the energy W_R of the now relaxed (buckled) film can be written in terms of strain and is given as:

$$W_R = W_0 - hb\frac{E_f}{1-v^2}(\varepsilon_c^{exp} - \varepsilon_c)^2, \tag{3.47}$$

where ε_c^{exp} is the experimental buckling strain and ε_c is the theoretical buckling strain determined by the delaminated length $2b$ and film's thickness. The condition for the delamination and buckling of a thin film is described [42] and given as:

$$W_0 \geq W_R + 2b\Gamma, \tag{3.48}$$

where Γ is the adhesion energy of the film to the substrate. By inserting Eqs. 3.46 and 3.47 in Eq. 3.48, we obtain:

$$2b\Gamma = hb\frac{E_f}{1-v^2}\left(\frac{1-v^2}{E_f}\sigma - \varepsilon_c\right)^2. \tag{3.49}$$

But,

$$\frac{1-v^2}{E_f}\sigma = \varepsilon_c^{exp}, \tag{3.50}$$

and

$$\frac{E_f}{1-v^2} = \bar{E}_f. \tag{3.51}$$

Therefore, Eq. 3.49 becomes:

$$\Gamma = \frac{1}{2}h\bar{E}_f(\varepsilon_c^{exp} - \varepsilon_c)^2. \tag{3.52}$$

ε_c^{exp} - ε_c is the difference between the experimental and theoretical buckling strains $\Delta\,\varepsilon_c$ (indicated in Fig. 3.9). Eq. 3.52 then becomes:

$$\Gamma = \frac{1}{2}h\bar{E}_f\Delta\varepsilon_c^2. \tag{3.53}$$

Eq. 3.53 makes it possible to estimate the adhesion energy from the physical and elastic properties of the film. Using the elastic modulus of MoS_2 previously determined in section 3.2, and the film thickness discussed in Chapter 1, the adhesion energy Γ of 1L MoS_2 is estimated to be 0.2 ± 0.1 N/m and Γ of 3L MoS_2 is estimated to be 0.9 ± 0.6 N/m. This indicates a higher adhesion energy of the 3L MoS_2 compared to the 1L film. The order of these values is in the same order of magnitude of the adhesion energy of 3 N/m reported for 3L graphene on silicon carbide [139].

3.4.3 MoS_2 Buckle Evolution

Experimental values of maximum deflection (δ_{exp}) and half the buckle width (b) extracted from buckles of 3L and 1L MoS_2 films previously shown in 2.17 (cf. page 62) are reported as a function of film strain ε_f and shown in Fig. 3.10. Data shown here are from the reloading (second loading) cycle, which have been taken to represent the buckle evolution. The first compression cycles have not been included in this data because delamination occurred during the first compression cycle and system stability was achieved afterwards.

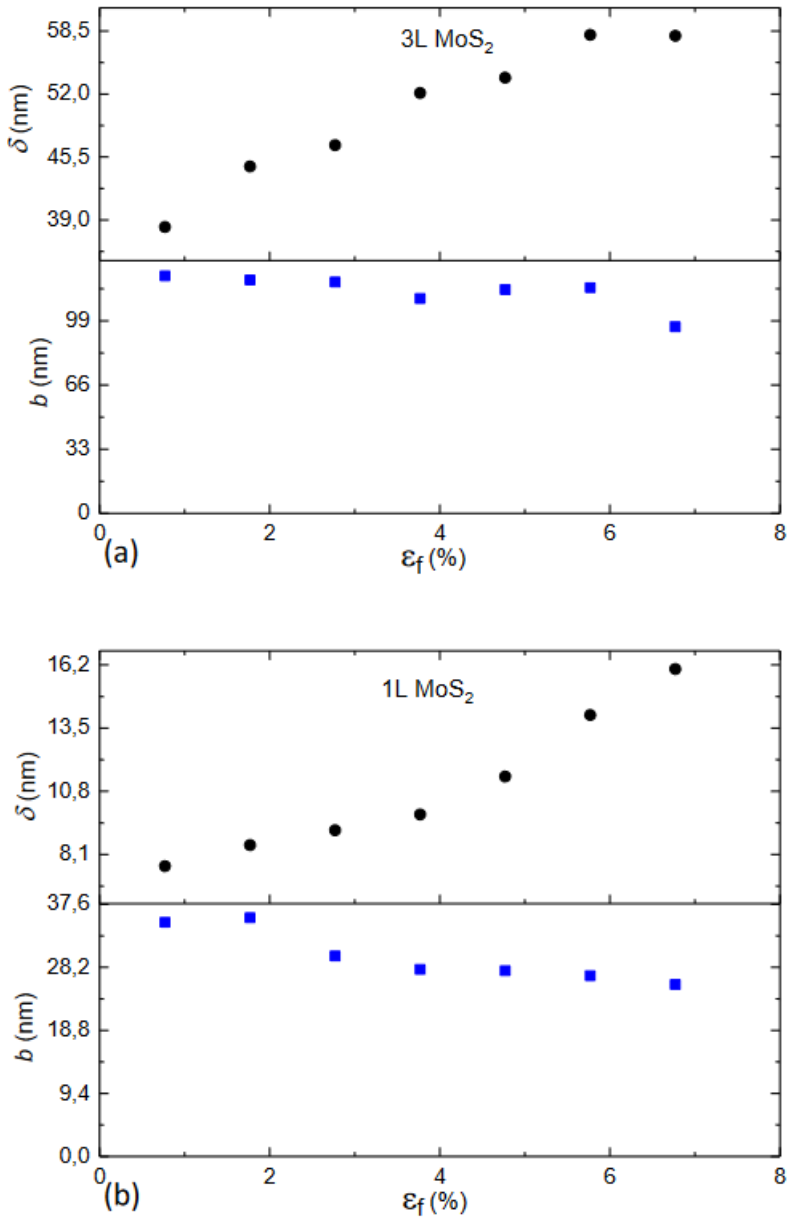

Figure 3.10: Evolution of the maximum deflection δ and half width of the buckle b of (a) 3L MoS_2 film, and (b) 1L MoS_2 film, as a function of film strain ε_f.

In both samples, deflection δ increases as ε_f is increased. In the 3L MoS_2 sample (Fig. 3.10a), b is approximately constant before an obvious reduction as ε_f tends to 6.77%. A steeper decrease of about 30% in b is observed in the 1L MoS_2 buckle (Fig. 3.10b) as ε_f is increased to 6.77%. This set of data is compared to the predicted deflection according to the FvK model where the elasticity mismatch of the film/substrate is considered. The FvK equations describing the critical

buckling strain and the maximum deflection are thus recalled:

$$\varepsilon_c^* = \gamma_\varepsilon \frac{\pi^2}{12} \left(\frac{h}{b}\right)^2, \tag{3.54}$$

and

$$\delta^* = \gamma_\delta \frac{4b}{\pi} \sqrt{\varepsilon_i - \varepsilon_c^*}. \tag{3.55}$$

By rearranging Eq. 3.55, we obtain:

$$\left(\frac{\pi}{4\gamma_\delta}\right)^2 \left(\frac{\delta^*}{b}\right)^2 = \varepsilon_f - \varepsilon_c^*. \tag{3.56}$$

We recall that compressive strains are assumed to be positive.

The b parameter appears in both terms of Eq. 3.56 (since ε_c^* is a function of b). To calculate expected values of δ^*, we explored two approaches. The first approach is to assume that b is constant. In the case of 3L MoS_2 buckle, the predicted maximum deflection values δ^* were determined according to Eq. 3.55. The delaminated length $2b$ is taken as the measured buckled width when the buckle was first observed, *i.e.* at $\varepsilon_s = 4\%$ and kept constant for varying ε_f. Also, this b value is employed to determine the theoretical critical buckling strain ε_c^* according to Eq. 3.54.

The comparison of both experimental and theoretical data of 3L MoS_2 (in the assumption of constant b) is shown in Fig. 3.11. Values of the square of normalised buckle deflection over buckle width $(\delta/b)^2$ are reported as a function of the film strain ε_f. The graph shows that, for every ε_f value, $(\delta/b)^2$ obtained from experiment is higher than the predicted $(\delta^*/b)^2$ value. In order to understand the difference in the experimental and theoretical values, we recall that δ is a function of the buckle width b and the square root of the film strain (Eq. 3.32). As no increase in b is considered, the increase in δ only translates to an increase in the overall strain in the film. The difference strain in the theoretical and experimental buckle, labelled $\Delta\varepsilon$, has therefore been determined for each ε_f step.

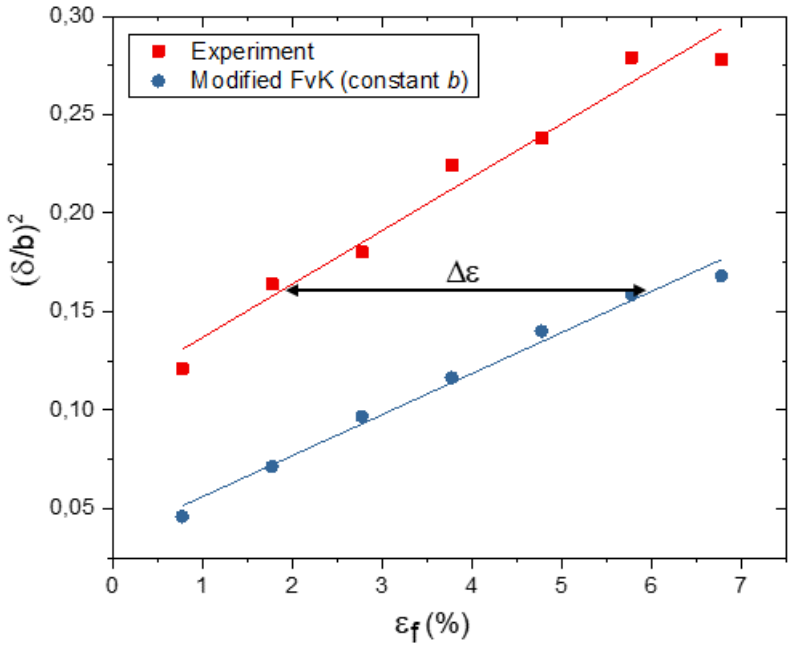

Figure 3.11: Evolution of $(\delta/b)^2$ vs ε_f of a 3L MoS_2 buckle compared with predicted $(\delta^*/b)^2$ values where b is assumed to be constant for the theoretical data.

Mathematically, $\Delta\varepsilon$ is an additional strain required to achieve the deflection observed experimentally (δ_{exp}). This displacement of the film, Δ, has been found to be an incremental push of the film from the flat zone into the buckle structure which can be physically described as sliding/shearing of the film over the substrate. Already described by A. Ruffini, $\Delta\varepsilon$ is expressed as the ratio of Δ to b [116] , *i.e.*

$$\Delta\varepsilon = \frac{\Delta}{b}. \tag{3.57}$$

$\Delta\varepsilon$ has been extracted for different ε_f values and the corresponding Δ values have been determined. Fig. 3.12 shows a plot of Δ with respect to the applied strain on the substrate $\varepsilon_{s,a}$ which is subsequently transferred to the film. A gradual linear increase in Δ is observed as ε_f is increased.

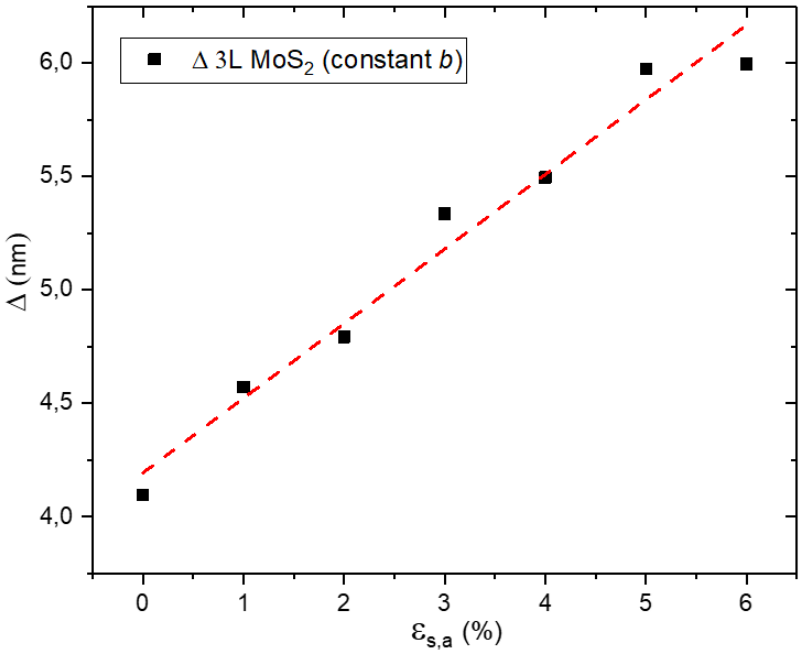

Figure 3.12: Displacement Δ of 3L MoS_2 film on PEEK substrate induced by sliding/shearing which is imposed by substrate compression.

In the second approach for the determination of predicted maximum deflection δ^*, we consider the real effect of b, even if its evolution is minimal. Here, δ^* values are calculated using the experimental value of b observed at each strain step (even if it is roughly constant). We also assume the theoretical critical strain is negligible that, since $\varepsilon_f \gg \varepsilon_c^*$ (we recall that $\varepsilon_c^* = 0.4\%$; see page 89), hence $\varepsilon_f - \varepsilon_c \approx \varepsilon_f$. Therefore, Eq. 3.56 becomes:

$$\delta^* = \gamma_\delta \frac{4b}{\pi} \sqrt{\varepsilon_f}. \tag{3.58}$$

By rearranging Eq. 3.58, we obtain:

$$\left(\frac{\pi}{4\gamma_\delta}\right)^2 \left(\frac{\delta^*}{b}\right)^2 = \varepsilon_f. \tag{3.59}$$

Since the term $\left(\frac{\pi}{4\gamma_\delta}\right)^2$ is constant, therefore any change in $\left(\frac{\delta^*}{b}\right)^2$ is directly linked to ε_f. Similar to the first scenario where b was considered constant, $\Delta\varepsilon$ is extracted from Fig. 3.13a for every strain step and Δ values are subsequently calculated using the observed b value for each ε_f value. A plot of Δ as a function of the applied strain $\varepsilon_{s,a}$ is shown in Fig. 3.13b. A linear increase in Δ

is also observed as $\varepsilon_{s,a}$ is increased. The magnitude of Δ is lower when compared with the first assumption, where b is assumed to be constant. The second approach seems to be more relevant to quantitatively estimate the sliding of the film.

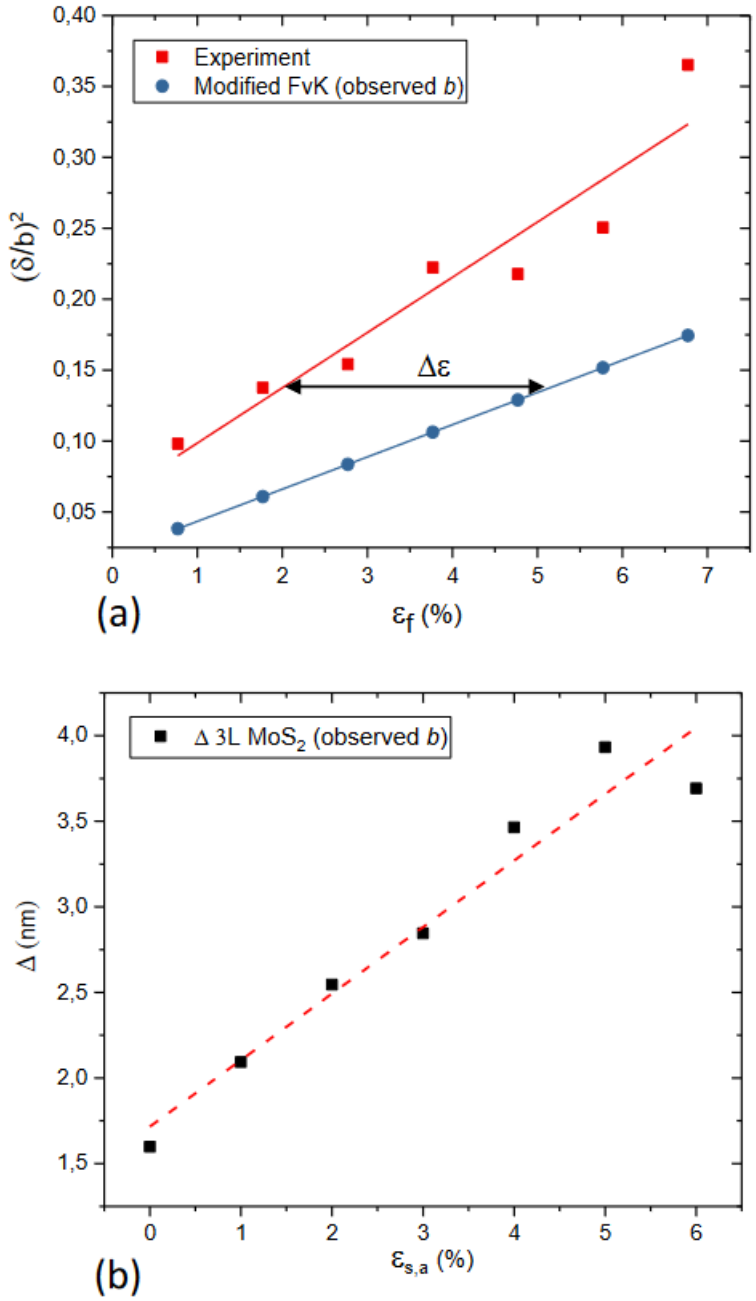

Figure 3.13: (a) Evolution of $(\delta/b)^2$ vs ε_f of a 3L MoS_2 buckle compared with predicted $(\delta^*/b)^2$ values where ε_c is negligible and observed b is adopted for δ^* calculation for every ε_f. (b) Displacement Δ of 3L MoS_2 film on PEEK substrate extracted from $\Delta\varepsilon$.

In the case of 1L MoS_2 buckle evolution (3.14), where the reduction in b is very evident as $\varepsilon_{s,a}$

is increased, experimental data is compared with predicted data by adopting the second strategy used in the analysis of the 3L MoS_2 buckle. For the calculation of δ^* values, ε_c^* is therefore negligible and b values are obtained from experimental data. Fig. 3.14a shows the plot of $(\delta/b)^2$ for both experimental and theoretical data versus total film strain ε_f. While the theoretical evolution of $(\delta^*/b)^2$ is linear, the evolution of the experimental $(\delta/b)^2$ appears not to be. Δ calculated from the extracted strain difference $\Delta\varepsilon$ is plotted against the applied substrate strain $\varepsilon_{s,a}$ (Fig. 3.14b). The film displacement over substrate Δ appears to be non-noticeable up until $\varepsilon_{s,a} = 3\%$ after which Δ is greatly increased. More data points will be needed to ascertain if the Δ tendency is exponential with respect to $\varepsilon_{s,a}$ or if it is constant up to $\varepsilon_{s,a} = 3\%$ before a linear augmentation to $\varepsilon_{s,a} = 6\%$.

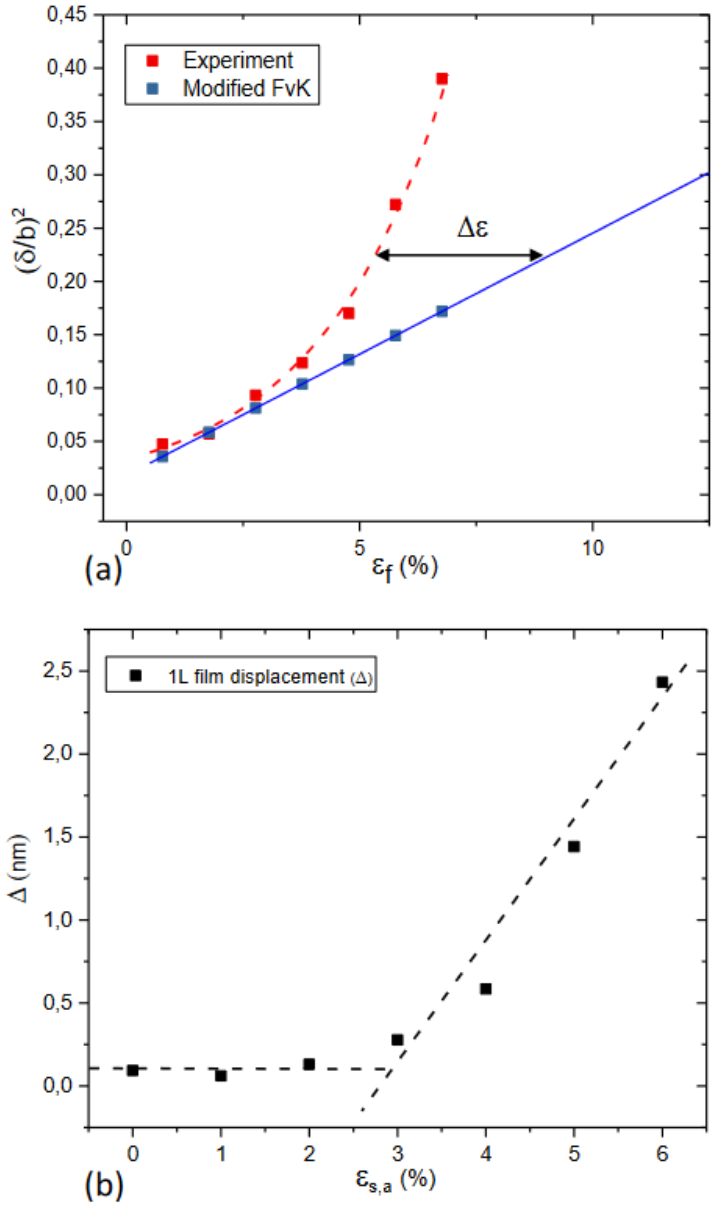

Figure 3.14: (a) Evolution of $(\delta/b)^2$ vs ε_f of a 1L MoS_2 buckle compared with predicted $(\delta^*/b)^2$ values where ε_c is negligible and observed b is adopted for δ^* calculation for every ε_f. (b) Displacement Δ of 1L MoS_2 film on PEEK substrate extracted from $\Delta\varepsilon$.

In both 3L and 1L Mos_2 films on PEEK substrates, Δ is increased without any further increase in the delamination of the film (b) from the substrate for each strain increase (due to externally applied compression on substrate). As expected by non-linear shear-lag model, which describes the interfacial sliding of films when the interfacial shear stress exceeds a critical value [140], a critical strain is reached after which sliding is activated in the flat part of the film, which leads to Δ at the boundary of the flat part of the film. While the Δ is linear in the 3L film, it appears to

be delayed in the 1L film until $\varepsilon_{s,a} = 3\%$.

It is highly probable that the sliding phenomenon causes the "re-organisation" of the film during coalescence of SSBs over a long distance where a change in direction is observed. It may also be responsible for other unexpected observations reported in Chapter 2. These include: the increase in the inter-buckle distance d as strain is increased, the re-adhesion of the film at the edges of the buckle consequently leading to a decrease in b as ε_s is increased. Perhaps, further analytical and experimental studies are required to understand this mechanical behaviour.

3.5 Summary

In this third Chapter, we started by describing the elastic theory of thin plates for which extracted data from AFM results were analysed. In the second section, we were able to extract the Young's modulus of buckled MoS_2 film by taking the advantage of depressions at the edges of the buckles. With a ratio of depression to deflection (δ_2/δ_1) being $\approx 1.6\%$, the film's Young's modulus E_f is estimated to be 290 ± 10 GPa. This value is in good agreement with values reported from other experimental methods and slightly higher when compared to values from numerical analyses. It is also important to state that this is a non-destructive method to extract E_f as opposed to the nanoindentation technique reported in the literature. We can therefore confirm that buckle morphology is effective in the determination of the elasticity property of 2D films.

In the third section, we discussed the extraction of actual strain in the film using equations describing straight-sided buckles. Residual buckles were observed after a complete withdraw of the externally applied strain which were helpful in determination of the internal strain in the film. In the fourth section, we considered the observed critical buckling strain and compared with the predicted critical buckling strain. The difference is linked to the adhesion of the films to the substrates. We also studied the evolution of MoS_2 buckle under cyclic loading and unloading. The deflection evolution follows a similar trend as that predicted by the FvK theory although an increase in experimental values is observed when compared with the predicted value despite considering the influence of substrate compliance in the FvK model. The difference between the experimental and predicted values has been linked to film displacement due to sliding/shearing at the film/substrate interface. This interfacial displacement was quantified and found to increase as

compression increases. In the 3L film, interfacial displacement was observed to increase linearly as the applied strain was increased. However, in the 1L film, displacement was not observed until applied strain was increased to about 3% after which a linear increase in the displacement was observed.

3.6 Résumé en Français

Le comportement élastique d'un matériau soumis à une contrainte mécanique est observé par des modifications de ses dimensions, étudiées dans le cadre de l'élasticité linéaire pour les déformations et reliées à la dérivée première des déplacements. Lorsque nous considérons des matériaux plus minces soumis à des contraintes, il y a un changement de leur forme en plus du changement de leurs dimensions. Il est donc nécessaire d'étudier la relation entre la contrainte mécanique (ou la déformation) et la réponse du matériau sous la forme d'un changement de forme. Le phénomène de flambage est donc analysé dans ce contexte. Dans ce chapitre, nous discutons d'un modèle bien établi qui décrit le phénomène de flambage dans les plaques soumises à la compression. Nous décrivons également une méthode d'extraction du module d'Young du film de MoS_2 à partir de la morphologie des flambages observés. Enfin, nous comparons nos résultats expérimentaux avec les données prédites par le modèle numérique.

I. Modèle décrivant les films minces sous contrainte

Les plaques minces (ou films minces) soumises à diverses conditions de chargement ont été étudiées dans le cadre du modèle de Föppl von Kármán (FvK). Cette théorie considère que la plaque est bidimensionnelle (comme le montre la Fig. 3.15) et qu'elle peut subir une déformation lorsqu'elle est soumise à une charge de compression (Fig. 3.15b) ; les modifications de ses dimensions sont liées aux dérivées premières des déplacements. Les équations mathématiques du modèle FvK décrivant l'équilibre mécanique d'une plaque comprimée ont été utilisées pour décrire la géométrie de la boucle droite (SSB) également appelée colonne d'Euler. La théorie de la colonne d'Euler fournit un cadre mathématique pour prédire la contrainte ou la déformation critique à laquelle le flambage se produit. Elle donne également la déviation maximale du flambage en fonction de l'épaisseur de la plaque et de sa contrainte/déformation. D'autres études ont montré que le phénomène de flambage peut être influencé par l'élasticité du substrat. En déterminant le décalage d'élasticité dans le système plaque/substrat (coefficient de Dundurs), un facteur de correction peut être extrait pour modifier le modèle FvK. Notre objectif est donc d'étudier si ces théories peuvent être étendues aux films 2D comme le MoS_2.

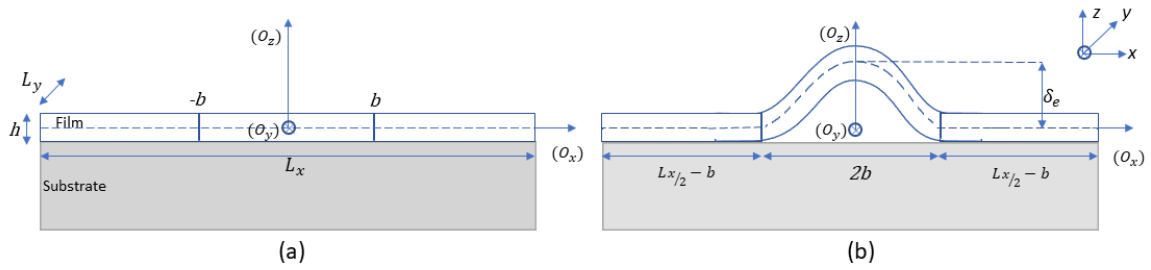

Figure 3.15: Schéma du système film-substrat (a) en configuration plate et (b) en configuration ridée.

II. Détermination du module d'Young d'un film de MoS_2

L'extraction du coefficient de Dundurs est essentielle pour la détermination du module d'Young. La morphologie des structures de flambage du film fournit des informations intéressantes sur les propriétés mécaniques du système film/substrat. R. Boujoux *et al.* ont publié une méthode permettant d'extraire le décalage du module élastique dans un système film/substrat par des mesures de la morphologie du flambage. Cette méthode prend en compte la présence d'une dépression de la ride (enfoncement du film dans le substrat à la base de la structure de ride) observée dans les cas où il existe un contraste élastique élevé entre le film et le substrat. Un profil type de ce phénomène appelé « Chapeau mexicain », obtenu à partir d'une image AFM d'un film de MoS_2 3L, est illustré Fig. 3.16. Considérons un film d'épaisseur h sur un substrat mou soumis à une contrainte de compression. La boucle émergente a une déflexion δ_1, une dépression δ_2 des deux côtés et une largeur $2b$ (profil en chapeau mexicain). Le coefficient de Dundurs α peut alors être déterminé comme une fonction non linéaire du paramètre λ tel que :

$$\alpha = \frac{\lambda^3 - 1}{\lambda^3 + 1}, \tag{3.60}$$

où λ est définit par :

$$\lambda = 3.75 \left(\frac{b}{h}\right) \left(\frac{\delta_2}{\delta_1}\right)^{\frac{2}{3}}. \tag{3.61}$$

Les données de plusieurs boucles analysées pour un film de MoS_2 3L sur PEEK permettent d'extraire un coefficient de Dundurs de 0,97, ce qui indique un contraste d'élasticité très élevé entre le film et le substrat.

Il est ainsi possible de déterminer un module d'Young E_s du film en utilisant la relation entre

ε_s et α donnée par :

$$\alpha = \frac{\bar{E_f} - \bar{E_s}}{\bar{E_f} + \bar{E_s}}, \tag{3.62}$$

Où $\bar{E_f}$ et $\bar{E_s}$ correspondent respectivement au module d'Young réduit du film et du substrat tels que :

$$\bar{E_i} = \frac{E_i}{1 - v_i^2}. \tag{3.63}$$

En considérant les valeurs des coefficients de Poisson v_i du film et du substrat données par la littérature, nous avons ainsi pu déterminer un module d'Young du film d'environ 290 GPa. Cette valeur est en bon accord avec les valeurs rapportées dans la littérature, comprises en grande majorité entre 200 et 400 GPa[3].

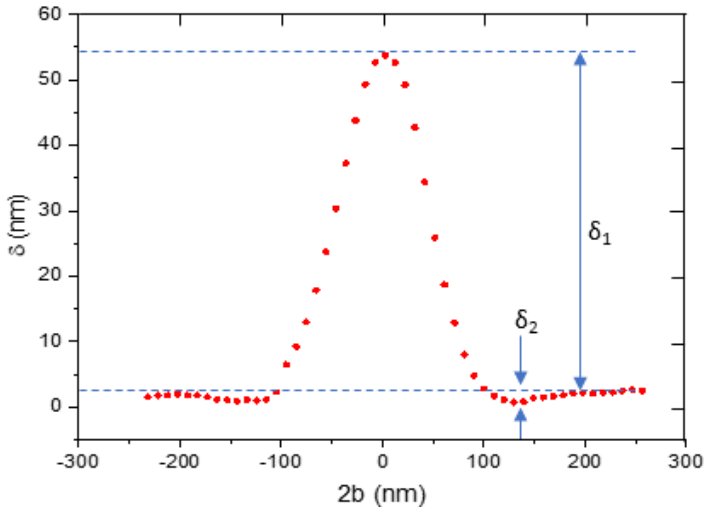

Figure 3.16: Profil caractéristique d'une ride de 3L MoS_2 sur substrat PEEK. δ_1 correspond à la déviation maximale du flambage, δ_2 à la dépression sur les bords du flambage.

III. Déformation résiduelle du film

Des études ont montré que les films minces déposés sur des substrats présentent une certaine déformation interne. Celle-ci est en grande partie induite par les contraintes internes causées par une inadéquation des coefficients d'expansion thermiques du système film/substrat. Dans le cas de notre MoS_2 transféré sur PEEK, la contrainte interne dans le film peut être imposée

[3]Cf ref [124] à [133]

par la vibration intense induite par les ultrasons pendant le processus de transfert. Par conséquent, la contrainte totale dans le film est la somme de la contrainte appliquée transférée par le substrat comprimé et de la contrainte interne dans le film. Il est donc nécessaire de déterminer la déformation interne. Nous rappelons que des flambages résiduels ont été observés après l'élimination complète de la contrainte appliquée extérieurement. Les morphologies de ces rides ont été utilisées pour déterminer la déformation dans le film lorsqu'aucune déformation externe n'est appliquée. Les résultats des données analysées montrent une déformation interne de 0,77% dans le MoS_2 1L. Nous avons supposé une valeur de déformation interne égale pour le film 3L MoS_2 puisqu'ils ont subi la même procédure de préparation de l'échantillon.

IV. Analyse de l'évolution de la morphologie des rides

Après avoir déterminé le module d'Young du film, nous avons comparé la déformation critique expérimentale pour le flambage avec celle prédite par le modèle FvK modifié. D'après nos résultats expérimentaux, le flambage s'est produit entre 3 et 4% de déformation appliquée dans les films de MoS_2 1L et 3L. Cependant, les calculs du modèle FvK modifié montrent que le flambage devrait se produire à 0,1% et 0,4% de déformation pour les films de MoS_2 1L et 3L, respectivement. L'une des principales causes de l'écart entre la théorie et l'expérience réside dans le fait que la théorie ne tient pas compte de l'adhésion du film au substrat. Avant que le flambage ne se produise, une énergie suffisante est nécessaire pour délaminer le film. En comprimant l'échantillon, l'énergie élastique interne stockée dans le film est augmentée et, lorsqu'elle est suffisante, elle compense l'énergie d'adhésion à l'interface, ce qui entraîne le décollement du film dans certaines régions de la surface. Une fois le délaminage effectué, les parties non adhérentes peuvent alors être considérées comme des plaques minces dont le comportement a été prédit par la colonne d'Euler. Nous avons donc extrait l'énergie d'adhésion du film à partir de la différence entre les déformations critiques de flambage expérimentales et théoriques. L'énergie d'adhésion estimée des films est de 0,15 N/m et 0,93 N/m pour les films de MoS_2 1L et 3L, respectivement.

Nous avons ensuite comparé l'évolution des rides extraite de nos données expérimentales avec les valeurs prédites par les équations FvK modifiées. L'évolution de la déviation maximale des rides des films MoS_2 1L et 3L suit une tendance similaire à celle prédite par le modèle théorique,

mais une augmentation des valeurs expérimentales a été observée. La différence entre les valeurs expérimentales et prédites a été liée au déplacement du film, en considérant une poussée incrémentale du film de la zone plate à la structure en boucle par glissement/cisaillement à l'interface entre le film et le substrat. Cela explique la réduction de la largeur de la boucle au fur et à mesure de l'augmentation de la déformation, signalée précédemment au Chapitre 2. Nous avons tenté de quantifier le déplacement Δ des films en fonction de la déformation appliquée. Pour un même b, il faut tout d'abord déterminer la déformation additionnelle $\Delta\ \varepsilon$ afin de retrouver la valeur calculée à partir de la valeur expérimentale, comme représenté Fig. 3.17. En multipliant $\Delta\ \varepsilon$ par la largeur $2b$ de la ride, il est ainsi possible de tracér le déplacement Δ en fonction de la contrainte appliquée au substrat. La Fig. 3.18 montre ainsi que pour un film de MoS_2 3L, le déplacement Δ a augmenté linéairement avec la déformation du film. En revanche, pour un film 1L, le déplacement n'a pas été observé avant que la déformation du film ne soit augmentée à 3%.

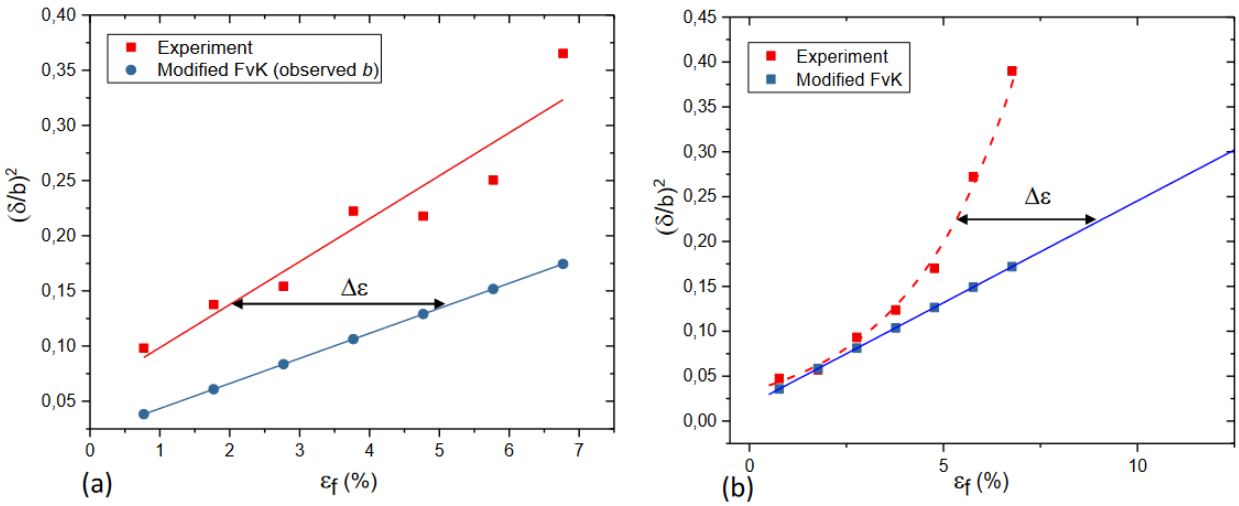

Figure 3.17: Evolution des rapports $(\delta/b)^2$ expérimentaux et calculés en fonction de la déformation du substrat ε_f pour une ride se formant sur un film de (a) 3L and (b) 1L MoS_2. Pour chaque ε_f, les valeurs calculées via le modèle FvK modifié considèrent ε_c négligeable et prennent en compte les valeurs de b expérimentales dans le calcul δ^*.

Enfin, il apparaît que, bien que la structure de flambage des films MoS_2 ultraminces soit similaire à celle des plaques métalliques épaisses, qui ont été étudiées et rapportées précédemment, les mécanismes diffèrent et il est nécessaire d'adapter les modèles existants. Aussi, les complexités engendrées par le déplacement du film sur le substrat, qui a été identifié comme responsable de la diminution de la largeur du flambage à mesure que la déformation augmente, nécessiteront

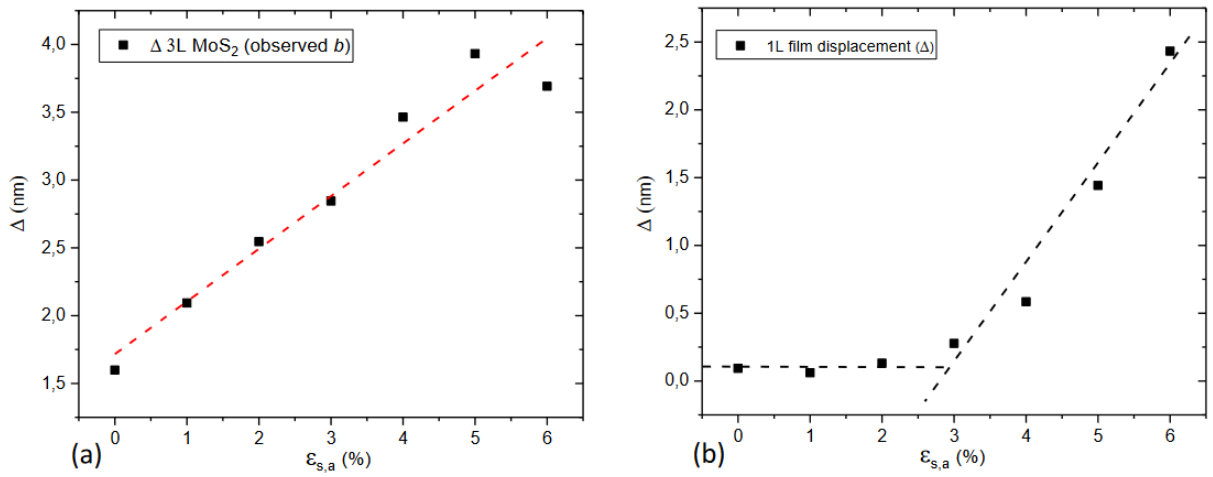

Figure 3.18: Déplacement Δ en fonction de la déformation appliquée au substrat ε_s,a pour un film de MoS_2 (c) 3L and (d) 1L déposé sur PEEK. Les valeurs de Δ sont extraites des valeurs de Δ ε présentées Fig. 3.17.

d'autres études numériques et expérimentales.

Conclusion and Perspectives

This thesis was devoted to studying the mechanical response of ultrathin MoS_2 films to compressive strain and determine if the buckling theory of thin plates can be extended to extremely thin 2D materials. Uniaxial compression tests were carried out in order to induce delamination and buckling of the films. The evolution of the film was observed by the means of atomic force microscopy with an integrated straining device which enabled *in-situ* compression and scanning. Experimental results were then analysed and compared to those predicted by the Föppl–von Kármán equations in the framework of elasticity.

Firstly, we described the procedures for the transfer of 2D films from a substrate to another. Transferring 2D films from the growth substrate to other substrates of interest is a major challenge. Targeted substrates were prepared and the procedure to ensure relatively flat surfaces have been enumerated. MoS_2 films were first transferred to prepared substrate using the PMMA-assisted transfer method proposed in the literature. Results from surface characterization showed the presence of residues of the sacrificial coating on the free surface. In order to prepare an impurity-free sample, we optimised a transfer method which guarantees a reliable, chemical and impurity-free transfer to any desired substrate while preserving the morphology and quality of the film for various physical analyses and applications. Using this method, MoS_2 films were transferred to metallic and non-metallic substrates. Results from sample characterisation by surface probe microscopy and Raman spectroscopy all indicate that the morphology of the transferred film was preserved.

The second chapter is dedicated to the description of the test procedure and experimental results of the response of the MoS_2 films to compressive strain. Poly-ether-ether-ketone was chosen as the substrate for this study due to some of its physical and mechanical properties. The substrate

was characterised to determine its elastic limit and was observed to remain in its elastic region up to 6% of compressive strain. Single layer and 3 layer MoS_2 films transferred to the substrates were progressively strained using a locally fabricated straining device which was incorporated to the atomic force microscope. Emergence of straight-sided buckles were observed on both 1L MoS_2 and 3L MoS_2 samples as compressive strain is increased from 3% to 4%. These buckles propagate perpendicularly to the direction of the compression axis and satisfy the conditions for the description of the Euler's column. Two buckles propagating in opposite directions were observed to interact depending on the relationship between the distance d between them and their width $2b$. If they were close enough, (at $\bar{d} < 2b$), the two buckles were observed to coalesce. These observations are similar to what has been reported in the case of thick metallic films. However, it was not possible to combine our data and existing model using buckle interactions to extract the Dundurs' coefficient and the Young modulus. Lastly, with increasing substrate strain, increase in the buckle deflection was observed as expected but decrease in the buckle width was observed, which is at variance to what is reported in the literature.

In the last chapter, buckle morphologies and evolution were analysed based on the modified FvK equations which take into consideration the elasticity of the substrate. By taking advantage of depressions observed at the edges of the buckles, the Young's modulus of MoS_2 was extracted to be 290 ± 10 GPa, which is good agreement with reported values in the literature. The internal strain in the film was determined from the analyses of residual buckles after the complete removal of externally imposed strain, by using the modified Föppl–von Kármán equations which take into consideration the elasticity mismatch in the film/substrate system. The adhesion energy of the film to the substrate was also extracted by considering the difference between experimental and predicted critical buckling strains according to the theoretical model. The experimental values of the maximum deflection of buckles of both 1L and 3L MoS_2 films were observed to be higher than the predicted values by the FvK equations with increasing strain. The difference in the experimental and predicted values have been linked to the displacement of film, which is an incremental push of the film from the flat zone to the buckle structure via sliding/shearing at the interface between the film and the substrate. In the 3L MoS_2 film, the displacement was found to increase linearly with the film strain. In the 1L film, the displacement was not clearly observed

until the film strain was increased to 3%.

Finally, it appears that the buckling mechanisms of ultra-thin MoS_2 films are only similar to those of thick metallic plates, which have been previously studied and reported. The complexities brought about by the displacement of the film over the substrate, which has been identified to be responsible for the decrease in the buckle width as strain is increased, will require further numerical and experimental studies. We have proposed the use of Finite Element Simulations with Cohesive Zone (CZ) model, which have been used in the past to study crack propagation at the film-substrate interface with strain increase, to study the delamination and re-adhesion of the film to the substrate. It is also necessary to confirm the exact internal strain in the film by Raman spectroscopy or other characterisation techniques. To enhance more accurate data acquisition, a new straining device has been acquired. The Deben microtest device, which is computer-controlled, would enable a gradual strain increase of about 0.1% per step. This would help in determining the precise experimental critical strain for compressed samples. Also with more data, the evolution of the buckle will be better studied. Likewise, it is important to measure the total strain in the film for every substrate strain increase. It is suggested that small flakes of the 2D material with known dimensions should be strained rather than continuous films. This would make it easier to track and measure fairly accurately the film's displacement over the substrate and also the film strain. This study could be extended to other 2D materials like graphene to confirm the buckle-driven film displacement.

Bibliography

[1] K. S. Novoselov, A. Geim, *et al.*, "The rise of graphene," *Nat. Mater*, vol. 6, no. 3, pp. 183–191, 2007.

[2] S. Iijima, "Helical microtubules of graphitic carbon," *nature*, vol. 354, no. 6348, pp. 56–58, 1991.

[3] S. Iijima, "Carbon nanotubes: past, present, and future," *Physica B: Condensed Matter*, vol. 323, no. 1-4, pp. 1–5, 2002.

[4] M. F. De Volder, S. H. Tawfick, R. H. Baughman, and A. J. Hart, "Carbon nanotubes: present and future commercial applications," *science*, vol. 339, no. 6119, pp. 535–539, 2013.

[5] M. J. Allen, V. C. Tung, and R. B. Kaner, "Honeycomb carbon: a review of graphene," *Chemical reviews*, vol. 110, no. 1, pp. 132–145, 2010.

[6] C. Soldano, A. Mahmood, and E. Dujardin, "Production, properties and potential of graphene," *Carbon*, vol. 48, no. 8, pp. 2127–2150, 2010.

[7] J.-W. Jiang, "Graphene versus MoS_2: A short review," *Frontiers of Physics*, vol. 10, no. 3, pp. 287–302, 2015.

[8] B. Radisavljevic, A. Radenovic, J. Brivio, V. Giacometti, and A. Kis, "Single-layer MoS_2 transistors," *Nature nanotechnology*, vol. 6, no. 3, pp. 147–150, 2011.

[9] A. Splendiani, L. Sun, Y. Zhang, T. Li, J. Kim, C.-Y. Chim, G. Galli, and F. Wang, "Emerging photoluminescence in monolayer MoS_2," *Nano letters*, vol. 10, no. 4, pp. 1271–1275, 2010.

[10] M. Chhowalla, H. S. Shin, G. Eda, L.-J. Li, K. P. Loh, and H. Zhang, "The chemistry of two-dimensional layered transition metal dichalcogenide nanosheets," *Nature chemistry*, vol. 5, no. 4, pp. 263–275, 2013.

[11] Z. Li and S. L. Wong, "Functionalization of 2D transition metal dichalcogenides for biomedical applications," *Materials Science and Engineering: C*, vol. 70, pp. 1095–1106, 2017.

[12] S. Manzeli, D. Ovchinnikov, D. Pasquier, O. V. Yazyev, and A. Kis, "2D transition metal dichalcogenides," *Nature Reviews Materials*, vol. 2, no. 8, pp. 1–15, 2017.

[13] R. G. Dickinson and L. Pauling, "The crystal structure of molybdenite," *Journal of the American Chemical Society*, vol. 45, no. 6, pp. 1466–1471, 1923.

[14] J. A. Wilson and A. Yoffe, "The transition metal dichalcogenides discussion and interpretation of the observed optical, electrical and structural properties," *Advances in Physics*, vol. 18, no. 73, pp. 193–335, 1969.

[15] R. Frindt and A. Yoffe, "Physical properties of layer structures: optical properties and photoconductivity of thin crystals of molybdenum disulphide," *Proceedings of the Royal Society of London. Series A. Mathematical and Physical Sciences*, vol. 273, no. 1352, pp. 69–83, 1963.

[16] P. Joensen, R. Frindt, and S. R. Morrison, "Single-layer MoS_2," *Materials research bulletin*, vol. 21, no. 4, pp. 457–461, 1986.

[17] R. Tenne, L. Margulis, M. e. Genut, and G. Hodes, "Polyhedral and cylindrical structures of tungsten disulphide," *Nature*, vol. 360, no. 6403, pp. 444–446, 1992.

[18] D. Lembke, S. Bertolazzi, and A. Kis, "Single-layer MoS_2 electronics," *Accounts of chemical research*, vol. 48, no. 1, pp. 100–110, 2015.

[19] D. Akinwande, N. Petrone, and J. Hone, "Two-dimensional flexible nanoelectronics," *Nature communications*, vol. 5, no. 1, pp. 1–12, 2014.

[20] H. E. Sliney, "Solid lubricant materials for high temperatures—a review," *Tribology International*, vol. 15, no. 5, pp. 303–315, 1982.

[21] Y.-C. Lin, D. O. Dumcenco, Y.-S. Huang, and K. Suenaga, "Atomic mechanism of the semiconducting-to-metallic phase transition in single-layered MoS_2," *Nature nanotechnology*, vol. 9, no. 5, pp. 391–396, 2014.

[22] J. P. Oviedo, S. KC, N. Lu, J. Wang, K. Cho, R. M. Wallace, and M. J. Kim, "In situ tem characterization of shear-stress-induced interlayer sliding in the cross section view of molybdenum disulfide," *ACS nano*, vol. 9, no. 2, pp. 1543–1551, 2015.

[23] X. Li and H. Zhu, "Two-dimensional MoS_2: Properties, preparation, and applications," *Journal of Materiomics*, vol. 1, no. 1, pp. 33–44, 2015.

[24] W. Zhao, J. Pan, Y. Fang, X. Che, D. Wang, K. Bu, and F. Huang, "Metastable MoS_2: crystal structure, electronic band structure, synthetic approach and intriguing physical properties," *Chemistry–A European Journal*, vol. 24, no. 60, pp. 15942–15954, 2018.

[25] Y. Venkata Subbaiah, K. Saji, and A. Tiwari, "Atomically thin MoS_2: a versatile nongraphene 2D material," *Advanced Functional Materials*, vol. 26, no. 13, pp. 2046–2069, 2016.

[26] S. Bertolazzi, J. Brivio, and A. Kis, "Stretching and breaking of ultrathin MoS_2," *ACS nano*, vol. 5, no. 12, pp. 9703–9709, 2011.

[27] C. Lee, X. Wei, J. W. Kysar, and J. Hone, "Measurement of the elastic properties and intrinsic strength of monolayer graphene," *science*, vol. 321, no. 5887, pp. 385–388, 2008.

[28] R. C. Cooper, C. Lee, C. A. Marianetti, X. Wei, J. Hone, and J. W. Kysar, "Nonlinear elastic behavior of two-dimensional molybdenum disulfide," *Physical Review B*, vol. 87, no. 3, p. 035423, 2013.

[29] P. Johari and V. B. Shenoy, "Tuning the electronic properties of semiconducting transition metal dichalcogenides by applying mechanical strains," *ACS nano*, vol. 6, no. 6, pp. 5449–5456, 2012.

[30] Q. Yue, J. Kang, Z. Shao, X. Zhang, S. Chang, G. Wang, S. Qin, and J. Li, "Mechanical and electronic properties of monolayer MoS_2 under elastic strain," *Physics Letters A*, vol. 376, no. 12-13, pp. 1166–1170, 2012.

[31] D. J. Trainer, Y. Zhang, F. Bobba, X. Xi, S.-W. Hla, and M. Iavarone, "The effects of atomic-scale strain relaxation on the electronic properties of monolayer MoS_2," *ACS nano*, vol. 13, no. 7, pp. 8284–8291, 2019.

[32] N. Harada, S. Sato, and N. Yokoyama, "Computational study on electrical properties of transition metal dichalcogenide field-effect transistors with strained channel," *Journal of Applied Physics*, vol. 115, no. 3, p. 034505, 2014.

[33] L. Dong, R. R. Namburu, T. P. O'Regan, M. Dubey, and A. M. Dongare, "Theoretical study on strain-induced variations in electronic properties of monolayer MoS_2," *Journal of Materials Science*, vol. 49, no. 19, pp. 6762–6771, 2014.

[34] S. Bhattacharyya, T. Pandey, and A. K. Singh, "Effect of strain on electronic and thermoelectric properties of few layers to bulk MoS_2," *Nanotechnology*, vol. 25, no. 46, p. 465701, 2014.

[35] H. Rostami, R. Roldán, E. Cappelluti, R. Asgari, and F. Guinea, "Theory of strain in single-layer transition metal dichalcogenides," *Physical Review B*, vol. 92, no. 19, p. 195402, 2015.

[36] N. Junqua and J. Grilhé, "Surface instabilities and dislocation formation during crystal growth," *Materials Science and Engineering: A*, vol. 173, no. 1-2, pp. 29–32, 1993.

[37] F. C. Frank and J. Van der Merwe, "One-dimensional dislocations. ii. misfitting monolayers and oriented overgrowth," *Proceedings of the Royal Society of London. Series A. Mathematical and Physical Sciences*, vol. 198, no. 1053, pp. 216–225, 1949.

[38] G. Gioia and M. Ortiz, "Delamination of compressed thin films," *Advances in applied mechanics*, vol. 33, no. 8, pp. 119–192, 1997.

[39] J. Colin, C. Coupeau, J. Durinck, and J. Grilhé, "Buckling patterns of gold thin films on silicon substrates: Formation of superimposed blisters," *EPL (Europhysics Letters)*, vol. 86, no. 5, p. 54002, 2009.

[40] J. Colin, C. Coupeau, and J. Grilhé, "Plastic folding of buckling structures," *Physical review letters*, vol. 99, no. 4, p. 046101, 2007.

[41] F. Paumier, R. Gaboriaud, and C. Coupeau, "Buckling phenomena in Y_2O_3 thin films on GaAs substrates," *Applied physics letters*, vol. 82, no. 13, pp. 2056–2058, 2003.

[42] C. Coupeau, J. Naud, F. Cleymand, P. Goudeau, and J. Grilhé, "Atomic force microscopy of in situ deformed nickel thin films," *Thin Solid Films*, vol. 353, no. 1-2, pp. 194–200, 1999.

[43] J. Colin, F. Cleymand, C. Coupeau, and J. Grilhé, "Worm-like delamination patterns of thin stainless steel films on polycarbonate substrates," *Philosophical Magazine A*, vol. 80, no. 11, pp. 2559–2565, 2000.

[44] F. Cleymand, C. Coupeau, and J. Grilhé, "Atomic force microscopy investigation of buckling patterns of nickel thin films on polycarbonate substrates," *Philosophical Magazine Letters*, vol. 82, no. 9, pp. 477–482, 2002.

[45] N. Matuda, S. Baba, and A. Kinbara, "Internal stress, young's modulus and adhesion energy of carbon films on glass substrates," *Thin Solid Films*, vol. 81, no. 4, pp. 301–305, 1981.

[46] A. Föppl, "Vorlesungen über technische mechanik, bd. 5, leipzig," *G. Teubner*, 1907.

[47] T. Von Kármán, *Festigkeitsprobleme im maschinenbau*. Teubner, 1910.

[48] C. Coupeau, "From thin film and coating buckling structures to mechanical properties," *Materials Science and Engineering: A*, vol. 483, pp. 617–619, 2008.

[49] B. Boubeker, M. Talea, P. Goudeau, C. Coupeau, and J. Grilhe, "On the young's modulus of 304 l stainless steel thin films," *Materials characterization*, vol. 45, no. 1, pp. 33–37, 2000.

[50] G. Binnig, C. F. Quate, and C. Gerber, "Atomic force microscope," *Physical review letters*, vol. 56, no. 9, p. 930, 1986.

[51] F. J. Giessibl, S. Hembacher, M. Herz, C. Schiller, and J. Mannhart, "Stability considerations and implementation of cantilevers allowing dynamic force microscopy with optimal resolution: the qplus sensor," *Nanotechnology*, vol. 15, no. 2, p. S79, 2004.

[52] B. Pittenger, N. Erina, and C. Su, "Quantitative mechanical property mapping at the nanoscale with peakforce qnm," *Application Note Veeco Instruments Inc*, vol. 1, pp. 1–11, 2010.

[53] P. Trtik, J. Kaufmann, and U. Volz, "On the use of peak-force tapping atomic force microscopy for quantification of the local elastic modulus in hardened cement paste," *Cement and concrete research*, vol. 42, no. 1, pp. 215–221, 2012.

[54] K. Xu, W. Sun, Y. Shao, F. Wei, X. Zhang, W. Wang, and P. Li, "Recent development of peakforce tapping mode atomic force microscopy and its applications on nanoscience," *Nanotechnology Reviews*, vol. 7, no. 6, pp. 605–621, 2018.

[55] S. Gazze, I. Hallin, G. Quinn, E. Dudley, G. Matthews, P. Rees, G. Van Keulen, S. Doerr, and L. Francis, "Organic matter identifies the nano-mechanical properties of native soil aggregates," *Nanoscale*, vol. 10, no. 2, pp. 520–525, 2018.

[56] G. Binnig, H. Rohrer, C. Gerber, and E. Weibel, "Surface studies by scanning tunneling microscopy," *Physical review letters*, vol. 49, no. 1, p. 57, 1982.

[57] G. Binnig, H. Rohrer, C. Gerber, and E. Weibel, "7× 7 reconstruction on Si(111) resolved in real space," *Physical review letters*, vol. 50, no. 2, p. 120, 1983.

[58] G. Binnig and H. Rohrer, "Scanning tunneling microscopy—from birth to adolescence," *reviews of modern physics*, vol. 59, no. 3, p. 615, 1987.

[59] W. Chen, V. Madhavan, T. Jamneala, and M. Crommie, "Scanning tunneling microscopy observation of an electronic superlattice at the surface of clean gold," *Physical Review Letters*, vol. 80, no. 7, p. 1469, 1998.

[60] H. Virus and P. T. Monitor, "Introduction to bruker's scanasyst and peakforce tapping afm technology,"

[61] Y. Nahas, F. Berneau, J. Bonneville, C. Coupeau, M. Drouet, B. Lamongie, M. Marteau, J. Michel, P. Tanguy, and C. Tromas, "An experimental uhv afm-stm device for characterizing surface nanostructures under stress/strain at variable temperature," *Review of Scientific Instruments*, vol. 84, no. 10, p. 105117, 2013.

[62] M. Bott, T. Michely, and G. Comsa, "Design principles of a variable temperature scanning tunneling microscope," *Review of scientific instruments*, vol. 66, no. 8, pp. 4135–4139, 1995.

[63] U. Krishnan, M. Kaur, K. Singh, M. Kumar, and A. Kumar, "A synoptic review of MoS_2: Synthesis to applications," *Superlattices and Microstructures*, vol. 128, pp. 274–297, 2019.

[64] H. Li, J. Wu, Z. Yin, and H. Zhang, "Preparation and applications of mechanically exfoliated single-layer and multilayer MoS_2 and WSe_2 nanosheets," *Accounts of chemical research*, vol. 47, no. 4, pp. 1067–1075, 2014.

[65] K. S. Novoselov, A. K. Geim, S. V. Morozov, D.-e. Jiang, Y. Zhang, S. V. Dubonos, I. V. Grigorieva, and A. A. Firsov, "Electric field effect in atomically thin carbon films," *science*, vol. 306, no. 5696, pp. 666–669, 2004.

[66] P. Yang, L. Zhu, F. Zhou, and Y. Zhang, "Wafer-scale uniform synthesis of 2D transition metal dichalcogenides single crystals via chemical vapor deposition," *Accounts of Materials Research*, vol. 3, no. 2, pp. 161–174, 2021.

[67] Y.-H. Lee, X.-Q. Zhang, W. Zhang, M.-T. Chang, C.-T. Lin, K.-D. Chang, Y.-C. Yu, J. T.-W. Wang, C.-S. Chang, L.-J. Li, *et al.*, "Synthesis of large-area MoS_2 atomic layers with chemical vapor deposition," *Advanced materials*, vol. 24, no. 17, pp. 2320–2325, 2012.

[68] B. Qin, H. Ma, M. Hossain, M. Zhong, Q. Xia, B. Li, and X. Duan, "Substrates in the synthesis of two-dimensional materials via chemical vapor deposition," *Chemistry of Materials*, vol. 32, no. 24, pp. 10321–10347, 2020.

[69] Y. Yu, C. Li, Y. Liu, L. Su, Y. Zhang, and L. Cao, "Controlled scalable synthesis of uniform, high-quality monolayer and few-layer MoS_2 films," *Scientific reports*, vol. 3, no. 1, pp. 1–6, 2013.

[70] Y.-C. Lin, W. Zhang, J.-K. Huang, K.-K. Liu, Y.-H. Lee, C.-T. Liang, C.-W. Chu, and L.-J. Li, "Wafer-scale MoS_2 thin layers prepared by MoO_3 sulfurization," *Nanoscale*, vol. 4, no. 20, pp. 6637–6641, 2012.

[71] K.-K. Liu, W. Zhang, Y.-H. Lee, Y.-C. Lin, M.-T. Chang, C.-Y. Su, C.-S. Chang, H. Li, Y. Shi, H. Zhang, *et al.*, "Growth of large-area and highly crystalline MoS_2 thin layers on insulating substrates," *Nano letters*, vol. 12, no. 3, pp. 1538–1544, 2012.

[72] Y. Zhang, Q. Ji, G.-F. Han, J. Ju, J. Shi, D. Ma, J. Sun, Y. Zhang, M. Li, X.-Y. Lang, *et al.*, "Dendritic, transferable, strictly monolayer MoS_2 flakes synthesized on $SrTiO_3$ single crystals for efficient electrocatalytic applications," *ACS nano*, vol. 8, no. 8, pp. 8617–8624, 2014.

[73] Q. Ji, Y. Zhang, T. Gao, Y. Zhang, D. Ma, M. Liu, Y. Chen, X. Qiao, P.-H. Tan, M. Kan, *et al.*, "Epitaxial monolayer MoS_2 on mica with novel photoluminescence," *Nano letters*, vol. 13, no. 8, pp. 3870–3877, 2013.

[74] D. Ma, J. Shi, Q. Ji, K. Chen, J. Yin, Y. Lin, Y. Zhang, M. Liu, Q. Feng, X. Song, X. Guo, J. Zhang, Y. Zhang, and Z. Liu, "A universal etching-free transfer of MoS_2 films for applications in photodetectors," *Nano Research*, vol. 8, pp. 3662–3672, Nov. 2015.

[75] M. A. Meitl, Z.-T. Zhu, V. Kumar, K. J. Lee, X. Feng, Y. Y. Huang, I. Adesida, R. G. Nuzzo, and J. A. Rogers, "Transfer printing by kinetic control of adhesion to an elastomeric stamp," *Nature materials*, vol. 5, no. 1, pp. 33–38, 2006.

[76] Z. Lu, L. Sun, G. Xu, J. Zheng, Q. Zhang, J. Wang, and L. Jiao, "Universal transfer and stacking of chemical vapor deposition grown two-dimensional atomic layers with water-soluble polymer mediator," *ACS nano*, vol. 10, no. 5, pp. 5237–5242, 2016.

[77] Y. Qian, M. K. Sohn, H. J. Park, J. S. Hwang, K. Subramanian, and D. J. Kang, "Universal 2D material film transfer using a novel low molecular weight polyvinyl acetate," *Applied Surface Science*, vol. 534, p. 147650, Dec. 2020.

[78] Z. Zhang, J. Du, D. Zhang, H. Sun, L. Yin, L. Ma, J. Chen, D. Ma, H.-M. Cheng, and W. Ren, "Rosin-enabled ultraclean and damage-free transfer of graphene for large-area flexible organic light-emitting diodes," *Nature communications*, vol. 8, no. 1, pp. 1–9, 2017.

[79] H. Li, J. Wu, X. Huang, Z. Yin, J. Liu, and H. Zhang, "A Universal, Rapid Method for Clean Transfer of Nanostructures onto Various Substrates," *ACS Nano*, vol. 8, pp. 6563–6570, July 2014.

[80] A. Gurarslan, Y. Yu, L. Su, Y. Yu, F. Suarez, S. Yao, Y. Zhu, M. Ozturk, Y. Zhang, and L. Cao, "Surface-Energy-Assisted Perfect Transfer of Centimeter-Scale Monolayer and Few-Layer MoS_2 Films onto Arbitrary Substrates," *ACS Nano*, vol. 8, pp. 11522–11528, Nov. 2014.

[81] T. Filleter and R. Bennewitz, "Nanometre-scale plasticity of Cu (100)," *Nanotechnology*, vol. 18, no. 4, p. 044004, 2006.

[82] K. Kurahashi, T. Matsuda, Y. Ishida, and T. Ichikawa, "Effect of polishing protocols on the surface roughness of polyetheretherketone," *Journal of Oral Science*, vol. 62, no. 1, pp. 40–42, 2020.

[83] C. M. Bollen, W. Papaioanno, J. Van Eldere, E. Schepers, M. Quirynen, and D. Van Steenberghe, "The influence of abutment surface roughness on plaque accumulation and peri-implant mucositis," *Clinical oral implants research*, vol. 7, no. 3, pp. 201–211, 1996.

[84] W. Choi, M. A. Shehzad, S. Park, and Y. Seo, "Influence of removing pmma residues on surface of cvd graphene using a contact-mode atomic force microscope," *RSC advances*, vol. 7, no. 12, pp. 6943–6949, 2017.

[85] L. E. Davis, "Handbook of auger electron spectroscopy," *Physical Electronics Division*, 1978.

[86] D. Briggs, "Practical surface analysis," *Auger and X-Ray Photoelecton Spectroscory*, vol. 1, pp. 151–152, 1990.

[87] J. R. Lince, "Tribology of co-sputtered nanocomposite au/MoS_2 solid lubricant films over a wide contact stress range," *Tribology Letters*, vol. 17, no. 3, pp. 419–428, 2004.

[88] Y.-C. Lin, C.-C. Lu, C.-H. Yeh, C. Jin, K. Suenaga, and P.-W. Chiu, "Graphene annealing: how clean can it be?," *Nano letters*, vol. 12, no. 1, pp. 414–419, 2012.

[89] U. Ali, K. J. B. A. Karim, and N. A. Buang, "A review of the properties and applications of poly (methyl methacrylate) (PMMA)," *Polymer Reviews*, vol. 55, no. 4, pp. 678–705, 2015.

[90] A. Kozbial, F. Zhou, Z. Li, H. Liu, and L. Li, "Are graphitic surfaces hydrophobic?," *Accounts of chemical research*, vol. 49, no. 12, pp. 2765–2773, 2016.

[91] A. Pirkle, J. Chan, A. Venugopal, D. Hinojos, C. Magnuson, S. McDonnell, L. Colombo, E. Vogel, R. Ruoff, and R. Wallace, "The effect of chemical residues on the physical and electrical properties of chemical vapor deposited graphene transferred to SiO_2," *Applied Physics Letters*, vol. 99, no. 12, p. 122108, 2011.

[92] H. Walen, D.-J. Liu, J. Oh, H. Lim, J. W. Evans, Y. Kim, and P. A. Thiel, "Self-organization of s adatoms on Au (111): $\sqrt{3}$R30 rows at low coverage," *The Journal of chemical physics*, vol. 143, no. 1, p. 014704, 2015.

[93] S. S. Grønborg, S. Ulstrup, M. Bianchi, M. Dendzik, C. E. Sanders, J. V. Lauritsen, P. Hofmann, and J. A. Miwa, "Synthesis of epitaxial single-layer MoS_2 on Au(111)," *Langmuir*, vol. 31, no. 35, pp. 9700–9706, 2015.

[94] N. Krane, C. Lotze, and K. J. Franke, "Moiré structure of MoS_2 on Au(111): Local structural and electronic properties," *Surface Science*, vol. 678, pp. 136–142, Dec. 2018.

[95] S. G. Sørensen, H. G. Füchtbauer, A. K. Tuxen, A. S. Walton, and J. V. Lauritsen, "Structure and electronic properties of in situ synthesized single-layer MoS_2 on a gold surface," *ACS nano*, vol. 8, no. 7, pp. 6788–6796, 2014.

[96] A. Bruix, J. A. Miwa, N. Hauptmann, D. Wegner, S. Ulstrup, S. S. Grønborg, C. E. Sanders, M. Dendzik, A. A. Khajetoorians, B. Hammer, and P. Hofmann, "Single-Layer MoS_2 on Au(111): Band gap renormalization and substrate interaction," *PHYSICAL REVIEW B*, p. 10, 2016.

[97] J. A. Stroscio, R. Feenstra, and A. Fein, "Electronic structure of the Si(111) 2× 1 surface by scanning-tunneling microscopy," *Physical review letters*, vol. 57, no. 20, p. 2579, 1986.

[98] C. Murray, W. Jolie, J. A. Fischer, J. Hall, C. van Efferen, N. Ehlen, A. Grüneis, C. Busse, and T. Michely, "Comprehensive tunneling spectroscopy of quasifreestanding MoS_2 on graphene on Ir(111)," *Physical Review B*, vol. 99, no. 11, p. 115434, 2019.

[99] D. J. Trainer, A. V. Putilov, C. Di Giorgio, T. Saari, B. Wang, M. Wolak, R. U. Chandrasena, C. Lane, T.-R. Chang, H.-T. Jeng, *et al.*, "Inter-layer coupling induced valence band edge shift in mono-to few-layer MoS_2," *Scientific reports*, vol. 7, no. 1, pp. 1–11, 2017.

[100] J. Ryou, Y.-S. Kim, S. Kc, and K. Cho, "Monolayer MoS_2 bandgap modulation by dielectric environments and tunable bandgap transistors," *Scientific reports*, vol. 6, no. 1, pp. 1–8, 2016.

[101] D. Yang, S. J. Sandoval, W. Divigalpitiya, J. Irwin, and R. Frindt, "Structure of single-molecular-layer MoS_2," *Physical Review B*, vol. 43, no. 14, p. 12053, 1991.

[102] C. Lee, H. Yan, L. E. Brus, T. F. Heinz, J. Hone, and S. Ryu, "Anomalous lattice vibrations of single-and few-layer MoS_2," *ACS nano*, vol. 4, no. 5, pp. 2695–2700, 2010.

[103] S. Choi, Z. Shaolin, and W. Yang, "Layer-number-dependent work function of MoS_2 nanoflakes," *Journal of the Korean Physical Society*, vol. 64, no. 10, pp. 1550–1555, 2014.

[104] F. Cleymand, C. Coupeau, J. Colin, and J. Grilhé, "Interactive study of straight-sided buckling patterns in thin films under compressive stress," *The European Physical Journal-Applied Physics*, vol. 10, no. 1, pp. 3–7, 2000.

[105] C. Coupeau, R. Boijoux, Y. Ni, and G. Parry, "Interacting straight-sided buckles: an enhanced attraction by substrate elasticity," *Journal of the Mechanics and Physics of Solids*, vol. 124, pp. 526–535, 2019.

[106] B. Burgarella, A. Maurel-Pantel, N. Lahellec, J.-L. Bouvard, and N. Billon, "Modeling the effective viscoelastic properties of peek matrix reinforced by arbitrary oriented short glass fibers," *Mechanics of Time-Dependent Materials*, pp. 1–29, 2020.

[107] F. Cleymand, C. Coupeau, and J. Grilhé, "Experimental investigation of the instability of buckling patterns: From straight-sided to wormlike structures," *Scripta materialia*, vol. 44, no. 11, pp. 2623–2627, 2001.

[108] B. Audoly, B. Roman, and A. Pocheau, "Secondary buckling patterns of a thin plate under in-plane compression," *The European Physical Journal B-Condensed Matter and Complex Systems*, vol. 27, no. 1, pp. 7–10, 2002.

[109] G. Parry, J. Colin, C. Coupeau, F. Foucher, A. Cimetière, and J. Grilhé, "Effect of substrate compliance on the global unilateral post-buckling of coatings: Afm observations and finite element calculations," *Acta materialia*, vol. 53, no. 2, pp. 441–447, 2005.

[110] S.-J. Yu, Y.-C. Shi, M.-G. Chen, P.-Z. Si, Y. Zhou, X.-F. Zhang, J. Chen, H. Zhou, and Z.-W. Jiao, "Coalescence behaviors of telephone cord buckles in $SiAlN_x$ films," *Surface and Coatings Technology*, vol. 232, pp. 884–890, 2013.

[111] S. Timoshenko and J. Goodier, *Theory of Elasticity*. Engineering societies monographs, McGraw-Hill, 1951.

[112] H. Langhaar, "Energy methods in applied mechanics. john wiley," *New York*, 1962.

[113] J. W. Hutchinson and Z. Suo, "Mixed mode cracking in layered materials," *Advances in applied mechanics*, vol. 29, pp. 63–191, 1991.

[114] L. B. Freund and S. Suresh, *Thin film materials: stress, defect formation and surface evolution*. Cambridge university press, 2004.

[115] L. Euler, *Institutiones calculi differentialis*. 1755.

[116] A. Ruffini, *Influence de la plasticité sur le délaminage et le flambage de films minces déposés sur substrats*. PhD thesis, Université de Poitiers, 2013.

[117] C. J. Brennan, J. Nguyen, E. T. Yu, and N. Lu, "Interface adhesion between 2d materials and elastomers measured by buckle delaminations," *Advanced Materials Interfaces*, vol. 2, no. 16, p. 1500176, 2015.

[118] J.-Y. Faou, G. Parry, S. Grachev, and E. Barthel, "Telephone cord buckles—a relation between wavelength and adhesion," *Journal of the Mechanics and Physics of Solids*, vol. 75, pp. 93–103, 2015.

[119] S.-W. Hahm, H.-S. Hwang, D. Kim, and D.-Y. Khang, "Buckling-based measurements of mechanical moduli of thin films," *Electronic Materials Letters*, vol. 5, no. 4, pp. 157–168, 2009.

[120] R. Boijoux, G. Parry, and C. Coupeau, "Buckle depression as a signature of young's modulus mismatch between a film and its substrate," *Thin Solid Films*, vol. 645, pp. 379–382, 2018.

[121] R. Boijoux, G. Parry, J.-Y. Faou, and C. Coupeau, "How soft substrates affect the buckling delamination of thin films through crack front sink-in," *Applied Physics Letters*, vol. 110, no. 14, p. 141602, 2017.

[122] Y. Zhang and Y. Liu, "The mexican hat effect on the delamination buckling of a compressed thin film," *Acta Mechanica Sinica*, vol. 30, no. 6, pp. 927–932, 2014.

[123] G. Casillas, U. Santiago, H. Barron, D. Alducin, A. Ponce, and M. Jose-Yacaman, "Elasticity of MoS_2 sheets by mechanical deformation observed by in situ electron microscopy," *The Journal of Physical Chemistry C*, vol. 119, no. 1, pp. 710–715, 2015.

[124] S. Bertolazzi, J. Brivio, and A. Kis, "Acs nano 5 (2011) 9703," *Crossref, ISI*.

[125] D. Davidovikj, F. Alijani, S. J. Cartamil-Bueno, H. S. van der Zant, M. Amabili, and P. G. Steeneken, "Nonlinear dynamic characterization of two-dimensional materials," *Nature communications*, vol. 8, no. 1, pp. 1–7, 2017.

[126] A. Castellanos-Gomez, M. Poot, G. A. Steele, H. S. Van der Zant, N. Agraït, and G. Rubio-Bollinger, "Mechanical properties of freely suspended semiconducting graphene-like layers based on MoS_2," *Nanoscale research letters*, vol. 7, no. 1, pp. 1–4, 2012.

[127] T. Lorenz, J.-O. Joswig, and G. Seifert, "Stretching and breaking of monolayer MoS_2—an atomistic simulation," *2D Materials*, vol. 1, no. 1, p. 011007, 2014.

[128] J. Feldman, "Elastic constants of 2h-MoS_2 and 2h-$NbSe_2$ extracted from measured dispersion curves and linear compressibilities," *Journal of Physics and Chemistry of Solids*, vol. 37, no. 12, pp. 1141–1144, 1976.

[129] J. Zhao, J.-W. Jiang, and T. Rabczuk, "Temperature-dependent mechanical properties of single-layer molybdenum disulphide: Molecular dynamics nanoindentation simulations," *Applied Physics Letters*, vol. 103, no. 23, p. 231913, 2013.

[130] K. Q. Dang and D. E. Spearot, "Effect of point and grain boundary defects on the mechanical behavior of monolayer MoS_2 under tension via atomistic simulations," *Journal of Applied Physics*, vol. 116, no. 1, p. 013508, 2014.

[131] J. Li, N. V. Medhekar, and V. B. Shenoy, "Bonding charge density and ultimate strength of monolayer transition metal dichalcogenides," *The Journal of Physical Chemistry C*, vol. 117, no. 30, pp. 15842–15848, 2013.

[132] C. Ataca, M. Topsakal, E. Akturk, and S. Ciraci, "A comparative study of lattice dynamics of three-and two-dimensional MoS_2," *The Journal of Physical Chemistry C*, vol. 115, no. 33, pp. 16354–16361, 2011.

[133] B. Mortazavi, A. Ostadhossein, T. Rabczuk, and A. C. Van Duin, "Mechanical response of all-MoS_2 single-layer heterostructures: a reaxff investigation," *Physical Chemistry Chemical Physics*, vol. 18, no. 34, pp. 23695–23701, 2016.

[134] K. S. Kim, Y. Zhao, H. Jang, S. Y. Lee, J. M. Kim, K. S. Kim, J.-H. Ahn, P. Kim, J.-Y. Choi, and B. H. Hong, "Large-scale pattern growth of graphene films for stretchable transparent electrodes," *nature*, vol. 457, no. 7230, pp. 706–710, 2009.

[135] L. B. Freund, "Some elementary connections between curvature and mismatch strain in compositionally graded thin films," *Journal of the Mechanics and Physics of Solids*, vol. 44, no. 5, pp. 723–736, 1996.

[136] T. Mohiuddin, A. Lombardo, R. Nair, A. Bonetti, G. Savini, R. Jalil, N. Bonini, D. Basko, C. Galiotis, N. Marzari, *et al.*, "Uniaxial strain in graphene by raman spectroscopy: G peak splitting, grüneisen parameters, and sample orientation," *Physical Review B*, vol. 79, no. 20, p. 205433, 2009.

[137] Z. Liu, M. Amani, S. Najmaei, Q. Xu, X. Zou, W. Zhou, T. Yu, C. Qiu, A. G. Birdwell, F. J. Crowne, *et al.*, "Strain and structure heterogeneity in MoS_2 atomic layers grown by chemical vapour deposition," *Nature communications*, vol. 5, no. 1, pp. 1–9, 2014.

[138] M. Dong, R. J. Young, D. J. Dunstan, and D. G. Papageorgiou, "Interfacial stress transfer in monolayer and few-layer MoS_2 nanosheets in model nanocomposites," *arXiv preprint arXiv:2210.09747*, 2022.

[139] G. Wells, T. Hopf, K. Vassilevski, E. Escobedo-Cousin, N. Wright, A. Horsfall, J. Goss, A. O'Neill, and M. Hunt, "Determination of the adhesion energy of graphene on SiC(0001) via measurement of pleat defects," *Applied Physics Letters*, vol. 105, no. 19, p. 193109, 2014.

[140] T. Jiang, R. Huang, and Y. Zhu, "Interfacial sliding and buckling of monolayer graphene on a stretchable substrate," *Advanced Functional Materials*, vol. 24, no. 3, pp. 396–402, 2014.

Abstract

The purpose of this thesis is to investigate the mechanical response of ultra-thin MoS_2 films to compressive strain and determine if the buckling theory of thin plates can be extended to extremely thin 2D materials. MoS_2 thin films are transferred from their growth substrates to polyether-ether-ketone substrate through a homemade technique where no sacrificial coating is used. Samples are deformed by imposing uni-axial strain on the substrates. The concomitant response of the film in the form of straight-sided buckles has been observed and characterised by *in-situ* atomic force microscope. Propagation and interaction of the straight-sided buckles are compared and found to be in good agreement with the behaviour of straight-sided buckles of thin metallic plates under compression. The Young's modulus of the strained film has been determined by taking advantage of depressions observed at the edges of the buckles. The observed critical buckling strain, higher than the expected one, has been linked to the adhesion of the film to the substrate and has been used to determine the adhesion energy of the film. The evolution of the buckles is studied in the frame-work of modified Föppl–von Kármán equations where the influence of substrate elasticity is considered. A comparison of experimental results with the theoretical model reveals an increase in maximum deflection of the buckling structures. The difference has been linked to the displacement of the film with respect to the substrate, which is imposed by the sliding/shearing at the boundary of the flat film that pushes on the buckle. This displacement increases as the applied compression on the substrate increases and has also been linked to the change in morphology, as well as re-organisation of some buckles.

Keywords: Buckling, Delamination, Thin Films, Atomic Force Microscopy, Elasticity, MoS_2, TMDCs

Résumé

Le but de cette thèse est d'étudier la réponse mécanique des films ultra-minces de MoS_2 à la contrainte de compression et de déterminer si la théorie de flambage des films minces peut s'appliquer aux matériaux 2D. Les films minces de MoS_2 sont transférés de leurs substrats de croissance au substrat de polyéther-éther-cétone dans l'eau à l'aide d'un processus d'ultrasonication où aucun revêtement sacrificiel n'est utilisé. Les échantillons sont déformés en imposant une déformation uni-axiale sur les substrats. La réponse concomitante du film sous la forme de rides droites a été observée et caractérisée par microscope à force atomique *in-situ*. La propagation et l'interaction des rides observées sont en accord avec le composant des cloques observées préalablement sur des films minces métalliques sous compression. Le module d'Young du film contraint a été déterminé en tirant parti des dépressions observées sur les bords des rides. La contrainte de flambage critique, plus élevée que celle privée par l'élasticité, élevée observée a été liée à l'adhérence du film au substrat et a été utilisée pour déterminer l'énergie d'adhérence du couple film/substrat. L'évolution du cloquage est étudiée dans le cadre des équations de Föppl–von Kármán modifiés où l'influence de l'élasticité du substrat est prise en compte. Une comparaison des résultats expérimentaux avec le modèle Föppl–von Kármán révèle une augmentation de la déflexion maximale de la structure de cloquage des films contraints. La différence a été reliée au déplacement du film par rapport au substrat, qui est imposé par le glissement/cisaillement à la frontière entre la partie plane du film et la ride. Ce déplacement augmente à mesure que la compression appliquée sur le substrat augmente et a également été lié au changement de morphologie, ainsi qu'à la réorganisation de certaines cloques.

Mots-clés :Cloquage, Délaminage, Couches Minces, Microscopie à Force Atomique, Élasticité, MoS_2, TMDCs